DHI-WASY Software

FEFLOW®

Finite Element Subsurface Flow
& Transport Simulation System

White Papers
Vol. V

DHI-WASY GmbH

DHI-WASY GmbH,
Waltersdorfer Straße 105, D-12526 Berlin, Germany
Phone: +49-30-67 99 98-0, Fax: +49-30-67 99 98-99
E-Mail: mail@dhi-wasy.de

Contents

1 Finite element formulation for borehole heat exchangers in modeling geothermal heating systems by FEFLOW

H.-J. G. Diersch[a], D. Bauer[b], W. Heidemann[b], W. Rühaak[a] & P. Schätzl[a]

[a]*DHI-WASY GmbH, Berlin, Germany*
[b]*Institute of Thermodynamics and Thermal Engineering (ITW), University of Stuttgart, Germany*

1.1 Introduction

In shallow aquifers a modern geothermal heat extraction technology (*geoexchange*) concerns the use of Borehole Heat Exchanger (BHE) systems of different construction. The most common in practice are single U-shape pipe (consisting of an inlet pipe, an outlet pipe and grout), double U-shape pipe (consisting of two inlet pipes, two outlet pipes and grout) and coaxial pipe (consisting of an inlet pipe included with an outlet pipe and grout) installations. Such heat exchangers form a vertical borehole system, where a refrigerant circulates in closed pipes exchanging heat with the surrounding aquifer driven alone by thermal conductivity (*closed loop system*). However, the extreme geometrical aspect ratios (extreme slenderness), typically involved in those boreholes, require an advanced numerical strategy, where the BHE systems are modeled by 1D finite-element representations. We mainly follow the ideas proposed by Al-Khoury *et al.*[1,2], who firstly used 1D single and double U-pipe elements in the context of geothermal heating systems. Al-Khoury *et al.*'s numerical strategy is further extended and adapted to the FEFLOW simulator with respect to the following:

- Generalization of the formulations for single and double U-shape as well as coaxial pipe configurations.
- Improving pipe-to-grout approximation method by using multiple grout points in application to single and double U-shape pipe exchangers.
- Improving relationships for thermal resistances of BHE.
- Integrating the 1D BHE pipe elements into FEFLOW's finite-element matrix system similar to fracture elements.
- Direct and non-sequential (essentially non-iterative) coupling of the 1D pipe elements to the porous medium discretization.
- Extending FEFLOW's boundary conditions for BHE pipes similar to multi-well borehole conditions.

In addition, the local processes within BHE can also alternatively be modeled via an analytical technique under the major assumption that *local* steady-state conditions are considered, where a thermal equilibrium immediately occurs between inlet and outlet pipes for a

given solid temperature at the borehole wall. Such type of analytical solutions has been firstly introduced by Eskilson and Claesson[12]. Their local analytical model is taken as an alternative to the general Al-Khoury *et al.*'s numerical strategy, particularly for long-term predictions. We will extend Eskilson and Claesson's analytical solution to different types of BHE and embed it in a general iterative finite-element strategy for solving the overall problem. Al-Khoury *et al.*'s numerical and Eskilson and Claesson's analytical strategies will be compared and tested. While the Al-Khoury *et al.*'s numerical approach has proven appropriated over the full time range of processes, Eskilson and Claesson's analytical solution is not suited for short-term predictions (say, thermal responses in a time range smaller than some hours), however, for long-term predictions the analytical solution has been shown in a well and reasonable accuracy in comparison to the general Al-Khoury *et al.*'s numerical strategy. In FEFLOW both modeling approaches are available and can be chosen in accordance with the specific needs in modeling.

1.2 Types of BHE

1.2.1 Double U-shape pipe (2U)

The double U-shape pipe (2U) exchanger is a cylindrical borehole consisting of two inner pipes forming a U-shape and filled with a grout material as shown in Fig. 1.1. Basically, the grout can be considered as a homogeneous material and could be schematized by only one component so as proposed by Al-Khoury *et al.*[1,2]. However, to improve the approximation of the inner pipe-to-grout heat transfer we introduce a larger number of grout components, which correlates with the number of pipes of BHE. This has some advantages: (1) A better accuracy results in modeling the transient behavior of U-shape pipe exchangers. (2) It allows a much higher flexibility in configuration of U-shape pipe systems, particularly, the U-shape pipes can be arranged crosswise or side by side. (3) Furthermore, the flow through double U-shape pipe configurations can be parallel or serial.

In total, we schematize a 2U exchanger by eight components:

- two pipes-in (denoted as *i1* and *i2*)
- two pipes-out (denoted as *o1* and *o2*)
- grout material, which is subdivided into 4 zones (denoted as *g1*, *g2*, *g3*, *g4*)

The four pipe components *i1*, *i2*, *o1*, and *o2* transfer heat across their cross-sectional areas and exchange fluxes across their surface areas. The radial heat transfer from the pipes is directed to the grout zones *gi* (i = 1,...,4). The grout zones *gi* (i = 1,...,4) exchange heat directly to the surrounding soil (the porous matrix with the filled fluid in the void space) denoted as *s* and to other contacted grout zones too. It can be seen that, as physically occurring, the heat coupling only occurs via the grout zones *gi* (i = 1,...,4), which work as intermediate media that transfer heat from one pipe to another and *vice versa*. Only the grout zones exchange heat with the surrounding soil *s* because there is no direct thermal contact between the pipes *i1*, *i2*, *o1*, and *o2* with the soil *s*.

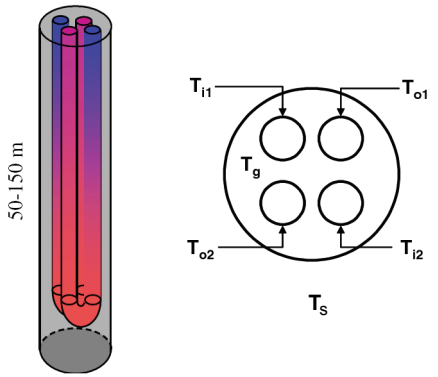

Figure 1.1 Schematization of a 2U-type BHE (from Al-Khoury and Bonnier[2]).

The 2U system involves several material and geometrical parameters, which are either given by the manufacturer of the heating systems or determined experimentally. These relations are used to express the overall thermal resistance between the 2U borehole and the soil. The usual practice is to lump the effects of the 2U components into effective heat transfer coefficients representing the reciprocal of the sum of the thermal resistances between the different components. The inner pipe-grout heat flux resistance relationships are shown in Fig. 1.2. Their analytical descriptions will be given in Chapter 1.5.

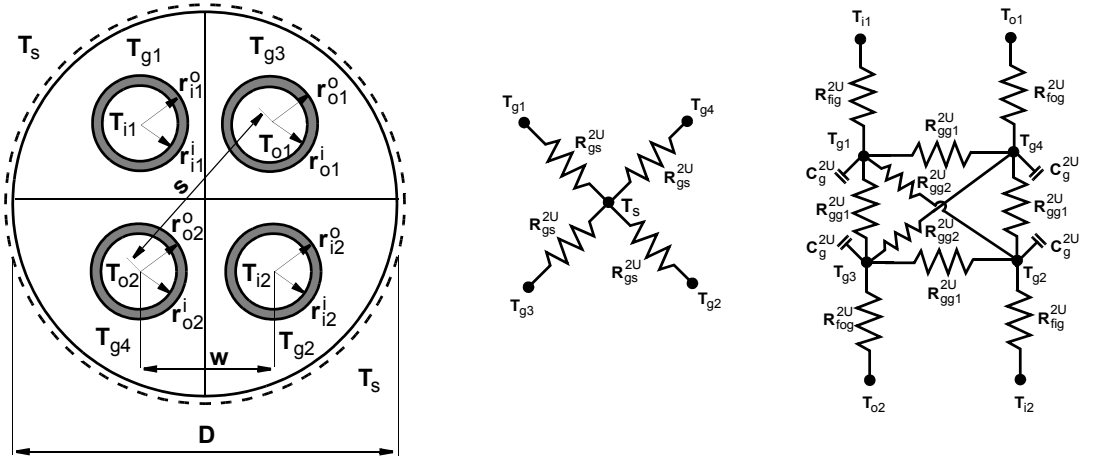

Figure 1.2 Inner pipe-grout heat flux resistance relationships of a 2U borehole consisting of four pipe components and four grout zones (exemplified for a crosswise configuration).

1.2.2 Single U-shape pipe (1U)

The single U-shape pipe (1U) exchanger can be easily degenerated from a 2U configuration when dropping the second U-tube. A 1U configuration only consists of four components:

- one pipe-in (denoted as *i1*)
- one pipe-out (denoted as *o1*)
- grout material, which is subdivided into 2 zones (denoted as *g1*, *g2*)

Similar to the 2U exchanger the U-tube of the 1U configuration transfers heat in radial direction to the grout zones *gi* (*i* = 1,...,2), while the grout material zones exchange heat directly to the surrounding soil *s* and to the adjacent grout zone. The corresponding inner pipe-grout heat flux resistance relationships are shown in Fig. 1.3.

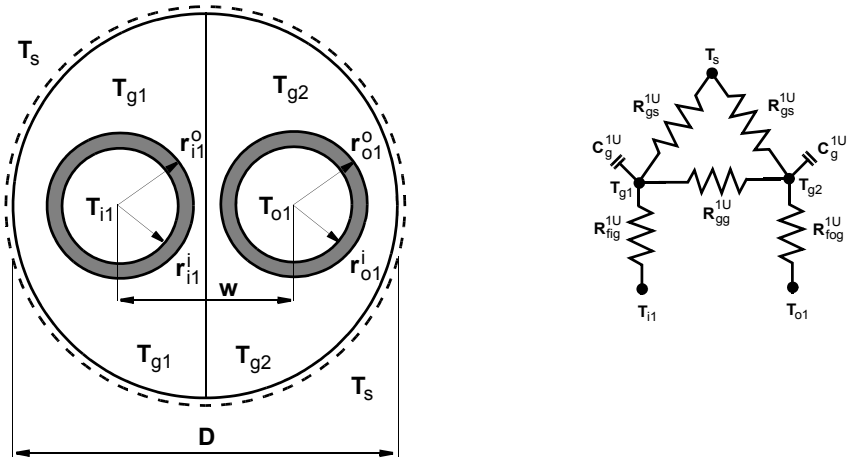

Figure 1.3 Inner pipe-grout heat flux resistance relationships of a 1U borehole consisting of two pipe components and two grout zones.

1.2.3 Coaxial pipe with annular (CXA) and centred (CXC) inlet

This type of BHE consists only of three components:

- one pipe-in (denoted as *i1*)
- one pipe-out (denoted as *o1*)
- grout material considered in one zone (denoted as *g1*)

Such coaxial BHE systems represent pipe-in-pipe installations, where two principal cases occur. In the case of the CXA exchanger the pipe-out is configured inside the pipe-in as shown in Fig. 1.4 forming an annular inlet and a centred outlet. Accordingly, the heat exchange to the grout material *g1*, which is in contact to the surrounding soil *s*, is only performed via the

pipe-in *i1*. On the other hand, the pipe-in *i1* exchanges heat with the pipe-out *o1* component. The coaxial pipes can also be installed with interchanged inlet and outlet. This represents the CXC exchanger, where the pipe-in is configured inside the pipe-out as shown in Fig. 1.5 forming a centred inlet and an annular outlet. Here, the heat exchange to the grout material *g1* is only performed via the pipe-out *o1*.

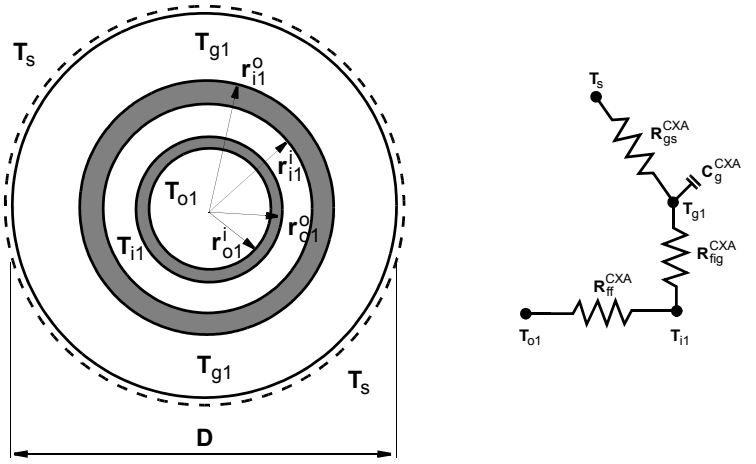

Figure 1.4 Inner pipe-grout heat flux resistance relationships of a CXA borehole with annular inlet.

1.3 Soil Equations

1.3.1 Basic equations

They describe the model equations for the *global* problem of the subsurface in form of balance laws for fluid mass, fluid momentum and thermal energy of soil *s* and fluid *f*. The conservation equation of fluid mass is given by

$$S_s \frac{\partial h}{\partial t} + \nabla \cdot \boldsymbol{q} = Q + Q_{\mathrm{EOB}} \tag{1-1}$$

where the used symbols are summarized in Appendix C. The flux $\boldsymbol{q}$ in the porous medium is expressed by the Darcy law as

$$\boldsymbol{q} = -\boldsymbol{K} f_{\mu} \left(\nabla h + \frac{\rho^f - \rho_0^f}{\rho_0^f} \boldsymbol{e} \right) \tag{1-2}$$

with the constitutive equations for fluid density and

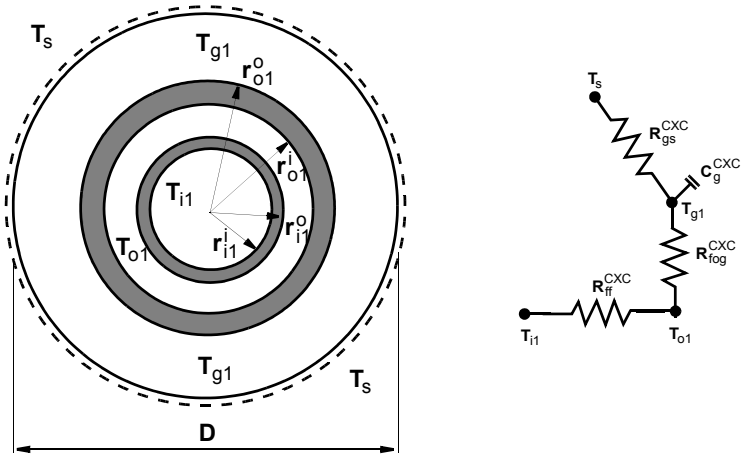

Figure 1.5 Inner pipe-grout heat flux resistance relationships of a CXC borehole with centred inlet.

viscosity

$$\left.\begin{aligned} \rho^f &= \rho_0^f[1-\beta(T_s - T_{s0})] \\ f_\mu &= \frac{\mu_0^f}{\mu^f} \qquad \mu^f = \mu^f(T_s) \end{aligned}\right\} \tag{1-3}$$

The conservation equation of thermal energy in the soil s can be expressed as

$$\begin{aligned} &\frac{\partial}{\partial t}[(\varepsilon\rho^f c^f + (1-\varepsilon)\rho^s c^s)T_s] + \nabla\cdot(\rho^f c^f \boldsymbol{q} T_s) \\ &-\nabla\cdot(\boldsymbol{\Lambda}\cdot\nabla T_s) = H_s \end{aligned} \tag{1-4}$$

with the tensor of thermal hydrodynamic dispersion

$$\boldsymbol{\Lambda} = [\varepsilon\lambda^f + (1-\varepsilon)\lambda^s]\boldsymbol{I} + \rho^f c^f\Big[\alpha_T\|\boldsymbol{q}\|\boldsymbol{I} + (\alpha_L - \alpha_T)\frac{\boldsymbol{q}\otimes\boldsymbol{q}}{\|\boldsymbol{q}\|}\Big] \tag{1-5}$$

and the term of extended Oberbeck-Boussinesq approximation

$$Q_{\mathrm{EOB}} = \beta\Big(\boldsymbol{q}\cdot\nabla T_s + \varepsilon\frac{\partial T_s}{\partial t}\Big) \tag{1-6}$$

1.3.2 Thermal boundary conditions

The boundary of the domain Ω is denoted by Γ, which can be subdivided in a number of disjoint portions Γ_1, Γ_2 and Γ_3. The boundary conditions (BC) on these boundary portions associated with the thermal

field of the soil *s* are given as follows:

1.3.2.1 Dirichlet-type BC

$$T_s(\boldsymbol{x}, t) = T_s^R(t) \qquad \text{on} \qquad \Gamma_1 \times t[0,\infty) \tag{1-7}$$

1.3.2.2 Neumann-type BC

$$\boldsymbol{q}_{nT_s}(\boldsymbol{x}, t) = \boldsymbol{q}_{nT_s}^R(t) = -(\boldsymbol{\Lambda} \cdot \nabla T_s) \cdot \boldsymbol{n} \tag{1-8}$$
$$\text{on} \qquad \Gamma_2 \times t[0,\infty)$$

1.3.2.3 Cauchy-type BC

$$\boldsymbol{q}_{nT_s}(\boldsymbol{x}, t) = -\sum_{i=1}^{G} \Phi_{sg}(T_{gi} - T_s) \tag{1-9}$$
$$\text{on} \qquad \Gamma_3 \times t[0,\infty)$$

which represents an interaction surface with the borehole controlled by the heat transfer coefficient $\Phi_{sg} = \Phi_{gs}$ between the soil and grout material zones of the borehole. In (1-9) *G* denotes the number of grout zones, which is 4 for 2U, 2 for 1U, and 1 for CXA and CXC.

1.4 BHE Equations

The processes within the borehole are considered as a *local* problem, which is linked to the global (soil-related) problem via thermal transfer relationships. They are formulated by energy conservation equations for the BHE components consisting of pipe(s)-in, pipe(s)-out and grout zone(s).

1.4.1 2U exchanger

The BHE represents a closed pipe system, where a refrigerant fluid is circulating with a given velocity $\boldsymbol{u}$. The heat transport equations for the eight borehole components of a 2U configuration can be written as follows

$$\left.\begin{aligned} &\frac{\partial}{\partial t}(\rho^r c^r T_{i1}) + \nabla \cdot (\rho^r c^r \boldsymbol{u} T_{i1}) - \nabla \cdot (\boldsymbol{\Lambda}^r \cdot \nabla T_{i1}) = H_{i1} \qquad \text{in} \qquad \Omega_{i1} \\ &\text{with} \qquad \boldsymbol{q}_{nT_{i1}} = -\Phi_{fig}^{2U}(T_{g1} - T_{i1}) \qquad \text{on} \qquad \Gamma_{i1} \end{aligned}\right\} \tag{1-10a}$$

$$\left.\begin{aligned} &\frac{\partial}{\partial t}(\rho^r c^r T_{i2}) + \nabla \cdot (\rho^r c^r \boldsymbol{u} T_{i2}) - \nabla \cdot (\boldsymbol{\Lambda}^r \cdot \nabla T_{i2}) = H_{i2} \qquad \text{in} \qquad \Omega_{i2} \\ &\text{with} \qquad \boldsymbol{q}_{nT_{i2}} = -\Phi_{fig}^{2U}(T_{g2} - T_{i2}) \qquad \text{on} \qquad \Gamma_{i2} \end{aligned}\right\} \tag{1-10b}$$

$$\left.\begin{aligned} &\frac{\partial}{\partial t}(\rho^r c^r T_{o1}) + \nabla\cdot(\rho^r c^r \boldsymbol{u} T_{o1}) - \nabla\cdot(\boldsymbol{\Lambda}^r\cdot\nabla T_{o1}) = H_{o1} \quad \text{in} \quad \Omega_{o1} \\ &\text{with} \quad \boldsymbol{q}_{nT_{o1}} = -\Phi^{2U}_{fog}(T_{g3} - T_{o1}) \quad \text{on} \quad \Gamma_{o1} \end{aligned}\right\} \tag{1-10c}$$

$$\left.\begin{aligned} &\frac{\partial}{\partial t}(\rho^r c^r T_{o2}) + \nabla\cdot(\rho^r c^r \boldsymbol{u} T_{o2}) - \nabla\cdot(\boldsymbol{\Lambda}^r\cdot\nabla T_{o2}) = H_{o2} \quad \text{in} \quad \Omega_{o2} \\ &\text{with} \quad \boldsymbol{q}_{nT_{o2}} = -\Phi^{2U}_{fog}(T_{g4} - T_{o2}) \quad \text{on} \quad \Gamma_{o2} \end{aligned}\right\} \tag{1-10d}$$

$$\left.\begin{aligned} &\frac{\partial}{\partial t}(\varepsilon_g\rho^g c^g T_{g1}) - \nabla\cdot(\varepsilon_g\lambda^g\nabla T_{g1}) = H_{g1} \quad \text{in} \quad \Omega_{g1} \\ &\text{with} \quad \boldsymbol{q}_{nT_{g1}} = -\Phi^{2U}_{gs}(T_s - T_{g1}) - \Phi^{2U}_{fig}(T_{i1} - T_{g1}) - \Phi^{2U}_{gg2}(T_{g2} - T_{g1}) \\ &\qquad\qquad -\Phi^{2U}_{gg1}(T_{g3} - T_{g1}) - \Phi^{2U}_{gg1}(T_{g4} - T_{g1}) \quad \text{on} \quad \Gamma_{g1} \end{aligned}\right\} \tag{1-10e}$$

$$\left.\begin{aligned} &\frac{\partial}{\partial t}(\varepsilon_g\rho^g c^g T_{g2}) - \nabla\cdot(\varepsilon_g\lambda^g\nabla T_{g2}) = H_{g2} \quad \text{in} \quad \Omega_{g2} \\ &\text{with} \quad \boldsymbol{q}_{nT_{g2}} = -\Phi^{2U}_{gs}(T_s - T_{g2}) - \Phi^{2U}_{fig}(T_{i2} - T_{g2}) - \Phi^{2U}_{gg2}(T_{g1} - T_{g2}) \\ &\qquad\qquad -\Phi^{2U}_{gg1}(T_{g3} - T_{g2}) - \Phi^{2U}_{gg1}(T_{g4} - T_{g2}) \quad \text{on} \quad \Gamma_{g2} \end{aligned}\right\} \tag{1-10f}$$

$$\left.\begin{aligned} &\frac{\partial}{\partial t}(\varepsilon_g\rho^g c^g T_{g3}) - \nabla\cdot(\varepsilon_g\lambda^g\nabla T_{g3}) = H_{g3} \quad \text{in} \quad \Omega_{g3} \\ &\text{with} \quad \boldsymbol{q}_{nT_{g3}} = -\Phi^{2U}_{gs}(T_s - T_{g3}) - \Phi^{2U}_{fog}(T_{o1} - T_{g3}) - \Phi^{2U}_{gg2}(T_{g4} - T_{g3}) \\ &\qquad\qquad -\Phi^{2U}_{gg1}(T_{g1} - T_{g3}) - \Phi^{2U}_{gg1}(T_{g2} - T_{g3}) \quad \text{on} \quad \Gamma_{g3} \end{aligned}\right\} \tag{1-10g}$$

$$\left.\begin{aligned} &\frac{\partial}{\partial t}(\varepsilon_g\rho^g c^g T_{g4}) - \nabla\cdot(\varepsilon_g\lambda^g\nabla T_{g4}) = H_{g4} \quad \text{in} \quad \Omega_{g4} \\ &\text{with} \quad \boldsymbol{q}_{nT_{g4}} = -\Phi^{2U}_{gs}(T_s - T_{g4}) - \Phi^{2U}_{fog}(T_{o2} - T_{g4}) - \Phi^{2U}_{gg2}(T_{g3} - T_{g4}) \\ &\qquad\qquad -\Phi^{2U}_{gg1}(T_{g1} - T_{g4}) - \Phi^{2U}_{gg1}(T_{g2} - T_{g4}) \quad \text{on} \quad \Gamma_{g4} \end{aligned}\right\} \tag{1-10h}$$

where

$$\boldsymbol{\Lambda}^r = (\lambda^r + \rho^r c^r \alpha_L \|\boldsymbol{u}\|)\boldsymbol{I} \qquad (1\text{-}11)$$

1.4.2 1U exchanger

For the 1U exchanger only four borehole components exist consisting of one pipe-in, one pipe-out and two grout zones. In this case the equations (1-10b), (1-10d), (1-10f) and (1-10g) are irrelevant. It results

$$\left.\begin{aligned} \frac{\partial}{\partial t}(\rho^r c^r T_{i1}) + \nabla\cdot(\rho^r c^r \boldsymbol{u} T_{i1}) - \nabla\cdot(\boldsymbol{\Lambda}^r\cdot\nabla T_{i1}) &= H_{i1} \quad \text{in} \quad \Omega_{i1} \\ \text{with} \quad \boldsymbol{q}_{nT_{i1}} &= -\Phi^{1U}_{fig}(T_{g1} - T_{i1}) \quad \text{on} \quad \Gamma_{i1} \end{aligned}\right\} \qquad (1\text{-}12a)$$

$$\left.\begin{aligned} \frac{\partial}{\partial t}(\rho^r c^r T_{o1}) + \nabla\cdot(\rho^r c^r \boldsymbol{u} T_{o1}) - \nabla\cdot(\boldsymbol{\Lambda}^r\cdot\nabla T_{o1}) &= H_{o1} \quad \text{in} \quad \Omega_{o1} \\ \text{with} \quad \boldsymbol{q}_{nT_{o1}} &= -\Phi^{1U}_{fog}(T_{g2} - T_{o1}) \quad \text{on} \quad \Gamma_{o1} \end{aligned}\right\} \qquad (1\text{-}12b)$$

$$\left.\begin{aligned} \frac{\partial}{\partial t}(\varepsilon_g \rho^g c^g T_{g1}) - \nabla\cdot(\varepsilon_g \lambda^g \nabla T_{g1}) &= H_{g1} \quad \text{in} \quad \Omega_{g1} \\ \text{with} \quad \boldsymbol{q}_{nT_{g1}} = -\Phi^{1U}_{gs}(T_s - T_{g1}) - \Phi^{1U}_{fig}(T_{i1} - T_{g1}) - \Phi^{1U}_{gg}(T_{g2} - T_{g1}) &\quad \text{on} \quad \Gamma_{g1} \end{aligned}\right\} \qquad (1\text{-}12c)$$

$$\left.\begin{aligned} \frac{\partial}{\partial t}(\varepsilon_g \rho^g c^g T_{g2}) - \nabla\cdot(\varepsilon_g \lambda^g \nabla T_{g2}) &= H_{g2} \quad \text{in} \quad \Omega_{g2} \\ \text{with} \quad \boldsymbol{q}_{nT_{g2}} = -\Phi^{1U}_{gs}(T_s - T_{g2}) - \Phi^{1U}_{fog}(T_{o1} - T_{g2}) - \Phi^{1U}_{gg}(T_{g1} - T_{g2}) &\quad \text{on} \quad \Gamma_{g2} \end{aligned}\right\} \qquad (1\text{-}12d)$$

1.4.3 CXA exchanger

A CXA exchanger only encompasses three borehole components consisting of one pipe-in, one pipe-out and one grout zone. The heat transport equations read

$$\left.\begin{aligned} \frac{\partial}{\partial t}(\rho^r c^r T_{i1}) + \nabla\cdot(\rho^r c^r \boldsymbol{u} T_{i1}) - \nabla\cdot(\boldsymbol{\Lambda}^r\cdot\nabla T_{i1}) &= H_{i1} \quad \text{in} \quad \Omega_{i1} \\ \text{with} \quad \boldsymbol{q}_{nT_{i1}} &= -\Phi_{fig}^{\text{CXA}}(T_{g1}-T_{i1}) - \Phi_{ff}^{\text{CXA}}(T_{o1}-T_{i1}) \quad \text{on} \quad \Gamma_{i1} \end{aligned}\right\} \tag{1-13a}$$

$$\left.\begin{aligned} \frac{\partial}{\partial t}(\rho^r c^r T_{o1}) + \nabla\cdot(\rho^r c^r \boldsymbol{u} T_{o1}) - \nabla\cdot(\boldsymbol{\Lambda}^r\cdot\nabla T_{o1}) &= H_{o1} \quad \text{in} \quad \Omega_{o1} \\ \text{with} \quad \boldsymbol{q}_{nT_{o1}} &= -\Phi_{ff}^{\text{CXA}}(T_{i1}-T_{o1}) \quad \text{on} \quad \Gamma_{o1} \end{aligned}\right\} \tag{1-13b}$$

$$\left.\begin{aligned} \frac{\partial}{\partial t}(\varepsilon_g \rho^g c^g T_{g1}) - \nabla\cdot(\varepsilon_g \lambda^g \nabla T_{g1}) &= H_{g1} \quad \text{in} \quad \Omega_{g1} \\ \text{with} \quad \boldsymbol{q}_{nT_{g1}} &= -\Phi_{gs}^{\text{CXA}}(T_s-T_{g1}) - \Phi_{fig}^{\text{CXA}}(T_{i1}-T_{g1}) \quad \text{on} \quad \Gamma_{g1} \end{aligned}\right\} \tag{1-13c}$$

1.4.4 CXC exchanger

Similarly to the CXA exchanger a CXC exchanger contains three borehole components consisting of one pipe-in, one pipe-out and one grout zone. The only difference is that the CXC exchanger with centred inlet pipe configuration the pipe-in only exchanges heat with the pipe-out. In this case the heat transport equations are given by

$$\left.\begin{aligned} \frac{\partial}{\partial t}(\rho^r c^r T_{i1}) + \nabla\cdot(\rho^r c^r \boldsymbol{u} T_{i1}) - \nabla\cdot(\boldsymbol{\Lambda}^r\cdot\nabla T_{i1}) &= H_{i1} \quad \text{in} \quad \Omega_{i1} \\ \text{with} \quad \boldsymbol{q}_{nT_{i1}} &= -\Phi_{ff}^{\mathrm{CXC}}(T_{o1}-T_{i1}) \quad \text{on} \quad \Gamma_{i1} \end{aligned}\right\} \tag{1-14a}$$

$$\left.\begin{aligned} \frac{\partial}{\partial t}(\rho^r c^r T_{o1}) + \nabla\cdot(\rho^r c^r \boldsymbol{u} T_{o1}) - \nabla\cdot(\boldsymbol{\Lambda}^r\cdot\nabla T_{o1}) &= H_{o1} \quad \text{in} \quad \Omega_{o1} \\ \text{with} \quad \boldsymbol{q}_{nT_{o1}} &= -\Phi_{fog}^{\mathrm{CXC}}(T_{g1}-T_{o1}) - \Phi_{ff}^{\mathrm{CXC}}(T_{i1}-T_{o1}) \quad \text{on} \quad \Gamma_{o1} \end{aligned}\right\} \tag{1-14b}$$

$$\left.\begin{aligned} \frac{\partial}{\partial t}(\varepsilon_g \rho^g c^g T_{g1}) - \nabla\cdot(\varepsilon_g \lambda^g \nabla T_{g1}) &= H_{g1} \quad \text{in} \quad \Omega_{g1} \\ \text{with} \quad \boldsymbol{q}_{nT_{g1}} &= -\Phi_{gs}^{\mathrm{CXC}}(T_s-T_{g1}) - \Phi_{fog}^{\mathrm{CXC}}(T_{o1}-T_{g1}) \quad \text{on} \quad \Gamma_{g1} \end{aligned}\right\} \tag{1-14c}$$

Note that $\Phi_{ff}^{\mathrm{CXA}} \neq \Phi_{ff}^{\mathrm{CXC}}$ due to the different pipe radii for pipe-in and pipe-out in a coaxial pipe installation.

1.5 Thermal Resistances

Thermal resistances are determined from the physical, material and geometric engineering parameters of the different BHE configurations as shown in Fig. 1.2 for the 2U exchanger, in Fig. 1.3 for the 1U exchanger, in Fig. 1.4 for the CXA exchanger and in Fig. 1.5 for the CXC exchanger. As indicated there the interaction between the different components of the pipe exists between the pipe-in and grout zone(s), the pipe-out and grout zone(s) as well as the pipe-in and pipe-out. The following thermal resistances can be derived.

1.5.1 2U exchanger

The thermal resistance between the pipes and grout zones is caused by the advection of the pipe flow and thermal conductivity of the pipe wall material specified separately for pipe-in and pipe-out

$$R_{fig}^{2\mathrm{U}} = R_{\mathrm{adv}_k}^{2\mathrm{U}} + R_{\mathrm{con}_k^a}^{2\mathrm{U}} + R_{\mathrm{con}^b}^{2\mathrm{U}} \qquad (k = i1 \cap i2) \tag{1-15a}$$

$$R_{fog}^{2\mathrm{U}} = R_{\mathrm{adv}_k}^{2\mathrm{U}} + R_{\mathrm{con}_k^a}^{2\mathrm{U}} + R_{\mathrm{con}^b}^{2\mathrm{U}} \qquad (k = o1 \cap o2) \tag{1-15b}$$

1.5.1.1 Thermal resistance due to the advective flow of refrigerant in the pipes

$$R_{\mathrm{adv}_k}^{2\mathrm{U}} = \frac{1}{\mathrm{Nu}_k \lambda^r \pi} \qquad (k = i1, o1, i2, o2) \tag{1-16}$$

In (1-16) the Nusselt numbers, Nu_k $(k = i1, o1, i2, o2)$, differ between laminar and turbulent flow[21], *viz.*,

$$\mathrm{Nu}_k = \begin{cases} 4.364 & \text{for laminar flow if } \mathrm{Re}_k < 2300 \\ \dfrac{(\xi_k/8)\mathrm{Re}_k \mathrm{Pr}}{1 + 12.7\sqrt{\xi_k/8}\,(\mathrm{Pr}^{2/3} - 1)}\left[1 + \left(\dfrac{d_k^i}{\bar{L}}\right)^{2/3}\right] & \text{for turbulent flow if } \mathrm{Re}_k \geq 10^4 \\ (1-\gamma_k)\,4.364 + \gamma_k\left\{\dfrac{(0.0308/8)10^4\,\mathrm{Pr}}{1 + 12.7\,\sqrt{0.0308/8}\,(\mathrm{Pr}^{2/3} - 1)}\left[1 + \left(\dfrac{d_k^i}{\bar{L}}\right)^{2/3}\right]\right\} & \text{for flow in transition range if } 2300 \leq \mathrm{Re}_k < 10^4 \end{cases} \quad (1\text{-}17)$$

in which Pr represents the Prandtl number and Re_k are the Reynolds number defined as

$$\mathrm{Pr} = \frac{\mu^r c^r}{\lambda^r} \qquad \mathrm{Re}_k = \frac{|\boldsymbol{u}_k|^{2\mathrm{U}} d_k^i}{(\mu^r/\rho^r)} \quad (k = i1, o1, i2, o2) \quad (1\text{-}18)$$

where d_k^i are the inner diameters of the pipes $d_k^i = 2r_k^i$ $(k = i1, o1, i2, o2)$. Furthermore, $\bar{L}$ corresponds to the length of the pipe and

$$\left.\begin{aligned} \xi_k &= (1.8\log_{10}\mathrm{Re}_k - 1.5)^{-2} \\ \gamma_k &= \frac{\mathrm{Re}_k - 2300}{10^4 - 2300} \qquad (0 \leq \gamma_k \leq 1) \end{aligned}\right\} \quad (1\text{-}19)$$

It is

$$|\boldsymbol{u}_k|^{2\mathrm{U}} = \begin{cases} \dfrac{Q_r}{2\pi(r_k^i)^2} & \text{for parallel discharge} \\ \dfrac{Q_r}{\pi(r_k^i)^2} & \text{for serial discharge} \end{cases} \quad (k = i1, o1, i2, o2) \quad (1\text{-}20)$$

where Q_r is the total refrigerant flow discharge of the 2U exchanger.

1.5.1.2 Thermal resistances due to the pipes wall material and grout transition

$$R^{2\mathrm{U}}_{\mathrm{con}_k^a} = \frac{\ln(r_k^o/r_k^i)}{2\pi\lambda_k^p} \qquad (k = i1, o1, i2, o2) \qquad (1\text{-}21)$$

where $\lambda_{i1}^p, \lambda_{o1}^p, \lambda_{i2}^p, \lambda_{o2}^p$ correspond to the thermal conductivities of the pipe wall material.

$$R_{\mathrm{con}^b}^{2\mathrm{U}} = x^{2\mathrm{U}} R_g^{2\mathrm{U}} \tag{1-22}$$

with

$$x^{2\mathrm{U}} = \frac{\ln\left(\frac{\sqrt{D^2 + 4d_o^2}}{2\sqrt{2}\ d_o}\right)}{\ln\left(\frac{D}{2d_o}\right)} \tag{1-23}$$

and

$$R_g^{2\mathrm{U}} = \frac{\operatorname{arcosh}\left(\frac{D^2 + d_o^2 - s^2}{2\ D\ d_o}\right)}{2\pi\lambda^g}\left(3.098 - 4.432\frac{s}{D} + 2.364\frac{s^2}{D^2}\right) \tag{1-24}$$

where D denotes the borehole diameter, $d_o = \frac{1}{4}\sum_k d_k^o$ is the averaged outer diameter of the pipes $d_k^o = 2r_k^o \quad (k = i1, o1, i2, o2)$ and $s = w\sqrt{2}$ corresponds to diagonal distance of pipes (see Fig. 1.2).

1.5.1.3 Thermal resistance due to inter-grout exchange

$$R_{gg1}^{2\mathrm{U}} = \frac{2R_{gs}^{2\mathrm{U}}(R_{ar1}^{2\mathrm{U}} - 2x^{2\mathrm{U}}R_g^{2\mathrm{U}})}{2R_{gs}^{2\mathrm{U}} - R_{ar1}^{2\mathrm{U}} + 2x^{2\mathrm{U}}R_g^{2\mathrm{U}}} \tag{1-25}$$

$$R_{gg2}^{2\mathrm{U}} = \frac{2R_{gs}^{2\mathrm{U}}(R_{ar2}^{2\mathrm{U}} - 2x^{2\mathrm{U}}R_g^{2\mathrm{U}})}{2R_{gs}^{2\mathrm{U}} - R_{ar2}^{2\mathrm{U}} + 2x^{2\mathrm{U}}R_g^{2\mathrm{U}}} \tag{1-26}$$

with

$$R_{ar1}^{2\mathrm{U}} = \frac{\operatorname{arcosh}\left(\frac{s^2 - d_o^2}{d_o^2}\right)}{2\pi\lambda^g} \tag{1-27}$$

$$R_{ar2}^{2\mathrm{U}} = \frac{\operatorname{arcosh}\left(\frac{2s^2 - d_o^2}{d_o^2}\right)}{2\pi\lambda^g} \tag{1-28}$$

1.5.1.4 Thermal resistance due to grout-soil exchange

$$R_{gs}^{2\mathrm{U}} = (1 - x^{2\mathrm{U}})R_g^{2\mathrm{U}} \tag{1-29}$$

1.5.2 1U exchanger

It is

$$R_{fig}^{1\mathrm{U}} = R_{\mathrm{adv}_k}^{1\mathrm{U}} + R_{\mathrm{con}_k^a}^{1\mathrm{U}} + R_{\mathrm{con}^b}^{1\mathrm{U}} \qquad (k = i1) \tag{1-30a}$$

$$R_{fog}^{1\mathrm{U}} = R_{\mathrm{adv}_k}^{1\mathrm{U}} + R_{\mathrm{con}_k^a}^{1\mathrm{U}} + R_{\mathrm{con}^b}^{1\mathrm{U}} \qquad (k = o1) \tag{1-30b}$$

1.5.2.1 Thermal resistance due to the advective flow of refrigerant in the pipes

with

$$R^{1U}_{adv_k} = \frac{1}{Nu_k \lambda^r \pi} \qquad (k = i1, o1) \qquad (1\text{-}31)$$

$$Nu_k = \begin{cases} 4.364 & \text{for laminar flow if } Re_k < 2300 \\ \dfrac{(\xi_k/8)Re_k Pr}{1 + 12.7\sqrt{\xi_k/8}\,(Pr^{2/3} - 1)}\left[1 + \left(\dfrac{d_k^i}{\bar{L}}\right)^{2/3}\right] & \text{for turbulent flow if } Re_k \geq 10^4 \\ (1-\gamma_k)\,4.364 + \gamma_k\left\{\dfrac{(0.0308/8)10^4\,Pr}{1 + 12.7\sqrt{0.0308/8}\,(Pr^{2/3} - 1)}\left[1 + \left(\dfrac{d_k^i}{\bar{L}}\right)^{2/3}\right]\right\} & \text{for flow in transition range if } 2300 \leq Re_k < 10^4 \end{cases} \qquad (1\text{-}32)$$

where

$$Pr = \frac{\mu^r c^r}{\lambda^r} \qquad Re_k = \frac{|\boldsymbol{u}_k|^{1U} d_k^i}{(\mu^r/\rho^r)} \qquad (k = i1, o1) \qquad (1\text{-}33)$$

and

$$\left.\begin{aligned} \xi_k &= (1.8\log_{10}Re_k - 1.5)^{-2} \\ \gamma_k &= \frac{Re_k - 2300}{10^4 - 2300} \qquad (0 \leq \gamma_k \leq 1) \end{aligned}\right\} \qquad (1\text{-}34)$$

$$|\boldsymbol{u}_k|^{1U} = \frac{Q_r}{2\pi(r_k^i)^2} \qquad (k = i1, o1) \qquad (1\text{-}35)$$

1.5.2.2 Thermal resistance due to the pipes wall material and grout transition

$$R^{1U}_{con^a_k} = \frac{\ln(r_k^o/r_k^i)}{2\pi\lambda_k^p} \qquad (k = i1, o1) \qquad (1\text{-}36)$$

$$R^{1U}_{con^b} = x^{1U} R_g^{1U} \qquad (1\text{-}37)$$

with

$$x^{1U} = \frac{\ln\left(\dfrac{\sqrt{D^2 + 2d_o^2}}{2d_o}\right)}{\ln\left(\dfrac{D}{\sqrt{2}\,d_o}\right)} \qquad (1\text{-}38)$$

and

$$R_g^{1U} = \frac{\operatorname{arcosh}\left(\frac{D^2 + d_o^2 - w^2}{2\,D\,d_o}\right)}{2\pi\lambda^g}\left(1.601 - 0.888\frac{w}{D}\right) \quad (1\text{-}39)$$

where w corresponds to distance of pipes (see Fig. 1.3).

1.5.2.3 Thermal resistance due to inter-grout exchange

$$R_{gg}^{1U} = \frac{2R_{gs}^{1U}(R_{ar}^{1U} - 2x^{1U}R_g^{1U})}{2R_{gs}^{1U} - R_{ar}^{1U} + 2x^{1U}R_g^{1U}} \quad (1\text{-}40)$$

with

$$R_{ar}^{1U} = \frac{\operatorname{arcosh}\left(\frac{2w^2 - d_o^2}{d_o^2}\right)}{2\pi\lambda^g} \quad (1\text{-}41)$$

1.5.2.4 Thermal resistance due to grout-soil exchange

$$R_{gs}^{1U} = (1 - x^{1U})R_g^{1U} \quad (1\text{-}42)$$

1.5.3 CXA exchanger

It is

$$R_{ff}^{CXA} = R_{\mathrm{adv}_{o1}}^{CXA} + R_{\mathrm{adv}_{i1}^a}^{CXA} + R_{\mathrm{con}_{o1}}^{CXA} \quad (1\text{-}43a)$$

$$R_{fig}^{CXA} = R_{\mathrm{adv}_{i1}^b}^{CXA} + R_{\mathrm{con}_{i1}}^{CXA} + R_{\mathrm{con}^b}^{CXA} \quad (1\text{-}43b)$$

1.5.3.1 Thermal resistance due to the advective flow of refrigerant in the pipes

$$R_{\mathrm{adv}_{o1}}^{CXA} = \frac{1}{\mathrm{Nu}_{o1}\lambda^r\pi} \quad (1\text{-}44a)$$

$$R_{\mathrm{adv}_{i1}^a}^{CXA} = \frac{1}{\mathrm{Nu}_{i1}\lambda^r\pi}\,\frac{d_h}{d_{o1}^o} \quad (1\text{-}44b)$$

$$R_{\mathrm{adv}_{i1}^b}^{CXA} = \frac{1}{\mathrm{Nu}_{i1}\lambda^r\pi}\,\frac{d_h}{d_{i1}^i} \quad (1\text{-}44c)$$

with

$$\mathrm{Nu}_{o1} = \begin{cases} 4.364 & \text{for laminar flow if } \mathrm{Re}_{o1} < 2300 \\ \dfrac{(\xi_{o1}/8)\mathrm{Re}_{o1}\mathrm{Pr}}{1+12.7\sqrt{\xi_{o1}/8}\,(\mathrm{Pr}^{2/3}-1)}\left[1+\left(\dfrac{d^i_{o1}}{\bar{L}}\right)^{2/3}\right] & \text{for turbulent flow if } \mathrm{Re}_{o1} \geq 10^4 \\ (1-\gamma_{o1})\,4.364 + \gamma_{o1}\left\{\dfrac{(0.0308/8)10^4\ \mathrm{Pr}}{1+12.7\sqrt{0.0308/8}\,(\mathrm{Pr}^{2/3}-1)}\left[1+\left(\dfrac{d^i_{o1}}{\bar{L}}\right)^{2/3}\right]\right\} & \text{for flow in transition range if } 2300 \leq \mathrm{Re}_{o1} < 10^4 \end{cases} \tag{1-45a}$$

$$\mathrm{Nu}_{i1} = \begin{cases} 3.66 + \left[4 - \dfrac{0.102}{\left(\dfrac{d^o_{o1}}{d^i_{i1}}\right)+0.02}\right]\left(\dfrac{d^o_{o1}}{d^i_{i1}}\right)^{0.04} & \text{for } \mathrm{Re}_{i1} < 2300 \\ \dfrac{(\xi_{i1}/8)\mathrm{Re}_{i1}\mathrm{Pr}}{1+12.7\sqrt{\xi_{i1}/8}\,(\mathrm{Pr}^{2/3}-1)}\left[1+\left(\dfrac{d_h}{\bar{L}}\right)^{2/3}\right]\dfrac{0.86\left(\dfrac{d^o_{o1}}{d^i_{i1}}\right)^{0.84}+\left[1-0.14\left(\dfrac{d^o_{o1}}{d^i_{i1}}\right)^{0.6}\right]}{1+\left(\dfrac{d^o_{o1}}{d^i_{i1}}\right)} & \text{for } \mathrm{Re}_{i1} \geq 10^4 \\ (1-\gamma_{i1})\left\{3.66 + \left[4 - \dfrac{0.102}{\left(\dfrac{d^o_{o1}}{d^i_{i1}}\right)+0.02}\right]\left(\dfrac{d^o_{o1}}{d^i_{i1}}\right)^{0.04}\right\} + & \\ \quad \gamma_{i1}\left\{\dfrac{(0.0308/8)10^4\ \mathrm{Pr}}{1+12.7\sqrt{0.0308/8}\,(\mathrm{Pr}^{2/3}-1)}\left[1+\left(\dfrac{d_h}{\bar{L}}\right)^{2/3}\right]\dfrac{0.86\left(\dfrac{d^o_{o1}}{d^i_{i1}}\right)^{0.84}+\left[1-0.14\left(\dfrac{d^o_{o1}}{d^i_{i1}}\right)^{0.6}\right]}{1+\left(\dfrac{d^o_{o1}}{d^i_{i1}}\right)}\right\} & \text{for } 2300 \leq \mathrm{Re}_{i1} < 10^4 \end{cases} \tag{1-45b}$$

where

$$\mathrm{Pr} = \frac{\mu^r c^r}{\lambda^r} \qquad \mathrm{Re}_{o1} = \frac{|\boldsymbol{u}_{o1}|^{\mathrm{CXA}} d^i_{o1}}{(\mu^r/\rho^r)} \qquad \mathrm{Re}_{i1} = \frac{|\boldsymbol{u}_{i1}|^{\mathrm{CXA}} d_h}{(\mu^r/\rho^r)} \tag{1-46}$$

and

$$d_h = d_{i1}^i - d_{o1}^o$$

$$\xi_k = (1.8 \log_{10}\mathrm{Re}_k - 1.5)^{-2} \qquad (k = i1, o1) \qquad (1\text{-}47)$$

$$\gamma_k = \frac{\mathrm{Re}_k - 2300}{10^4 - 2300} \qquad (0 \le \gamma_k \le 1)$$

$$\left.\begin{aligned} |\boldsymbol{u}_{o1}|^{\mathrm{CXA}} &= \frac{Q_r}{2\pi (r_{o1}^i)^2} \\ |\boldsymbol{u}_{i1}|^{\mathrm{CXA}} &= \frac{Q_r}{2\pi [(r_{i1}^i)^2 - (r_{o1}^o)^2]} \end{aligned}\right\} \qquad (1\text{-}48)$$

1.5.3.2 Thermal resistance due to the pipes wall material and grout transition

$$R_{\mathrm{con}_k}^{\mathrm{CXA}} = \frac{\ln(r_k^o / r_k^i)}{2\pi\lambda_k^p} \qquad (k = i1, o1) \qquad (1\text{-}49)$$

$$R_{\mathrm{con}^b}^{\mathrm{CXA}} = x^{\mathrm{CXA}} R_g^{\mathrm{CXA}} \qquad (1\text{-}50)$$

with

$$x^{\mathrm{CXA}} = \frac{\ln\left(\frac{\sqrt{D^2 + (d_{i1}^o)^2}}{\sqrt{2} d_{i1}^o}\right)}{\ln\left(\frac{D}{d_{i1}^o}\right)} \qquad (1\text{-}51)$$

and

$$R_g^{\mathrm{CXA}} = \frac{\ln(D / d_{i1}^o)}{2\pi\lambda^g} \qquad (1\text{-}52)$$

1.5.3.3 Thermal resistance due to grout-soil exchange

$$R_{gs}^{\mathrm{CXA}} = (1 - x^{\mathrm{CXA}}) R_g^{\mathrm{CXA}} \qquad (1\text{-}53)$$

1.5.4 CXC exchanger

It is

$$R_{ff}^{\mathrm{CXC}} = R_{\mathrm{adv}_{i1}}^{\mathrm{CXC}} + R_{\mathrm{adv}_{o1}^a}^{\mathrm{CXC}} + R_{\mathrm{con}_{i1}}^{\mathrm{CXC}} \qquad (1\text{-}54a)$$

$$R_{fog}^{\mathrm{CXC}} = R_{\mathrm{adv}_{o1}^b}^{\mathrm{CXC}} + R_{\mathrm{con}_{o1}}^{\mathrm{CXC}} + R_{\mathrm{con}^b}^{\mathrm{CXC}} \qquad (1\text{-}54b)$$

1.5.4.1 Thermal resistance due to the advective flow of refrigerant in the pipes

$$R_{\mathrm{adv}_{i1}}^{\mathrm{CXC}} = \frac{1}{\mathrm{Nu}_{i1}\lambda^r \pi} \qquad (1\text{-}55a)$$

$$R_{\mathrm{adv}_{o1}^a}^{\mathrm{CXC}} = \frac{1}{\mathrm{Nu}_{o1}\lambda^r \pi} \frac{d_h}{d_{i1}^o} \qquad (1\text{-}55b)$$

$$R_{\mathrm{adv}_{o1}^b}^{\mathrm{CXC}} = \frac{1}{\mathrm{Nu}_{o1}\lambda^r \pi} \frac{d_h}{d_{o1}^i} \qquad (1\text{-}55c)$$

with

$$\mathrm{Nu}_{i1} = \begin{cases} 4.364 & \text{for laminar flow if } \mathrm{Re}_{i1} < 2300 \\ \dfrac{(\xi_{i1}/8)\mathrm{Re}_{i1}\mathrm{Pr}}{1+12.7\sqrt{\xi_{i1}/8}\,(\mathrm{Pr}^{2/3}-1)}\left[1+\left(\dfrac{d^i_{i1}}{\bar{L}}\right)^{2/3}\right] & \text{for turbulent flow if } \mathrm{Re}_{i1} \geq 10^4 \\ (1-\gamma_{i1})\,4.364 + \gamma_{i1}\left\{\dfrac{(0.0308/8)10^4\,\mathrm{Pr}}{1+12.7\,\sqrt{0.0308/8}\,(\mathrm{Pr}^{2/3}-1)}\left[1+\left(\dfrac{d^i_{i1}}{\bar{L}}\right)^{2/3}\right]\right\} & \text{for flow in transition range if } 2300 \leq \mathrm{Re}_{i1} < 10^4 \end{cases} \tag{1-56a}$$

$$\mathrm{Nu}_{o1} = \begin{cases} 3.66 + \left[4 - \dfrac{0.102}{\left(\dfrac{d^o_{i1}}{d^i_{o1}}\right)+0.02}\right]\left(\dfrac{d^o_{i1}}{d^i_{o1}}\right)^{0.04} & \text{for } \mathrm{Re}_{o1} < 2300 \\ \dfrac{(\xi_{o1}/8)\mathrm{Re}_{o1}\mathrm{Pr}}{1+12.7\sqrt{\xi_{o1}/8}\,(\mathrm{Pr}^{2/3}-1)}\left[1+\left(\dfrac{d_h}{\bar{L}}\right)^{2/3}\right]\dfrac{0.86\left(\dfrac{d^o_{i1}}{d^i_{o1}}\right)^{0.84}+\left[1-0.14\left(\dfrac{d^o_{i1}}{d^i_{o1}}\right)^{0.6}\right]}{1+\left(\dfrac{d^o_{i1}}{d^i_{o1}}\right)} & \text{for } \mathrm{Re}_{o1} \geq 10^4 \\ (1-\gamma_{o1})\left\{3.66 + \left[4 - \dfrac{0.102}{\left(\dfrac{d^o_{i1}}{d^i_{o1}}\right)+0.02}\right]\left(\dfrac{d^o_{i1}}{d^i_{o1}}\right)^{0.04}\right\} + & \\ \quad \gamma_{o1}\left\{\dfrac{(0.0308/8)10^4\,\mathrm{Pr}}{1+12.7\,\sqrt{0.0308/8}\,(\mathrm{Pr}^{2/3}-1)}\left[1+\left(\dfrac{d_h}{\bar{L}}\right)^{2/3}\right]\dfrac{0.86\left(\dfrac{d^o_{i1}}{d^i_{o1}}\right)^{0.84}+\left[1-0.14\left(\dfrac{d^o_{i1}}{d^i_{o1}}\right)^{0.6}\right]}{1+\left(\dfrac{d^o_{i1}}{d^i_{o1}}\right)}\right\} & \text{for } 2300 \leq \mathrm{Re}_{o1} < 10^4 \end{cases} \tag{1-56b}$$

where

$$\mathrm{Pr} = \frac{\mu^r c^r}{\lambda^r} \qquad \mathrm{Re}_{i1} = \frac{|\boldsymbol{u}_{i1}|^{\mathrm{CXC}} d^i_{i1}}{(\mu^r/\rho^r)} \qquad \mathrm{Re}_{o1} = \frac{|\boldsymbol{u}_{o1}|^{\mathrm{CXC}} d_h}{(\mu^r/\rho^r)} \tag{1-57}$$

and

$$d_h = d^i_{o1} - d^o_{i1}$$

$$\xi_k = (1.8 \log_{10}\mathrm{Re}_k - 1.5)^{-2} \qquad (k = i1, o1) \tag{1-58}$$

$$\gamma_k = \frac{\mathrm{Re}_k - 2300}{10^4 - 2300} \qquad (0 \le \gamma_k \le 1)$$

$$\left.\begin{aligned} |\boldsymbol{u}_{i1}|^{\mathrm{CXC}} &= \frac{Q_r}{2\pi (r^i_{i1})^2} \\ |\boldsymbol{u}_{o1}|^{\mathrm{CXC}} &= \frac{Q_r}{2\pi [(r^i_{o1})^2 - (r^o_{i1})^2]} \end{aligned}\right\} \tag{1-59}$$

1.5.4.2 Thermal resistance due to the pipes wall material and grout transition

$$R^{\mathrm{CXC}}_{\mathrm{con}_k} = \frac{\ln(r^o_k / r^i_k)}{2\pi\lambda^p_k} \qquad (k = i1, o1) \tag{1-60}$$

$$R^{\mathrm{CXC}}_{\mathrm{con}_b} = x^{\mathrm{CXC}} R^{\mathrm{CXC}}_g \tag{1-61}$$

with

$$x^{\mathrm{CXC}} = \frac{\ln\left(\dfrac{\sqrt{D^2 + (d^o_{o1})^2}}{\sqrt{2}\, d^o_{o1}}\right)}{\ln\left(\dfrac{D}{d^o_{o1}}\right)} \tag{1-62}$$

and

$$R^{\mathrm{CXC}}_g = \frac{\ln(D / d^o_{o1})}{2\pi\lambda^g} \tag{1-63}$$

1.5.4.3 Thermal resistance due to grout-soil exchange

$$R^{\mathrm{CXC}}_{gs} = (1 - x^{\mathrm{CXC}}) R^{\mathrm{CXC}}_g \tag{1-64}$$

1.5.5 Notes to negative thermal resistances of grout for 2U and 1U exchangers

In dependence on geometric measures for 2U and 1U exchangers negative thermal resistances for grout $R^{2\mathrm{U}}_{gg1}, R^{2\mathrm{U}}_{gg2}, R^{1\mathrm{U}}_{gg}$ may occur. This is caused by the applied model conception of grout zones and can be accepted in both numerical and analytical BHE models. However, the following constraints have to be satisfied:

$$\left.\begin{aligned} \left(\frac{1}{R^{2\mathrm{U}}_{gg1}} + \frac{1}{2R^{2\mathrm{U}}_{gs}}\right)^{-1} > 0 \\ \left(\frac{1}{R^{2\mathrm{U}}_{gg2}} + \frac{1}{2R^{2\mathrm{U}}_{gs}}\right)^{-1} > 0 \end{aligned}\right\} \tag{1-65}$$

for 2U exchangers and

$$\left(\frac{1}{R^{1\mathrm{U}}_{gg}} + \frac{1}{2R^{1\mathrm{U}}_{gs}}\right)^{-1} > 0 \tag{1-66}$$

for 1U exchangers.

In cases where (1-65) or (1-66) are violated the values of x^{2U} and x^{1U}, respectively, have to be reduced until the constraints (1-65), (1-66) are met. The following correction procedure is applied:

- If (1-65) or (1-66) are violated reduce $x_{\text{new}}^{2U,1U} = \frac{2}{3} x_{\text{old}}^{2U,1U}$ and check (1-65) or (1-66).
- If (1-65) or (1-66) are still violated reduce $x_{\text{new}}^{2U,1U} = \frac{1}{3} x_{\text{old}}^{2U,1U}$ and check (1-65) or (1-66).
- If (1-65) or (1-66) are again violated set $x_{\text{new}}^{2U,1U} = 0$.

1.6 Heat Transfer Coefficients

The heat transfer coefficients $\Phi_{fig}, \Phi_{fog}, \Phi_{gg1}, \Phi_{gg2}, \Phi_{ff}, \Phi_{gg}, \Phi_{gs}$ specified for the 2U, 1U, CXA and CXC configurations are related to thermal resistance relationships R. Due to the analogy of Fourier's law for heat flow and Ohm's law for electric current flow simple formulations can be derived to lump the effects of the BHE constituents into an effective coefficient representing the reciprocal of the sum of the thermal resistances acting on their specific exchange surfaces S between the different components.

1.6.1 2U exchanger

$$\begin{aligned}
\Phi_{fig}^{2U} &= \frac{1}{R_{fig}^{2U}} \frac{1}{S_i} \\
\Phi_{fog}^{2U} &= \frac{1}{R_{fog}^{2U}} \frac{1}{S_o} \\
\Phi_{gg1}^{2U} &= \frac{1}{R_{gg1}^{2U}} \frac{1}{S_{g1}} \\
\Phi_{gg2}^{2U} &= \frac{1}{R_{gg2}^{2U}} \frac{1}{S_{g2}} \\
\Phi_{gs}^{2U} &= \frac{1}{R_{gs}^{2U}} \frac{1}{S_{gs}}
\end{aligned} \tag{1-67}$$

1.6.2 1U exchanger

$$\begin{aligned}
\Phi_{fig}^{1U} &= \frac{1}{R_{fig}^{1U}} \frac{1}{S_i} \\
\Phi_{fog}^{1U} &= \frac{1}{R_{fog}^{1U}} \frac{1}{S_o} \\
\Phi_{gg}^{1U} &= \frac{1}{R_{gg}^{1U}} \frac{1}{S_{g1}} \\
\Phi_{gs}^{1U} &= \frac{1}{R_{gs}^{1U}} \frac{1}{S_{gs}}
\end{aligned} \tag{1-68}$$

1.6.3 CXA exchanger

$$\Phi_{fig}^{CXA} = \frac{1}{R_{fig}^{CXA}} \frac{1}{S_i}$$
$$\Phi_{ff}^{CXA} = \frac{1}{R_{ff}^{CXA}} \frac{1}{S_{io}} \qquad (1\text{-}69)$$
$$\Phi_{gs}^{CXA} = \frac{1}{R_{gs}^{CXA}} \frac{1}{S_{gs}}$$

1.6.4 CXC exchanger

$$\Phi_{fog}^{CXC} = \frac{1}{R_{fog}^{CXC}} \frac{1}{S_o}$$
$$\Phi_{ff}^{CXC} = \frac{1}{R_{ff}^{CXC}} \frac{1}{S_{io}} \qquad (1\text{-}70)$$
$$\Phi_{gs}^{CXC} = \frac{1}{R_{gs}^{CXC}} \frac{1}{S_{gs}}$$

where the specific exchange surfaces S are given as follows

(1-71)

	2U	1U	CXA	CXC
S_i	$\pi d_{i1,i2}^i$	πd_{i1}^i	πd_{i1}^i	-
S_o	$\pi d_{o1,o2}^i$	πd_{o1}^i	-	πd_{o1}^i
S_{io}	-	-	πd_{o1}^i	πd_{i1}^i
S_{g1}	$\frac{1}{2}D$	D	-	-
S_{g2}	D	-	-	-
S_{gs}	$\frac{1}{4}\pi D$	$\frac{1}{2}\pi D$	πD	πD

1.7 User-specified Thermal Resistances

From practical point of view it could be useful to specify directly thermal resistances which have been measured in the field. Such field-related thermal resistances result for instance from *Thermal Response Tests*[18]. In such cases the *borehole thermal resistance* R_b and the *internal borehole thermal resistance* R_a are determined according to the definition introduced by Hellström[13]. With R_b and R_a the complete set of thermal resistances and heat transfer relationships for the

BHE models can be determined in dependence on the numerical (Al-Khoury *et al.*'s[1,2]) and analytical (Eskilson and Claesson's[12]) solution strategies.

1.7.1 Numerical BHE solution

1.7.1.1 2U exchanger

Defining

$$\left.\begin{aligned} R_{\text{adv}}^{\text{2U}} &= \frac{1}{4}(R_{\text{adv}_{i1}}^{\text{2U}} + R_{\text{adv}_{i2}}^{\text{2U}} + R_{\text{adv}_{o1}}^{\text{2U}} + R_{\text{adv}_{o2}}^{\text{2U}}) \\ R_{\text{con}}^{\text{2U}} &= \frac{1}{4}\left(R_{\text{con}_{i1}^{a}}^{\text{2U}} + R_{\text{con}_{i2}^{a}}^{\text{2U}} + R_{\text{con}_{o1}^{a}}^{\text{2U}} + R_{\text{con}_{o2}^{a}}^{\text{2U}}\right) \end{aligned}\right\} \quad (1\text{-}72)$$

we replace (1-24) by

$$R_g^{\text{2U}} = 4R_b - R_{\text{adv}}^{\text{2U}} - R_{\text{con}}^{\text{2U}} \quad (1\text{-}73)$$

and (1-27) and (1-28) by

$$R_{ar1}^{\text{2U}} = \frac{(2+\sqrt{2})R_g^{\text{2U}}(R_a - R_{\text{adv}}^{\text{2U}} - R_{\text{con}}^{\text{2U}})}{R_g^{\text{2U}} + R_a - R_{\text{adv}}^{\text{2U}} - R_{\text{con}}^{\text{2U}}} \quad (1\text{-}74)$$

$$R_{ar2}^{\text{2U}} = \sqrt{2}\, R_{ar1}^{\text{2U}} \quad (1\text{-}75)$$

1.7.1.2 1U exchanger

Defining

$$\left.\begin{aligned} R_{\text{adv}}^{\text{1U}} &= \frac{1}{2}(R_{\text{adv}_{i1}}^{\text{1U}} + R_{\text{adv}_{o1}}^{\text{1U}}) \\ R_{\text{con}}^{\text{1U}} &= \frac{1}{2}\left(R_{\text{con}_{i1}^{a}}^{\text{1U}} + R_{\text{con}_{o1}^{a}}^{\text{1U}}\right) \end{aligned}\right\} \quad (1\text{-}76)$$

we replace (1-39) by

$$R_g^{\text{1U}} = 2R_b - R_{\text{adv}}^{\text{1U}} - R_{\text{con}}^{\text{1U}} \quad (1\text{-}77)$$

and (1-41) by

$$R_{ar}^{\text{1U}} = R_a - 2(R_{\text{adv}}^{\text{1U}} + R_{\text{con}}^{\text{1U}}) \quad (1\text{-}78)$$

1.7.1.3 CXA exchanger

Replace (1-43a) by

$$R_{ff}^{\text{CXA}} = R_a \quad (1\text{-}79)$$

and (1-52) by

$$R_g^{\text{CXA}} = R_b - R_{\text{adv}_{i1}^{b}}^{\text{CXA}} - R_{\text{con}_{i1}}^{\text{CXA}}, \quad (1\text{-}80)$$

respectively.

1.7.1.4 CXC exchanger

Replace (1-54a) by

$$R_{ff}^{\text{CXC}} = R_a \quad (1\text{-}81)$$

and (1-63) by

$$R_g^{\text{CXC}} = R_b - R_{\text{adv}_{o1}^{b}}^{\text{CXC}} - R_{\text{con}_{o1}}^{\text{CXC}}, \quad (1\text{-}82)$$

respectively.

1.7.2 Analytical BHE solution

1.7.2.1 2U exchanger

Replace (1-15a) and (1-15b) by

$$R_{fig}^{2U} = 2R_b$$
$$R_{fog}^{2U} = 2R_b \qquad (1\text{-}83)$$

and (1-29) by

$$R_{gs}^{2U} = 2R_b \qquad (1\text{-}84)$$

Furthermore, we replace (1-25) and (1-26) by

$$R_{gg1}^{2U} = \frac{8R_b(R_a - 2R_b)}{4R_b - R_a} \qquad (1\text{-}85)$$

and

$$R_{gg2}^{2U} = R_{gg1}^{2U}, \qquad (1\text{-}86)$$

respectively.

1.7.2.2 1U exchanger

Replace (1-30a) and (1-30b) by

$$R_{fig}^{1U} = R_b$$
$$R_{fog}^{1U} = R_b \qquad (1\text{-}87)$$

and (1-42) by

$$R_{gs}^{1U} = R_b \qquad (1\text{-}88)$$

Furthermore, (1-40) is replaced by

$$R_{gg}^{1U} = \frac{2R_b(R_a - 2R_b)}{4R_b - R_a} \qquad (1\text{-}89)$$

1.7.2.3 CXA exchanger

Replace (1-43a) by

$$R_{ff}^{CXA} = R_a \qquad (1\text{-}90)$$

and (1-43b) by

$$R_{fig}^{CXA} = \frac{R_b}{2} \qquad (1\text{-}91)$$

as well as (1-53) by

$$R_{gs}^{CXA} = \frac{R_b}{2} \qquad (1\text{-}92)$$

1.7.2.4 CXC exchanger

Replace (1-54a) by

$$R_{ff}^{CXC} = R_a \qquad (1\text{-}93)$$

and (1-54b) by

$$R_{fog}^{CXC} = \frac{R_b}{2} \qquad (1\text{-}94)$$

as well as (1-64) by

$$R_{gs}^{CXC} = \frac{R_b}{2} \qquad (1\text{-}95)$$

1.8 Finite Element Discretization of the Local Problem

equations (1-10a) to (1-10h), which will be discretized by finite elements. Introducing the spatial weighting function w the following integral formulations hold

1.8.1 Weak statements

1.8.1.1 2U exchanger

We start with the more general 2U heat transport

$$\int_{\Omega_{i1}}\left[w\rho^r c^r\left(\frac{\partial T_{i1}}{\partial t}+\boldsymbol{u}\cdot\nabla T_{i1}\right)+\nabla w\cdot(\boldsymbol{\Lambda}^r\cdot\nabla T_{i1})\right]d\Omega+\int_{\Gamma_{i1}} w\Phi^{2U}_{fig}T_{i1}d\Gamma=\int_{\Gamma_{i1}} w\Phi^{2U}_{fig}T_{g1}d\Gamma+\int_{\Omega_{i1}} wH_{i1}d\Omega \tag{1-96a}$$

$$\int_{\Omega_{i2}}\left[w\rho^r c^r\left(\frac{\partial T_{i2}}{\partial t}+\boldsymbol{u}\cdot\nabla T_{i2}\right)+\nabla w\cdot(\boldsymbol{\Lambda}^r\cdot\nabla T_{i2})\right]d\Omega+\int_{\Gamma_{i2}} w\Phi^{2U}_{fig}T_{i2}d\Gamma=\int_{\Gamma_{i2}} w\Phi^{2U}_{fig}T_{g2}d\Gamma+\int_{\Omega_{i2}} wH_{i2}d\Omega \tag{1-96b}$$

$$\int_{\Omega_{o1}}\left[w\rho^r c^r\left(\frac{\partial T_{o1}}{\partial t}+\boldsymbol{u}\cdot\nabla T_{o1}\right)+\nabla w\cdot(\boldsymbol{\Lambda}^r\cdot\nabla T_{o1})\right]d\Omega+\int_{\Gamma_{o1}} w\Phi^{2U}_{fog}T_{o1}d\Gamma=\int_{\Gamma_{o1}} w\Phi^{2U}_{fog}T_{g3}d\Gamma+\int_{\Omega_{o1}} wH_{o1}d\Omega \tag{1-96c}$$

$$\int_{\Omega_{o2}}\left[w\rho^r c^r\left(\frac{\partial T_{o2}}{\partial t}+\boldsymbol{u}\cdot\nabla T_{o2}\right)+\nabla w\cdot(\boldsymbol{\Lambda}^r\cdot\nabla T_{o2})\right]d\Omega+\int_{\Gamma_{o2}} w\Phi^{2U}_{fog}T_{o2}d\Gamma=\int_{\Gamma_{o2}} w\Phi^{2U}_{fog}T_{g4}d\Gamma+\int_{\Omega_{o2}} wH_{o2}d\Omega \tag{1-96d}$$

$$\int_{\Omega_{g1}}\left[w\varepsilon_g\rho^g c^g\frac{\partial T_{g1}}{\partial t}+\nabla w\cdot(\varepsilon_g\lambda^g\nabla T_{g1})\right]d\Omega+\int_{\Gamma_{g1}} w(\Phi^{2U}_{gs}+\Phi^{2U}_{fig}+\Phi^{2U}_{gg2}+2\Phi^{2U}_{gg1})T_{g1}d\Gamma \tag{1-96e}$$
$$=\int_{\Gamma_{g1}} w(\Phi^{2U}_{gs}T_s+\Phi^{2U}_{fig}T_{i1}+\Phi^{2U}_{gg2}T_{g2}+\Phi^{2U}_{gg1}T_{g3}+\Phi^{2U}_{gg1}T_{g4})d\Gamma+\int_{\Omega_{g1}} wH_{g1}d\Omega$$

$$\int_{\Omega_{g2}}\left[w\varepsilon_g\rho^g c^g\frac{\partial T_{g2}}{\partial t}+\nabla w\cdot(\varepsilon_g\lambda^g\nabla T_{g2})\right]d\Omega+\int_{\Gamma_{g2}} w(\Phi^{2U}_{gs}+\Phi^{2U}_{fig}+\Phi^{2U}_{gg2}+2\Phi^{2U}_{gg1})T_{g2}d\Gamma \tag{1-96f}$$
$$=\int_{\Gamma_{g2}} w(\Phi^{2U}_{gs}T_s+\Phi^{2U}_{fig}T_{i2}+\Phi^{2U}_{gg2}T_{g1}+\Phi^{2U}_{gg1}T_{g3}+\Phi^{2U}_{gg1}T_{g4})d\Gamma+\int_{\Omega_{g2}} wH_{g2}d\Omega$$

$$\int_{\Omega_{g3}} \left[w\varepsilon_g \rho^g c^g \frac{\partial T_{g3}}{\partial t} + \nabla w \cdot (\varepsilon_g \lambda^g \nabla T_{g3}) \right] d\Omega + \int_{\Gamma_{g3}} w(\Phi_{gs}^{2U} + \Phi_{fog}^{2U} + \Phi_{gg2}^{2U} + 2\Phi_{gg1}^{2U}) T_{g3} d\Gamma \tag{1-96g}$$
$$= \int_{\Gamma_{g3}} w(\Phi_{gs}^{2U} T_s + \Phi_{fog}^{2U} T_{o1} + \Phi_{gg2}^{2U} T_{g4} + \Phi_{gg1}^{2U} T_{g1} + \Phi_{gg1}^{2U} T_{g2}) d\Gamma + \int_{\Omega_{g3}} w H_{g3} d\Omega$$

$$\int_{\Omega_{g4}} \left[w\varepsilon_g \rho^g c^g \frac{\partial T_{g4}}{\partial t} + \nabla w \cdot (\varepsilon_g \lambda^g \nabla T_{g4}) \right] d\Omega + \int_{\Gamma_{g4}} w(\Phi_{gs}^{2U} + \Phi_{fog}^{2U} + \Phi_{gg2}^{2U} + 2\Phi_{gg1}^{2U}) T_{g4} d\Gamma \tag{1-96h}$$
$$= \int_{\Gamma_{g4}} w(\Phi_{gs}^{2U} T_s + \Phi_{fog}^{2U} T_{o2} + \Phi_{gg2}^{2U} T_{g3} + \Phi_{gg1}^{2U} T_{g1} + \Phi_{gg1}^{2U} T_{g2}) d\Gamma + \int_{\Omega_{g4}} w H_{g4} d\Omega$$

1.8.1.2 1U exchanger

For the 1U exchanger configuration the equations (1-96b), (1-96d), (1-96g) and (1-96h) become irrelevant. We obtain

$$\int_{\Omega_{i1}} \left[w\rho^r c^r \left(\frac{\partial T_{i1}}{\partial t} + \boldsymbol{u} \cdot \nabla T_{i1} \right) + \nabla w \cdot (\boldsymbol{\Lambda}^r \cdot \nabla T_{i1}) \right] d\Omega + \int_{\Gamma_{i1}} w\Phi_{fig}^{1U} T_{i1} d\Gamma = \int_{\Gamma_{i1}} w\Phi_{fig}^{1U} T_{g1} d\Gamma + \int_{\Omega_{i1}} w H_{i1} d\Omega \tag{1-97a}$$

$$\int_{\Omega_{o1}} \left[w\rho^r c^r \left(\frac{\partial T_{o1}}{\partial t} + \boldsymbol{u} \cdot \nabla T_{o1} \right) + \nabla w \cdot (\boldsymbol{\Lambda}^r \cdot \nabla T_{o1}) \right] d\Omega + \int_{\Gamma_{o1}} w\Phi_{fog}^{1U} T_{o1} d\Gamma = \int_{\Gamma_{o1}} w\Phi_{fog}^{1U} T_{g2} d\Gamma + \int_{\Omega_{o1}} w H_{o1} d\Omega \tag{1-97b}$$

$$\int_{\Omega_{g1}} \left[w\varepsilon_g \rho^g c^g \frac{\partial T_{g1}}{\partial t} + \nabla w \cdot (\varepsilon_g \lambda^g \nabla T_{g1}) \right] d\Omega + \int_{\Gamma_{g1}} w(\Phi_{gs}^{1U} + \Phi_{fig}^{1U} + \Phi_{gg}^{1U}) T_{g1} d\Gamma \tag{1-97c}$$
$$= \int_{\Gamma_{g1}} w(\Phi_{gs}^{1U} T_s + \Phi_{fig}^{1U} T_{i1} + \Phi_{gg}^{1U} T_{g2}) d\Gamma + \int_{\Omega_{g1}} w H_{g1} d\Omega$$

$$\int_{\Omega_{g2}} \left[w\varepsilon_g \rho^g c^g \frac{\partial T_{g2}}{\partial t} + \nabla w \cdot (\varepsilon_g \lambda^g \nabla T_{g2}) \right] d\Omega + \int_{\Gamma_{g2}} w(\Phi_{gs}^{1U} + \Phi_{fog}^{1U} + \Phi_{gg}^{1U}) T_{g2} d\Gamma \tag{1-97d}$$
$$= \int_{\Gamma_{g2}} w(\Phi_{gs}^{1U} T_s + \Phi_{fog}^{1U} T_{o1} + \Phi_{gg}^{1U} T_{g1}) d\Gamma + \int_{\Omega_{g2}} w H_{g2} d\Omega$$

are more specific. They read for the CXA type

1.8.1.3 CXA exchanger

The formulations for the coaxial pipe configurations

$$\int_{\Omega_{i1}} \left[w\rho^r c^r \left(\frac{\partial T_{i1}}{\partial t} + \boldsymbol{u} \cdot \nabla T_{i1} \right) + \nabla w \cdot (\boldsymbol{\Lambda}^r \cdot \nabla T_{i1}) \right] d\Omega + \int_{\Gamma_{i1}} w(\Phi_{fig}^{\mathrm{CXA}} + \Phi_{ff}^{\mathrm{CXA}}) T_{i1} d\Gamma \tag{1-98a}$$
$$= \int_{\Gamma_{i1}} w(\Phi_{fig}^{\mathrm{CXA}} T_{g1} + \Phi_{ff}^{\mathrm{CXA}} T_{o1}) d\Gamma + \int_{\Omega_{i1}} w H_{i1} d\Omega$$

$$\int_{\Omega_{o1}} \left[w\rho^r c^r \left(\frac{\partial T_{o1}}{\partial t} + \boldsymbol{u} \cdot \nabla T_{o1} \right) + \nabla w \cdot (\boldsymbol{\Lambda}^r \cdot \nabla T_{o1}) \right] d\Omega + \int_{\Gamma_{o1}} w \Phi_{ff}^{\mathrm{CXA}} T_{o1} d\Gamma \tag{1-98b}$$
$$= \int_{\Gamma_{o1}} w \Phi_{ff}^{\mathrm{CXA}} T_{i1} d\Gamma + \int_{\Omega_{o1}} w H_{o1} d\Omega$$

$$\int_{\Omega_{g1}} \left[w\varepsilon_g \rho^g c^g \frac{\partial T_{g1}}{\partial t} + \nabla w \cdot (\varepsilon_g \lambda^g \nabla T_{g1}) \right] d\Omega + \int_{\Gamma_{g1}} w(\Phi_{gs}^{\mathrm{CXA}} + \Phi_{fig}^{\mathrm{CXA}}) T_{g1} d\Gamma \tag{1-98c}$$
$$= \int_{\Gamma_{g1}} w(\Phi_{gs}^{\mathrm{CXA}} T_s + \Phi_{fig}^{\mathrm{CXA}} T_{i1}) d\Gamma + \int_{\Omega_{g1}} w H_{g1} d\Omega$$

1.8.1.4 CXC exchanger

The formulations for the CXC type read

$$\int_{\Omega_{i1}} \left[w\rho^r c^r \left(\frac{\partial T_{i1}}{\partial t} + \boldsymbol{u} \cdot \nabla T_{i1} \right) + \nabla w \cdot (\boldsymbol{\Lambda}^r \cdot \nabla T_{i1}) \right] d\Omega + \int_{\Gamma_{i1}} w \Phi_{ff}^{\mathrm{CXC}} T_{i1} d\Gamma \tag{1-99a}$$
$$= \int_{\Gamma_{i1}} w(\Phi_{ff}^{\mathrm{CXC}} T_{o1}) d\Gamma + \int_{\Omega_{i1}} w H_{i1} d\Omega$$

$$\int_{\Omega_{o1}} \left[w\rho^r c^r \left(\frac{\partial T_{o1}}{\partial t} + \boldsymbol{u} \cdot \nabla T_{o1} \right) + \nabla w \cdot (\boldsymbol{\Lambda}^r \cdot \nabla T_{o1}) \right] d\Omega + \int_{\Gamma_{o1}} w(\Phi_{fog}^{\mathrm{CXC}} + \Phi_{ff}^{\mathrm{CXC}}) T_{o1} d\Gamma \tag{1-99b}$$
$$= \int_{\Gamma_{o1}} w(\Phi_{fog}^{\mathrm{CXC}} T_{g1} + \Phi_{ff}^{\mathrm{CXC}} T_{i1}) d\Gamma + \int_{\Omega_{o1}} w H_{o1} d\Omega$$

$$\int_{\Omega_{g1}} \left[w\varepsilon_g \rho^g c^g \frac{\partial T_{g1}}{\partial t} + \nabla w \cdot (\varepsilon_g \lambda^g \nabla T_{g1}) \right] d\Omega + \int_{\Gamma_{g1}} w(\Phi_{gs}^{\mathrm{CXC}} + \Phi_{fog}^{\mathrm{CXC}}) T_{g1} d\Gamma \tag{1-99c}$$
$$= \int_{\Gamma_{g1}} w(\Phi_{gs}^{\mathrm{CXC}} T_s + \Phi_{fog}^{\mathrm{CXC}} T_{o1}) d\Gamma + \int_{\Omega_{g1}} w H_{g1} d\Omega$$

1.8.2 Spatial discretization

Using the Galerkin-based finite element method (FEM), where the test function w becomes identical to the trial space $\boldsymbol{N}$, equations (1-96a) to (1-99c) lead to the following generalized matrix system

$$\boldsymbol{O} \cdot \dot{\boldsymbol{T}} + \boldsymbol{D} \cdot \boldsymbol{T} = \boldsymbol{F}$$

$$\begin{bmatrix} \boldsymbol{O}_i & 0 & 0 & 0 & 0 & 0 & 0 & 0 \\ 0 & \boldsymbol{O}_i & 0 & 0 & 0 & 0 & 0 & 0 \\ 0 & 0 & \boldsymbol{O}_o & 0 & 0 & 0 & 0 & 0 \\ 0 & 0 & 0 & \boldsymbol{O}_o & 0 & 0 & 0 & 0 \\ 0 & 0 & 0 & 0 & \boldsymbol{O}_{g1} & 0 & 0 & 0 \\ 0 & 0 & 0 & 0 & 0 & \boldsymbol{O}_{g2} & 0 & 0 \\ 0 & 0 & 0 & 0 & 0 & 0 & \boldsymbol{O}_{g3} & 0 \\ 0 & 0 & 0 & 0 & 0 & 0 & 0 & \boldsymbol{O}_{g4} \end{bmatrix} \cdot \begin{Bmatrix} \dot{\boldsymbol{T}}_{i1} \\ \dot{\boldsymbol{T}}_{i2} \\ \dot{\boldsymbol{T}}_{o1} \\ \dot{\boldsymbol{T}}_{o2} \\ \dot{\boldsymbol{T}}_{g1} \\ \dot{\boldsymbol{T}}_{g2} \\ \dot{\boldsymbol{T}}_{g3} \\ \dot{\boldsymbol{T}}_{g4} \end{Bmatrix} + \begin{bmatrix} \boldsymbol{K}_{i1} & 0 & \boldsymbol{R}_{io} & 0 & \boldsymbol{R}_i & 0 & 0 & 0 \\ 0 & \boldsymbol{K}_{i2} & 0 & 0 & 0 & \boldsymbol{R}_i & 0 & 0 \\ \boldsymbol{R}_{io} & 0 & \boldsymbol{K}_{o1} & 0 & 0 & 0 & \boldsymbol{R}_o & 0 \\ 0 & 0 & 0 & \boldsymbol{K}_{o2} & 0 & 0 & 0 & \boldsymbol{R}_o \\ \boldsymbol{R}_i & 0 & 0 & 0 & \boldsymbol{K}_{ig} & \boldsymbol{R}_{g2} & \boldsymbol{R}_{g1} & \boldsymbol{R}_{g1} \\ 0 & \boldsymbol{R}_i & 0 & 0 & \boldsymbol{R}_{g2} & \boldsymbol{K}_{ig} & \boldsymbol{R}_{g1} & \boldsymbol{R}_{g1} \\ 0 & 0 & \boldsymbol{R}_o & 0 & \boldsymbol{R}_{g1} & \boldsymbol{R}_{g1} & \boldsymbol{K}_{og} & \boldsymbol{R}_{g2} \\ 0 & 0 & 0 & \boldsymbol{R}_o & \boldsymbol{R}_{g1} & \boldsymbol{R}_{g1} & \boldsymbol{R}_{g2} & \boldsymbol{K}_{og} \end{bmatrix} \cdot \begin{Bmatrix} \boldsymbol{T}_{i1} \\ \boldsymbol{T}_{i2} \\ \boldsymbol{T}_{o1} \\ \boldsymbol{T}_{o2} \\ \boldsymbol{T}_{g1} \\ \boldsymbol{T}_{g2} \\ \boldsymbol{T}_{g3} \\ \boldsymbol{T}_{g4} \end{Bmatrix} = \begin{Bmatrix} \boldsymbol{F}_{i1} \\ \boldsymbol{F}_{i2} \\ \boldsymbol{F}_{o1} \\ \boldsymbol{F}_{o2} \\ \boldsymbol{F}_{g1} - \boldsymbol{R}_s \cdot \boldsymbol{T}_s \\ \boldsymbol{F}_{g2} - \boldsymbol{R}_s \cdot \boldsymbol{T}_s \\ \boldsymbol{F}_{g3} - \boldsymbol{R}_s \cdot \boldsymbol{T}_s \\ \boldsymbol{F}_{g4} - \boldsymbol{R}_s \cdot \boldsymbol{T}_s \end{Bmatrix} \tag{1-100}$$

with

$$\boldsymbol{O}_i = \sum_e \int_{\Omega^e_{i1,\,i2}} \rho^r c^r \boldsymbol{N}^T \boldsymbol{N} d\Omega$$

$$\boldsymbol{O}_o = \sum_e \int_{\Omega^e_{o1,\,o2}} \rho^r c^r \boldsymbol{N}^T \boldsymbol{N} d\Omega \qquad \text{(1-101a)}$$

$$\boldsymbol{O}_{gi} = \sum_e \int_{\Omega^e_{gi}} \varepsilon_g \rho^g c^g \boldsymbol{N}^T \boldsymbol{N} d\Omega \qquad (i = 1, \ldots, G)$$

$$\begin{aligned}
\boldsymbol{K}_{i1} &= \boldsymbol{C}_i - \boldsymbol{R}_i - \boldsymbol{R}_{io} \\
\boldsymbol{K}_{i2} &= \boldsymbol{C}_i - \boldsymbol{R}_i \\
\boldsymbol{K}_{o1} &= \boldsymbol{C}_o - \boldsymbol{R}_o - \boldsymbol{R}_{io} \\
\boldsymbol{K}_{o2} &= \boldsymbol{C}_o - \boldsymbol{R}_o \\
\boldsymbol{K}_{ig} &= \boldsymbol{G}_i - \boldsymbol{R}_i - 2\boldsymbol{R}_{g1} - \boldsymbol{R}_{g2} - \boldsymbol{R}_s \\
\boldsymbol{K}_{og} &= \boldsymbol{G}_o - \boldsymbol{R}_o - 2\boldsymbol{R}_{g1} - \boldsymbol{R}_{g2} - \boldsymbol{R}_s
\end{aligned} \qquad \text{(1-101b)}$$

$$\boldsymbol{C}_i = \sum_e \int_{\Omega^e_{i1,\,i2}} (\rho^r c^r \boldsymbol{u} \cdot \boldsymbol{N}^T \nabla \boldsymbol{N} + \boldsymbol{\Lambda}^r \cdot \nabla \boldsymbol{N}^T \nabla \boldsymbol{N}) d\Omega$$

$$\boldsymbol{C}_o = \sum_e \int_{\Omega^e_{o1,\,o2}} (\rho^r c^r \boldsymbol{u} \cdot \boldsymbol{N}^T \nabla \boldsymbol{N} + \boldsymbol{\Lambda}^r \cdot \nabla \boldsymbol{N}^T \nabla \boldsymbol{N}) d\Omega \qquad \text{(1-101c)}$$

$$\boldsymbol{G}_i = \sum_e \int_{\Omega^e_{g1,\,g2}} (\varepsilon_g \lambda^g \nabla \boldsymbol{N}^T \nabla \boldsymbol{N}) d\Omega$$

$$\boldsymbol{G}_o = \sum_e \int_{\Omega^e_{g3,\,g4}} (\varepsilon_g \lambda^g \nabla \boldsymbol{N}^T \nabla \boldsymbol{N}) d\Omega \qquad \text{(1-101d)}$$

and

$$\begin{aligned}
\boldsymbol{F}_{i1} &= \sum_e \int_{\Omega^e_{i1}} H_{i1} \boldsymbol{N}^T d\Omega \\
\boldsymbol{F}_{i2} &= \sum_e \int_{\Omega^e_{i2}} H_{i2} \boldsymbol{N}^T d\Omega \\
\boldsymbol{F}_{o1} &= \sum_e \int_{\Omega^e_{o1}} H_{o1} \boldsymbol{N}^T d\Omega \\
\boldsymbol{F}_{o2} &= \sum_e \int_{\Omega^e_{o2}} H_{o2} \boldsymbol{N}^T d\Omega \\
\boldsymbol{F}_{g1} &= \sum_e \int_{\Omega^e_{g1}} H_{g1} \boldsymbol{N}^T d\Omega \\
\boldsymbol{F}_{g2} &= \sum_e \int_{\Omega^e_{g2}} H_{g2} \boldsymbol{N}^T d\Omega \\
\boldsymbol{F}_{g3} &= \sum_e \int_{\Omega^e_{g3}} H_{g3} \boldsymbol{N}^T d\Omega \\
\boldsymbol{F}_{g4} &= \sum_e \int_{\Omega^e_{g4}} H_{g4} \boldsymbol{N}^T d\Omega
\end{aligned} \qquad \text{(1-101e)}$$

(1-101f)

	2U	1U	CXA	CXC
$\boldsymbol{R}_i$	$-\sum_e \int_{\Gamma^e_{i1,i2}} \Phi^{2U}_{fig} \boldsymbol{N}^T \boldsymbol{N} d\Gamma$	$-\sum_e \int_{\Gamma^e_{i1}} \Phi^{1U}_{fig} \boldsymbol{N}^T \boldsymbol{N} d\Gamma$	$-\sum_e \int_{\Gamma^e_{i1}} \Phi^{CXA}_{fig} \boldsymbol{N}^T \boldsymbol{N} d\Gamma$	0
$\boldsymbol{R}_o$	$-\sum_e \int_{\Gamma^e_{o1,o2}} \Phi^{2U}_{fog} \boldsymbol{N}^T \boldsymbol{N} d\Gamma$	$-\sum_e \int_{\Gamma^e_{o1}} \Phi^{1U}_{fog} \boldsymbol{N}^T \boldsymbol{N} d\Gamma$	0	$-\sum_e \int_{\Gamma^e_{o1}} \Phi^{CXC}_{fog} \boldsymbol{N}^T \boldsymbol{N} d\Gamma$
$\boldsymbol{R}_{io}$	0	0	$-\sum_e \int_{\Gamma^e_{o1}} \Phi^{CXA}_{ff} \boldsymbol{N}^T \boldsymbol{N} d\Gamma$	$-\sum_e \int_{\Gamma^e_{i1}} \Phi^{CXC}_{ff} \boldsymbol{N}^T \boldsymbol{N} d\Gamma$
$\boldsymbol{R}_{g1}$	$-\sum_e \int_{\Gamma^e_{g1,g2,g3,g4}} \Phi^{2U}_{gg1} \boldsymbol{N}^T \boldsymbol{N} d\Gamma$	$-\sum_e \int_{\Gamma^e_{g1,g2}} \Phi^{1U}_{gg} \boldsymbol{N}^T \boldsymbol{N} d\Gamma$	0	0
$\boldsymbol{R}_{g2}$	$-\sum_e \int_{\Gamma^e_{g1,g2,g3,g4}} \Phi^{2U}_{gg2} \boldsymbol{N}^T \boldsymbol{N} d\Gamma$	0	0	0
$\boldsymbol{R}_s$	$-\sum_e \int_{\Gamma^e_{g1,g2,g3,g4}} \Phi^{2U}_{gs} \boldsymbol{N}^T \boldsymbol{N} d\Gamma$	$-\sum_e \int_{\Gamma^e_{g1,g2}} \Phi^{1U}_{gs} \boldsymbol{N}^T \boldsymbol{N} d\Gamma$	$-\sum_e \int_{\Gamma^e_{g1}} \Phi^{CXA}_{gs} \boldsymbol{N}^T \boldsymbol{N} d\Gamma$	$-\sum_e \int_{\Gamma^e_{g1}} \Phi^{CXC}_{gs} \boldsymbol{N}^T \boldsymbol{N} d\Gamma$

The symbolic $\Omega^e_{i1,i2}, \Gamma^e_{i1,i2}$ denotes the domain and surface of pipe(s)-in, $\Omega^e_{o1,o2}, \Gamma^e_{o1,o2}$ for pipe(s)-out and $\Omega^e_{gi}, \Gamma^e_{gi}$ $(i = 1, \ldots, G)$ for the grout zones of finite element e. Analytical (explicit) integration of the matrices of (1-101a) to (1-101f) is given in Appendix A.

1.8.3 Streamline upwind scheme

If the advective part in the heat transport equations of the BHE pipes becomes dominant, wiggles in the solutions can occur and the spatial discretization with the standard methods (Galerkin-FEM) is insufficient. A common technique is the streamline upwind scheme, which introduces a balancing diffusivity to produce stabilized wiggle-free (smooth) solutions[11]. It is equivalent to modifying the thermal dispersion tensor (1-11) for the refrigerant in the 1D pipes according to

$$\boldsymbol{\Lambda}^r = [\lambda^r + \rho^r c^r (\alpha_L + \alpha_L^{\text{num}}) \|\boldsymbol{u}\|] \boldsymbol{I} \qquad (1\text{-}102)$$

with a numerical thermo-dispersivity $\alpha_L^{\text{num}} = \kappa L/2$ derived for linear finite elements, where L corresponds to the length of the 1D pipe element and $\kappa \in (0, 1)$ represents an upwind parameter which can be taken with $\kappa = 0$ for the Galerkin-FEM and with $\kappa = 1$ for the streamline upwind scheme.

1.8.4 Temporal discretization

1.8.4.1 θ-method

Introducing a weighting coefficient $(0 \le \theta \le 1)$, common time stepping schemes result if choosing θ in an appropriate manner, *viz*.,

$\theta = 0$	explicit scheme	
$\theta = 1/2$	trapezoid rule (Crank-Nicolson scheme)	(1-103)
$\theta = 1$	implicit scheme	

The θ-method results the following matrix system from

$$\left(\frac{\boldsymbol{O}}{\Delta t_n} + \boldsymbol{D}\theta\right)\boldsymbol{T}^{n+1} = \left(\frac{\boldsymbol{O}}{\Delta t_n} - \boldsymbol{D}(1-\theta)\right)\boldsymbol{T}^{n} + (\boldsymbol{F}^{n+1}\theta + \boldsymbol{F}^{n}(1-\theta)) \tag{1-104a}$$

with

$$
\begin{bmatrix}
\frac{\boldsymbol{O}_i}{\Delta t_n}+\boldsymbol{K}_{i1}\theta & 0 & \boldsymbol{R}_{io}\theta & 0 & \boldsymbol{R}_i\theta & 0 & 0 & 0 \\
0 & \frac{\boldsymbol{O}_i}{\Delta t_n}+\boldsymbol{K}_{i2}\theta & 0 & 0 & 0 & \boldsymbol{R}_i\theta & 0 & 0 \\
\boldsymbol{R}_{io}\theta & 0 & \frac{\boldsymbol{O}_o}{\Delta t_n}+\boldsymbol{K}_{o1}\theta & 0 & 0 & 0 & \boldsymbol{R}_o\theta & 0 \\
0 & 0 & 0 & \frac{\boldsymbol{O}_o}{\Delta t_n}+\boldsymbol{K}_{o2}\theta & 0 & 0 & 0 & \boldsymbol{R}_o\theta \\
\boldsymbol{R}_i\theta & 0 & 0 & 0 & \frac{\boldsymbol{O}_{g1}}{\Delta t_n}+\boldsymbol{K}_{ig}\theta & \boldsymbol{R}_{g2}\theta & \boldsymbol{R}_{g1}\theta & \boldsymbol{R}_{g1}\theta \\
0 & \boldsymbol{R}_i\theta & 0 & 0 & \boldsymbol{R}_{g2}\theta & \frac{\boldsymbol{O}_{g2}}{\Delta t_n}+\boldsymbol{K}_{ig}\theta & \boldsymbol{R}_{g1}\theta & \boldsymbol{R}_{g1}\theta \\
0 & 0 & \boldsymbol{R}_o\theta & 0 & \boldsymbol{R}_{g1}\theta & \boldsymbol{R}_{g1}\theta & \frac{\boldsymbol{O}_{g3}}{\Delta t_n}+\boldsymbol{K}_{og}\theta & \boldsymbol{R}_{g2}\theta \\
0 & 0 & 0 & \boldsymbol{R}_o\theta & \boldsymbol{R}_{g1}\theta & \boldsymbol{R}_{g1}\theta & \boldsymbol{R}_{g2}\theta & \frac{\boldsymbol{O}_{g4}}{\Delta t_n}+\boldsymbol{K}_{og}\theta
\end{bmatrix}
\cdot
\begin{Bmatrix}
\boldsymbol{T}_{i1} \\ \boldsymbol{T}_{i2} \\ \boldsymbol{T}_{o1} \\ \boldsymbol{T}_{o2} \\ \boldsymbol{T}_{g1} \\ \boldsymbol{T}_{g2} \\ \boldsymbol{T}_{g3} \\ \boldsymbol{T}_{g4}
\end{Bmatrix}^{n+1}
$$

$$
=
\begin{bmatrix}
\frac{\boldsymbol{O}_i}{\Delta t_n}-\boldsymbol{K}_{i1}(1-\theta) & 0 & -\boldsymbol{R}_{io}(1-\theta) & 0 & -\boldsymbol{R}_i(1-\theta) & 0 & 0 & 0 \\
0 & \frac{\boldsymbol{O}_i}{\Delta t_n}-\boldsymbol{K}_{i2}(1-\theta) & 0 & 0 & 0 & -\boldsymbol{R}_i(1-\theta) & 0 & 0 \\
-\boldsymbol{R}_{io}(1-\theta) & 0 & \frac{\boldsymbol{O}_o}{\Delta t_n}-\boldsymbol{K}_{o1}(1-\theta) & 0 & 0 & 0 & -\boldsymbol{R}_o(1-\theta) & 0 \\
0 & 0 & 0 & \frac{\boldsymbol{O}_o}{\Delta t_n}-\boldsymbol{K}_{o2}(1-\theta) & 0 & 0 & 0 & -\boldsymbol{R}_o(1-\theta) \\
-\boldsymbol{R}_i(1-\theta) & 0 & 0 & 0 & \frac{\boldsymbol{O}_{g1}}{\Delta t_n}-\boldsymbol{K}_{ig}(1-\theta) & -\boldsymbol{R}_{g2}(1-\theta) & -\boldsymbol{R}_{g1}(1-\theta) & -\boldsymbol{R}_{g1}(1-\theta) \\
0 & -\boldsymbol{R}_i(1-\theta) & 0 & 0 & -\boldsymbol{R}_{g2}(1-\theta) & \frac{\boldsymbol{O}_{g2}}{\Delta t_n}-\boldsymbol{K}_{ig}(1-\theta) & -\boldsymbol{R}_{g1}(1-\theta) & -\boldsymbol{R}_{g1}(1-\theta) \\
0 & 0 & -\boldsymbol{R}_o(1-\theta) & 0 & -\boldsymbol{R}_{g1}(1-\theta) & -\boldsymbol{R}_{g1}(1-\theta) & \frac{\boldsymbol{O}_{g3}}{\Delta t_n}-\boldsymbol{K}_{og}(1-\theta) & -\boldsymbol{R}_{g2}(1-\theta) \\
0 & 0 & 0 & -\boldsymbol{R}_o(1-\theta) & -\boldsymbol{R}_{g1}(1-\theta) & -\boldsymbol{R}_{g1}(1-\theta) & -\boldsymbol{R}_{g2}(1-\theta) & \frac{\boldsymbol{O}_{g4}}{\Delta t_n}-\boldsymbol{K}_{og}(1-\theta)
\end{bmatrix}
\cdot
\begin{Bmatrix}
\boldsymbol{T}_{i1} \\ \boldsymbol{T}_{i2} \\ \boldsymbol{T}_{o1} \\ \boldsymbol{T}_{o2} \\ \boldsymbol{T}_{g1} \\ \boldsymbol{T}_{g2} \\ \boldsymbol{T}_{g3} \\ \boldsymbol{T}_{g4}
\end{Bmatrix}^{n}
+
$$

(1-104b)

$$
\theta
\begin{Bmatrix}
\boldsymbol{F}_{i1} \\ \boldsymbol{F}_{i2} \\ \boldsymbol{F}_{o1} \\ \boldsymbol{F}_{o2} \\ \boldsymbol{F}_{g1} \\ \boldsymbol{F}_{g2} \\ \boldsymbol{F}_{g3} \\ \boldsymbol{F}_{g4}
\end{Bmatrix}^{n+1}
+(1-\theta)
\begin{Bmatrix}
\boldsymbol{F}_{i1} \\ \boldsymbol{F}_{i2} \\ \boldsymbol{F}_{o1} \\ \boldsymbol{F}_{o2} \\ \boldsymbol{F}_{g1} \\ \boldsymbol{F}_{g2} \\ \boldsymbol{F}_{g3} \\ \boldsymbol{F}_{g4}
\end{Bmatrix}^{n}
-
\begin{Bmatrix}
0 \\ 0 \\ 0 \\ 0 \\ \boldsymbol{R}_s \cdot \boldsymbol{T}_s \\ \boldsymbol{R}_s \cdot \boldsymbol{T}_s \\ \boldsymbol{R}_s \cdot \boldsymbol{T}_s \\ \boldsymbol{R}_s \cdot \boldsymbol{T}_s
\end{Bmatrix}^{n+1}
$$

where the subscript n denotes the time plane and Δt_n is a variable time step length.

1.8.4.2 Predictor-corrector method

For the fully implicit backward Euler (BE) scheme

$$\left(\frac{\boldsymbol{O}}{\theta\Delta t_n}+\boldsymbol{D}\right)\boldsymbol{T}^{n+1} = \boldsymbol{O}\left[\frac{\boldsymbol{T}^n}{\theta\Delta t_n}+\left(\frac{1}{\theta}-1\right)\dot{\boldsymbol{T}}^n\right]+\boldsymbol{F}^{n+1} \tag{1-105a}$$

$$\begin{bmatrix}
\frac{\boldsymbol{O}_i}{\theta\Delta t_n}+\boldsymbol{K}_{i1} & 0 & \boldsymbol{R}_{io} & 0 & \boldsymbol{R}_i & 0 & 0 & 0\\
0 & \frac{\boldsymbol{O}_i}{\theta\Delta t_n}+\boldsymbol{K}_{i2} & 0 & 0 & 0 & \boldsymbol{R}_i & 0 & 0\\
\boldsymbol{R}_{io} & 0 & \frac{\boldsymbol{O}_o}{\Delta t_n}+\boldsymbol{K}_{o1} & 0 & 0 & 0 & \boldsymbol{R}_o & 0\\
0 & 0 & 0 & \frac{\boldsymbol{O}_o}{\theta\Delta t_n}+\boldsymbol{K}_{o2} & 0 & 0 & 0 & \boldsymbol{R}_o\\
\boldsymbol{R}_i & 0 & 0 & 0 & \frac{\boldsymbol{O}_{g1}}{\theta\Delta t_n}+\boldsymbol{K}_{ig} & \boldsymbol{R}_{g2} & \boldsymbol{R}_{g1} & \boldsymbol{R}_{g1}\\
0 & \boldsymbol{R}_i & 0 & 0 & \boldsymbol{R}_{g2} & \frac{\boldsymbol{O}_{g2}}{\theta\Delta t_n}+\boldsymbol{K}_{ig} & \boldsymbol{R}_{g1} & \boldsymbol{R}_{g1}\\
0 & 0 & \boldsymbol{R}_o & 0 & \boldsymbol{R}_{g1} & \boldsymbol{R}_{g1} & \frac{\boldsymbol{O}_{g3}}{\theta\Delta t_n}+\boldsymbol{K}_{og} & \boldsymbol{R}_{g2}\\
0 & 0 & 0 & \boldsymbol{R}_o & \boldsymbol{R}_{g1} & \boldsymbol{R}_{g1} & \boldsymbol{R}_{g2} & \frac{\boldsymbol{O}_{g4}}{\theta\Delta t_n}+\boldsymbol{K}_{og}
\end{bmatrix}\cdot\begin{Bmatrix}\boldsymbol{T}_{i1}\\ \boldsymbol{T}_{i2}\\ \boldsymbol{T}_{o1}\\ \boldsymbol{T}_{o2}\\ \boldsymbol{T}_{g1}\\ \boldsymbol{T}_{g2}\\ \boldsymbol{T}_{g3}\\ \boldsymbol{T}_{g4}\end{Bmatrix}^{n+1}$$

$$= \begin{bmatrix}
\frac{\boldsymbol{O}_i}{\Delta t_n} & 0 & 0 & 0 & 0 & 0 & 0 & 0\\
0 & \frac{\boldsymbol{O}_i}{\Delta t_n} & 0 & 0 & 0 & 0 & 0 & 0\\
0 & 0 & \frac{\boldsymbol{O}_o}{\Delta t_n} & 0 & 0 & 0 & 0 & 0\\
0 & 0 & 0 & \frac{\boldsymbol{O}_o}{\Delta t_n} & 0 & 0 & 0 & 0\\
0 & 0 & 0 & 0 & \frac{\boldsymbol{O}_{g1}}{\Delta t_n} & 0 & 0 & 0\\
0 & 0 & 0 & 0 & 0 & \frac{\boldsymbol{O}_{g2}}{\Delta t_n} & 0 & 0\\
0 & 0 & 0 & 0 & 0 & 0 & \frac{\boldsymbol{O}_{g3}}{\Delta t_n} & 0\\
0 & 0 & 0 & 0 & 0 & 0 & 0 & \frac{\boldsymbol{O}_{g4}}{\Delta t_n}
\end{bmatrix}\cdot\left[\frac{1}{\theta\Delta t_n}\begin{Bmatrix}\boldsymbol{T}_{i1}\\ \boldsymbol{T}_{i2}\\ \boldsymbol{T}_{o1}\\ \boldsymbol{T}_{o2}\\ \boldsymbol{T}_{g1}\\ \boldsymbol{T}_{g2}\\ \boldsymbol{T}_{g3}\\ \boldsymbol{T}_{g4}\end{Bmatrix}^{n}+\left(\frac{1}{\theta}-1\right)\begin{Bmatrix}\dot{\boldsymbol{T}}_{i1}\\ \dot{\boldsymbol{T}}_{i2}\\ \dot{\boldsymbol{T}}_{o1}\\ \dot{\boldsymbol{T}}_{o2}\\ \dot{\boldsymbol{T}}_{g1}\\ \dot{\boldsymbol{T}}_{g2}\\ \dot{\boldsymbol{T}}_{g3}\\ \dot{\boldsymbol{T}}_{g4}\end{Bmatrix}^{n}\right]+\begin{Bmatrix}\boldsymbol{F}_{i1}\\ \boldsymbol{F}_{i2}\\ \boldsymbol{F}_{o1}\\ \boldsymbol{F}_{o2}\\ \boldsymbol{F}_{g1}\\ \boldsymbol{F}_{g2}\\ \boldsymbol{F}_{g3}\\ \boldsymbol{F}_{g4}\end{Bmatrix}^{n+1}-\begin{Bmatrix}0\\ 0\\ 0\\ 0\\ \boldsymbol{R}_s\cdot\boldsymbol{T}_s\\ \boldsymbol{R}_s\cdot\boldsymbol{T}_s\\ \boldsymbol{R}_s\cdot\boldsymbol{T}_s\\ \boldsymbol{R}_s\cdot\boldsymbol{T}_s\end{Bmatrix}^{n+1} \tag{1-105b}$$

with $\theta \in (\frac{1}{2}, 1)$ for the TR and BE scheme, respec- tively.

with a first-order accuracy and the semi-implicit non-dissipative trapezoid rule (TR) one yields from (1-100)

1.9 Analytical Solution of the Local Problem

1.9.1 Local steady-state condition with given temperature at borehole wall

The present analytical solution is only valid for local steady-state heat transport and given temperature $T_s = T_s(z,t)$ at borehole wall. It was firstly derived by Eskilson and Claesson[12] for heat transfer between two pipes and the borehole wall. We extend the analytical method to CXA, CXC, 1U and 2U configurations of BHE. The local steady-state heat balance equations for fluid in pipe-in and pipe-out read

$$\begin{aligned} -A^i \rho^r c^r u(\nabla_z T_{i1}) &= \frac{T_{i1}-T_s}{R_1^\Delta} + \frac{T_{i1}-T_{o1}}{R_{12}^\Delta} \\ A^i \rho^r c^r u(\nabla_z T_{o1}) &= \frac{T_{o1}-T_s}{R_2^\Delta} + \frac{T_{o1}-T_{i1}}{R_{12}^\Delta} \end{aligned} \qquad (1\text{-}106)$$

which have to be solved for the pipe(s)-in temperature $T_{i1}(z)$ and pipe(s)-out temperature $T_{o1}(z)$. In (1-106) the vertical heat conductivity in the pipes is neglected. It is further assumed that the inner cross-sectional area of pipe-in and pipe-out is equal $A^i = A_i^i = A_o^i$. The local steady-state condition limits the application of (1-106) to a time scale larger than[12]

$$t > t_{\text{limit}}^{\text{steady}} = \frac{5}{4} D^2 \left(\frac{\varepsilon \rho^f c^f + (1-\varepsilon)\rho^s c^s}{\varepsilon \lambda^f + (1-\varepsilon)\lambda^s} \right) \qquad (1\text{-}107)$$

The time for the refrigerant to circulate through the borehole is $2A^i\bar{L}/Q_r$. Accordingly, equations (1-106) can only describe transient input variations of inlet temperature and pumping rate on a time scale larger than[12]

$$t > t_{\text{limit}}^{\text{steady}} + A^i \frac{2\bar{L}}{Q_r} \qquad (1\text{-}108)$$

The specific thermal flux $\varphi(z,t)$ exchanging heat of the borehole with the adjacent soil s is given from (1-106) according to

$$\varphi(z,t) = \frac{T_s - T_{i1}}{R_1^\Delta} + \frac{T_s - T_{o1}}{R_2^\Delta} \qquad (1\text{-}109)$$

1.9.2 Eskilson and Claesson's analytical BHE solution

The coupled equations (1-106) can be solved by using Laplace transforms[12]. It yields

$$\begin{aligned} T_{i1}(z,t) &= T_{i1}(0,t) f_1(z) + T_{o1}(0,t) f_2(z) + \int_0^z T_s(\xi,t) f_4(z-\xi) d\xi \\ T_{o1}(z,t) &= -T_{i1}(0,t) f_2(z) + T_{o1}(0,t) f_3(z) - \int_0^z T_s(\xi,t) f_5(z-\xi) d\xi \end{aligned} \qquad (0 \le z \le \bar{L}) \qquad (1\text{-}110)$$

The functions $f_1, f_2, \ldots, f_5$ are given by the expressions

$$\left.\begin{aligned} f_1(z) &= e^{\beta z}[\cosh(\gamma z) - \delta\sinh(\gamma z)] \\ f_2(z) &= e^{\beta z}\frac{\beta_{12}}{\gamma}\sinh(\gamma z) \\ f_3(z) &= e^{\beta z}[\cosh(\gamma z) + \delta\sinh(\gamma z)] \\ f_4(z) &= e^{\beta z}\left[\beta_1\cosh(\gamma z) - \left(\delta\beta_1 + \frac{\beta_2\beta_{12}}{\gamma}\right)\sinh(\gamma z)\right] \\ f_5(z) &= e^{\beta z}\left[\beta_2\cosh(\gamma z) + \left(\delta\beta_2 + \frac{\beta_1\beta_{12}}{\gamma}\right)\sinh(\gamma z)\right] \end{aligned}\right\} \tag{1-111}$$

where

$$\beta_1 = \frac{1}{R_1^{\Delta} A^i \rho^r c^r u} \qquad \beta_2 = \frac{1}{R_2^{\Delta} A^i \rho^r c^r u} \qquad \beta_{12} = \frac{1}{R_{12}^{\Delta} A^i \rho^r c^r u} \qquad \beta = \frac{\beta_2 - \beta_1}{2}$$
$$\gamma = \sqrt{\frac{(\beta_1 + \beta_2)^2}{4} + \beta_{12}(\beta_1 + \beta_2)} \qquad \delta = \frac{1}{\gamma}\left(\beta_{12} + \frac{\beta_1 + \beta_2}{2}\right) \tag{1-112}$$

The following boundary conditions are applied

$$\begin{aligned} T_{i1}(0, t) &= T_i(t) \\ T_{i1}(\bar{L}, t) &= T_{o1}(\bar{L}, t) \end{aligned} \tag{1-113}$$

where $T_i(t)$ represents the inlet temperature. Using (1-113) in (1-111) and (1-112) the outlet temperature $T_o(t)$ is given as

$$T_o(t) = T_{o1}(0, t) \tag{1-114}$$

1.9.3 Solution for 1U and 2U configurations

It is assumed that the pipes are arranged symmetrically within the borehole. Accordingly, there is

$$R_2^{\Delta} = R_1^{\Delta} \tag{1-115}$$

so that

$$\left.\begin{aligned}\beta_2 &= \beta_1 = \frac{1}{R_1^{\Delta} A^i \rho^r c^r u}\\ \beta_{12} &= \frac{1}{R_{12}^{\Delta} A^i \rho^r c^r u}\\ \beta &= 0\\ \gamma &= \sqrt{\beta_1^2 + 2\beta_{12}\beta_1}\\ \delta &= \frac{1}{\gamma}(\beta_{12} + \beta_1)\end{aligned}\right\} \qquad (1\text{-}116)$$

Hence, (1-111) simplifies

$$\left.\begin{aligned}f_1(z) &= \cosh(\gamma z) - \delta\sinh(\gamma z)\\ f_2(z) &= \frac{\beta_{12}}{\gamma}\sinh(\gamma z)\\ f_3(z) &= \cosh(\gamma z) + \delta\sinh(\gamma z)\\ f_4(z) &= \beta_1\cosh(\gamma z) - \left(\delta\beta_1 + \frac{\beta_2\beta_{12}}{\gamma}\right)\sinh(\gamma z)\\ f_5(z) &= \beta_2\cosh(\gamma z) + \left(\delta\beta_2 + \frac{\beta_1\beta_{12}}{\gamma}\right)\sinh(\gamma z)\end{aligned}\right\} \qquad (1\text{-}117)$$

In using (1-113) the equations (1-110) can be equalized at $z = \bar{L}$ and solved for the outlet temperature $T_o(t)$, *viz.*,

$$T_o(t) = T_i(t)\frac{f_1(\bar{L}) + f_2(\bar{L})}{f_3(\bar{L}) - f_2(\bar{L})} + \int_0^{\bar{L}} \frac{T_s(\xi, t)[f_4(\bar{L} - \xi) + f_5(\bar{L} - \xi)]}{f_3(\bar{L}) - f_2(\bar{L})} d\xi \qquad (1\text{-}118)$$

With known inlet temperature $T_i(t)$ from the boundary condition (1-113) and outlet temperature T_o from (1-118) the temperature distributions T_{i1} and T_{o1} as a function of z and t are obtained after evaluating the integrals in (1-110). It yields[1)]

$$\begin{aligned}T_{i1}(z, t) &= T_i(t)f_1(z) + T_o(t)f_2(z) + \int_0^z T_s(\xi, t)f_4(z - \xi)d\xi\\ T_{o1}(z, t) &= -T_i(t)f_2(z) + T_o(t)f_3(z) - \int_0^z T_s(\xi, t)f_5(z - \xi)d\xi\end{aligned} \qquad (1\text{-}119)$$

The integrals in (1-119) are performed elementwise, where the solid temperature T_s at the borehole wall is numerically approximated as a linear function from the nodal finite element solution at time *t*. For example

$$\begin{aligned}&\int_0^z T_s(\xi, t)f_4(z - \xi)d\xi \qquad (1\text{-}120)\\ &\approx \sum_{e \in (z_1^e, z_2^e) \le z} \frac{T_s^e(z_1^e, t) + T_s^e(z_2^e, t)}{2} F_4(z, z_2^e, z_1^e)\end{aligned}$$

where z_1^e, z_2^e represent the vertical coordinates of the lower and upper nodes, respectively, of element *e*.

[1)] The integrals of functions $f_4(z - \xi)$ and $f_5(z - \xi)$ result for 1U and 2U configurations

$$F_4(z, a, b) = \int_a^b f_4(z - \xi)d\xi = -\frac{\beta_1}{\gamma}\sinh(\gamma(z - \xi))\Big|_a^b + \left(\frac{\delta\beta_1}{\gamma} + \frac{\beta_2\beta_{12}}{\gamma^2}\right)\cosh(\gamma(z - \xi))\Big|_a^b$$

$$F_5(z, a, b) = \int_a^b f_5(z - \xi)d\xi = -\frac{\beta_2}{\gamma}\sinh(\gamma(z - \xi))\Big|_a^b - \left(\frac{\delta\beta_2}{\gamma} + \frac{\beta_1\beta_{12}}{\gamma^2}\right)\cosh(\gamma(z - \xi))\Big|_a^b$$

The temperature distribution for the grout zones figuration $T_{g1}(z,t)$ and $T_{g2}(z,t)$ can be derived for the 1U con-

$$T_{g1}(z,t) = \frac{\left[\frac{T_s(z,t)}{R_{gs}^{1U}} + \frac{T_{o1}(z,t)}{R_{fig}^{1U}} + \left(\frac{T_s(z,t)}{R_{gs}^{1U}} + \frac{T_{i1}(z,t)}{R_{fig}^{1U}}\right) u_1 R_{gg}^{1U}\right] R_{gg}^{1U}}{(R_{gg}^{1U})^2 u_1^2 - 1}$$

$$T_{g2}(z,t) = \left(\frac{T_{g1}(z,t)}{R_{gg}^{1U}} + \frac{T_{o1}(z,t)}{R_{fig}^{1U}} + \frac{T_s(z,t)}{R_{gs}^{1U}}\right)\frac{1}{u_1} \tag{1-121}$$

with

$$u_1 = \frac{1}{R_{fig}^{1U}} + \frac{1}{R_{gs}^{1U}} + \frac{1}{R_{gg}^{1U}} \tag{1-122}$$

The grout distributions for 2U configurations give

$$T_{g1}(z,t) = T_{g2}(z,t) = \frac{\left[\frac{2T_s(z,t)}{R_{gs}^{2U}} + \frac{2T_{o1}(z,t)}{R_{fig}^{2U}} + \left(\frac{2T_s(z,t)}{R_{gs}^{2U}} + \frac{2T_{i1}(z,t)}{R_{fig}^{2U}}\right) u_2 v\right] v}{v^2 u_2^2 - 1}$$

$$T_{g3}(z,t) = T_{g4}(z,t) = \left(\frac{T_{g1}(z,t)}{v} + \frac{2T_{o1}(z,t)}{R_{fig}^{2U}} + \frac{2T_s(z,t)}{R_{gs}^{2U}}\right)\frac{1}{u_2} \tag{1-123}$$

with

$$u_2 = \frac{2}{R_{fig}^{2U}} + \frac{2}{R_{gs}^{2U}} + \frac{1}{v}$$

$$v = \frac{R_{gg1}^{2U} R_{gg2}^{2U}}{2(R_{gg1}^{2U} + R_{gg2}^{2U})} \tag{1-124}$$

$$\left.\begin{aligned} R_1^{\Delta} &= R_{fig}^{1U} + R_{gs}^{1U} \\ R_{12}^{\Delta} &= \frac{(u_1 R_{fig}^{1U} R_{gg}^{1U})^2 - (R_{fig}^{1U})^2}{R_{gg}^{1U}} \end{aligned}\right\} \quad \text{for 1U pipes} \tag{1-125}$$

The thermal resistances R_1^{Δ} and R_{12}^{Δ} are given by

$$\left.\begin{aligned} R_1^{\Delta} &= \frac{R_{fig}^{2U} + R_{gs}^{2U}}{2} \\ R_{12}^{\Delta} &= \frac{(R_{fig}^{2U})^2}{4}\left(u_2^2 v - \frac{1}{v}\right) \end{aligned}\right\} \quad \text{for 2U pipes} \qquad (1\text{-}126)$$

1.9.4 Solution for CXA configuration

For coaxial BHE pipes with annular inlet there is

$$R_2^{\Delta} = \infty \qquad (1\text{-}127)$$

so that

$$\left.\begin{aligned} \beta_1 &= \frac{1}{R_1^{\Delta} A^i \rho^r c^r u} \\ \beta_2 &= 0 \\ \beta_{12} &= \frac{1}{R_{12}^{\Delta} A^i \rho^r c^r u} \\ \beta &= -\frac{\beta_1}{2} \\ \gamma &= \sqrt{\frac{\beta_1^2}{4} + \beta_{12}\beta_1} \\ \delta &= \frac{1}{\gamma}\left(\beta_{12} + \frac{\beta_1}{2}\right) \end{aligned}\right\} \qquad (1\text{-}128)$$

Hence, (1-111) simplifies

$$\left.\begin{aligned} f_1(z) &= e^{\beta z}[\cosh(\gamma z) - \delta\sinh(\gamma z)] \\ f_2(z) &= e^{\beta z}\frac{\beta_{12}}{\gamma}\sinh(\gamma z) \\ f_3(z) &= e^{\beta z}[\cosh(\gamma z) + \delta\sinh(\gamma z)] \\ f_4(z) &= e^{\beta z}[\beta_1\cosh(\gamma z) - \delta\beta_1\sinh(\gamma z)] \\ f_5(z) &= e^{\beta z}\frac{\beta_1\beta_{12}}{\gamma}\sinh(\gamma z) \end{aligned}\right\} \qquad (1\text{-}129)$$

The outlet temperature $T_o(t)$ is determined by

$$T_o(t) = T_i(t)\frac{f_1(\bar{L}) + f_2(\bar{L})}{f_3(\bar{L}) - f_2(\bar{L})} + \int_0^{\bar{L}} T_s(\xi, t)\frac{[f_4(\bar{L} - \xi) + f_5(\bar{L} - \xi)]}{f_3(\bar{L}) - f_2(\bar{L})} d\xi \qquad (1\text{-}130)$$

and the temperature distributions $T_{i1}(z, t)$ and $T_{o1}(z, t)$ are obtained from the integral expressions[2)]

$$\begin{aligned} T_{i1}(z, t) &= T_i(t)f_1(z) + T_o(t)f_2(z) + \int_0^z T_s(\xi, t)f_4(z - \xi)d\xi \\ T_{o1}(z, t) &= -T_i(t)f_2(z) + T_o(t)f_3(z) - \int_0^z T_s(\xi, t)f_5(z - \xi)d\xi \end{aligned} \qquad (1\text{-}131)$$

[2)] The integrals of functions $f_4(z-\xi)$ and $f_5(z-\xi)$ result for the CXA configuration

$$F_4(z, a, b) = \int_a^b f_4(z - \xi)d\xi = \frac{\beta_1}{\gamma^2 - \beta^2}\exp(\beta(z - \xi))\Big|_a^b \left[(\gamma\delta + \beta)\cosh(\gamma(z - \xi))\Big|_a^b - (\gamma + \delta\beta)\sinh(\gamma(z - \xi))\Big|_a^b\right]$$

$$F_5(z, a, b) = \int_a^b f_5(z - \xi)d\xi = \frac{\beta_1\beta_{12}}{\gamma^2 - \beta^2}\exp(\beta(z - \xi))\Big|_a^b \left[\frac{\beta}{\gamma}\sinh(\gamma(z - \xi))\Big|_a^b - \cosh(\gamma(z - \xi))\Big|_a^b\right]$$

The temperature distribution for the grout zone $T_{g1}(z,t)$ yields

$$T_{g1}(z,t) = \frac{R_{fig}^{CXA}}{R_{fig}^{CXA}+R_{gs}^{CXA}}[T_s(z,t) - T_{i1}(z,t)] + T_{i1}(z,t) \tag{1-132}$$

The thermal resistances R_1^Δ and R_{12}^Δ are given by

$$\begin{aligned} R_1^\Delta &= R_{fig}^{CXA} + R_{gs}^{CXA} \\ R_{12}^\Delta &= R_{ff}^{CXA} \end{aligned} \tag{1-133}$$

1.9.5 Solution for CXC configuration

For coaxial BHE pipes with centred inlet there is

$$R_1^\Delta = \infty \tag{1-134}$$

so that

$$\left.\begin{aligned} \beta_1 &= 0 \\ \beta_2 &= \frac{1}{R_2^\Delta A^i \rho^r c^r u} \\ \beta_{12} &= \frac{1}{R_{12}^\Delta A^i \rho^r c^r u} \\ \beta &= \frac{\beta_2}{2} \\ \gamma &= \sqrt{\frac{\beta_1^2}{4}+\beta_{12}\beta_2} \\ \delta &= \frac{1}{\gamma}\left(\beta_{12}+\frac{\beta_2}{2}\right) \end{aligned}\right\} \tag{1-135}$$

Hence, (1-111) simplifies

$$\left.\begin{aligned} f_1(z) &= e^{\beta z}[\cosh(\gamma z) - \delta\sinh(\gamma z)] \\ f_2(z) &= e^{\beta z}\frac{\beta_{12}}{\gamma}\sinh(\gamma z) \\ f_3(z) &= e^{\beta z}[\cosh(\gamma z) + \delta\sinh(\gamma z)] \\ f_4(z) &= -e^{\beta z}\frac{\beta_2\beta_{12}}{\gamma}\sinh(\gamma z) \\ f_5(z) &= e^{\beta z}[\beta_2\cosh(\gamma z) + \delta\beta_2\sinh(\gamma z)] \end{aligned}\right\} \tag{1-136}$$

The outlet temperature $T_o(t)$ is determined by

$$T_o(t) = T_i(t)\frac{f_1(\bar{L})+f_2(\bar{L})}{f_3(\bar{L})-f_2(\bar{L})} + \int_0^{\bar{L}} \frac{T_s(\xi,t)[f_4(\bar{L}-\xi)+f_5(\bar{L}-\xi)]}{f_3(\bar{L})-f_2(\bar{L})} d\xi \tag{1-137}$$

and the temperature distributions $T_{i1}(z, t)$ and $T_{o1}(z, t)$ are obtained from the integral expressions[3)]

$$T_{i1}(z, t) = T_i(t)f_1(z) + T_o(t)f_2(z) + \int_0^z T_s(\xi, t)f_4(z-\xi)d\xi$$
$$T_{o1}(z, t) = -T_i(t)f_2(z) + T_o(t)f_3(z) - \int_0^z T_s(\xi, t)f_5(z-\xi)d\xi \quad (1\text{-}138)$$

The temperature distribution for the grout zone $T_{g1}(z, t)$ yields

$$T_{g1}(z, t) = \frac{R_{fig}^{CXC}}{R_{fig}^{CXC} + R_{gs}^{CXC}}[T_s(z, t) - T_{o1}(z, t)] + T_{o1}(z, t) \quad (1\text{-}139)$$

The thermal resistances R_1^{Δ} and R_{12}^{Δ} are given by

$$R_1^{\Delta} = R_{fig}^{CXC} + R_{gs}^{CXC}$$
$$R_{12}^{\Delta} = R_{ff}^{CXC} \quad (1\text{-}140)$$

1.10 Implementation

1.10.1 Numerical BHE solution

The aquifer system is discretized in FEFLOW by 3D prismatic finite elements, where the BHE systems are modeled by vertical boreholes. Each borehole is discretized by a number of *K* nodes, which are linked to the 1D pipe elements as exemplified in Fig. 1.6 for a 2U exchanger borehole. The *K* nodes represent inner boundary nodes of the soil *s*. The Cauchy-type BC (1-9) requires the solution of the grout temperatures $T_{gi}(i = 1, \ldots, G)$ at the *K* nodes, which is obtained by solving the local matrix system consisting of *K**DOF equations (DOF = 8 for 2U DOF = 4 for 1U and DOF = 3 for CXA and CXC), *cf.* Appendix B.

For the soil temperatures $\boldsymbol{T}_s^{n+1} = \boldsymbol{T}_s(t^{n+1})$ the spatio-temporal finite element discretization leads to a matrix system of the following form:

$$[\boldsymbol{A}_s] \cdot \{\boldsymbol{T}_s\}^{n+1} = \{\boldsymbol{B}_s\}^{n+1} - \sum_{i=1}^{G} [\boldsymbol{R}_s] \cdot \{\boldsymbol{T}_{gi}\}^{n+1} \quad (1\text{-}141)$$

with

$$[\boldsymbol{A}_s] = [\boldsymbol{A}_s^*] - G[\boldsymbol{R}_s] \quad (1\text{-}142)$$

[3)] The integrals of functions $f_4(z-\xi)$ and $f_5(z-\xi)$ result for the CXC configuration

$$F_4(z, a, b) = \int_a^b f_4(z-\xi)d\xi = \frac{\beta_2\beta_{12}}{\beta^2-\gamma^2}\exp(\beta(z-\xi))\Big|_a^b \left[\frac{\beta}{\gamma}\sinh(\gamma(z-\xi))\Big|_a^b - \cosh(\gamma(z-\xi))\Big|_a^b\right]$$

$$F_5(z, a, b) = \int_a^b f_5(z-\xi)d\xi = \frac{\beta_2}{\gamma^2-\beta^2}\exp(\beta(z-\xi))\Big|_a^b \left[(\beta-\gamma\delta)\cosh(\gamma(z-\xi))\Big|_a^b + (\delta\beta-\gamma)\sinh(\gamma(z-\xi))\Big|_a^b\right]$$

where $[A_s^*]$ is the soil matrix without the soil-grout transfer condition. Denoting by N the number of soil s nodes, the matrix has the space $[A_s] \in \Re^{N \times N}$. In (1-141) the grout temperatures $T_{gi}(i = 1, \ldots, G)$ on the RHS results from the heat transfer boundary condition (1-9), which is unknown at first. The overall matrix equation system can be written as

$$\begin{bmatrix} A_{i1} & 0 & R_{io} & 0 & R_i & 0 & 0 & 0 \\ 0 & A_{i2} & 0 & 0 & 0 & R_i & 0 & 0 \\ R_{io} & 0 & A_{o1} & 0 & 0 & 0 & R_o & 0 \\ 0 & 0 & 0 & A_{o2} & 0 & 0 & 0 & R_o \\ R_i & 0 & 0 & 0 & A_{ig} & R_{g2} & R_{g1} & R_{g1} \\ 0 & R_i & 0 & 0 & R_{g2} & A_{ig} & R_{g1} & R_{g1} \\ 0 & 0 & R_o & 0 & R_{g1} & R_{g1} & A_{og} & R_{g2} \\ 0 & 0 & 0 & R_o & R_{g1} & R_{g1} & R_{g2} & A_{og} \end{bmatrix} \cdot \begin{Bmatrix} T_{i1} \\ T_{i2} \\ T_{o1} \\ T_{o2} \\ T_{g1} \\ T_{g2} \\ T_{g3} \\ T_{g4} \end{Bmatrix}^{n+1} = \begin{Bmatrix} B_{i1} \\ B_{i2} \\ B_{o1} \\ B_{o2} \\ B_{g1} - R_s \cdot T_s \\ B_{g2} - R_s \cdot T_s \\ B_{g3} - R_s \cdot T_s \\ B_{g4} - R_s \cdot T_s \end{Bmatrix}^{n+1} \tag{1-143}$$

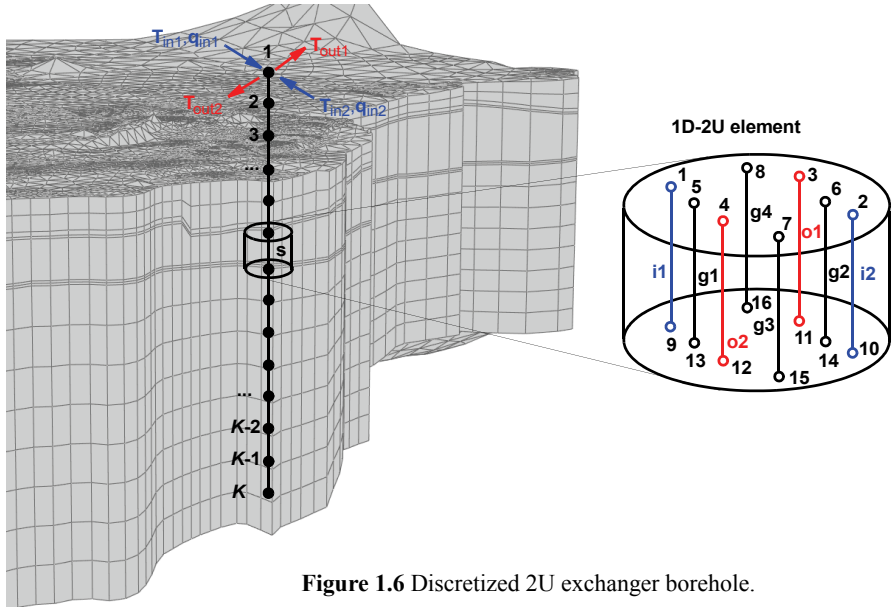

Figure 1.6 Discretized 2U exchanger borehole.

Both matrix systems (1-141) and can be combined

$$\left[\begin{array}{cccccccc:c} \boldsymbol{A}_{i1} & 0 & \boldsymbol{R}_{io} & 0 & \boldsymbol{R}_{i} & 0 & 0 & 0 & 0 \\ 0 & \boldsymbol{A}_{i2} & 0 & 0 & 0 & \boldsymbol{R}_{i} & 0 & 0 & 0 \\ \boldsymbol{R}_{io} & 0 & \boldsymbol{A}_{o1} & 0 & 0 & 0 & \boldsymbol{R}_{o} & 0 & 0 \\ 0 & 0 & 0 & \boldsymbol{A}_{o2} & 0 & 0 & 0 & \boldsymbol{R}_{o} & 0 \\ \boldsymbol{R}_{i} & 0 & 0 & 0 & \boldsymbol{A}_{ig} & \boldsymbol{R}_{g2} & \boldsymbol{R}_{g1} & \boldsymbol{R}_{g1} & \boldsymbol{R}_{s} \\ 0 & \boldsymbol{R}_{i} & 0 & 0 & \boldsymbol{R}_{g2} & \boldsymbol{A}_{ig} & \boldsymbol{R}_{g1} & \boldsymbol{R}_{g1} & \boldsymbol{R}_{s} \\ 0 & 0 & \boldsymbol{R}_{o} & 0 & \boldsymbol{R}_{g1} & \boldsymbol{R}_{g1} & \boldsymbol{A}_{og} & \boldsymbol{R}_{g2} & \boldsymbol{R}_{s} \\ 0 & 0 & 0 & \boldsymbol{R}_{o} & \boldsymbol{R}_{g1} & \boldsymbol{R}_{g1} & \boldsymbol{R}_{g2} & \boldsymbol{A}_{og} & \boldsymbol{R}_{s} \\ \hdashline 0 & 0 & 0 & 0 & \boldsymbol{R}_{s} & \boldsymbol{R}_{s} & \boldsymbol{R}_{s} & \boldsymbol{R}_{s} & \boldsymbol{A}_{s} \end{array}\right] \cdot \left\{\begin{array}{c} \boldsymbol{T}_{i1} \\ \boldsymbol{T}_{i2} \\ \boldsymbol{T}_{o1} \\ \boldsymbol{T}_{o2} \\ \boldsymbol{T}_{g1} \\ \boldsymbol{T}_{g2} \\ \boldsymbol{T}_{g3} \\ \boldsymbol{T}_{g4} \\ \hdashline \boldsymbol{T}_{s} \end{array}\right\}^{n+1} = \left\{\begin{array}{c} \boldsymbol{B}_{i1} \\ \boldsymbol{B}_{i2} \\ \boldsymbol{B}_{o1} \\ \boldsymbol{B}_{o2} \\ \boldsymbol{B}_{g1} \\ \boldsymbol{B}_{g2} \\ \boldsymbol{B}_{g3} \\ \boldsymbol{B}_{g4} \\ \hdashline \boldsymbol{B}_{s} \end{array}\right\}^{n+1} \tag{1-144}$$

and expressed in a compact form

$$\left[\begin{array}{cc} \boldsymbol{A}_{\text{pipe}} & \boldsymbol{R}_{ps} \\ \boldsymbol{R}_{ps}^{T} & \boldsymbol{A}_{s} \end{array}\right] \cdot \left\{\begin{array}{c} \boldsymbol{T}_{\text{pipe}} \\ \hdashline \boldsymbol{T}_{s} \end{array}\right\}^{n+1} = \left\{\begin{array}{c} \boldsymbol{B}_{\text{pipe}} \\ \hdashline \boldsymbol{B}_{s} \end{array}\right\}^{n+1} \tag{1-145}$$

where

$$
\boldsymbol{A}_{\text{pipe}_{(\text{K*DOF}\times\text{K*DOF})}} = \begin{bmatrix}
\boldsymbol{A}_{i1} & 0 & \boldsymbol{R}_{io} & 0 & \boldsymbol{R}_i & 0 & 0 & 0 \\
0 & \boldsymbol{A}_{i2} & 0 & 0 & 0 & \boldsymbol{R}_i & 0 & 0 \\
\boldsymbol{R}_{io} & 0 & \boldsymbol{A}_{o1} & 0 & 0 & 0 & \boldsymbol{R}_o & 0 \\
0 & 0 & 0 & \boldsymbol{A}_{o2} & 0 & 0 & 0 & \boldsymbol{R}_o \\
\boldsymbol{R}_i & 0 & 0 & 0 & \boldsymbol{A}_{ig} & \boldsymbol{R}_{g2} & \boldsymbol{R}_{g1} & \boldsymbol{R}_{g1} \\
0 & \boldsymbol{R}_i & 0 & 0 & \boldsymbol{R}_{g2} & \boldsymbol{A}_{ig} & \boldsymbol{R}_{g1} & \boldsymbol{R}_{g1} \\
0 & 0 & \boldsymbol{R}_o & 0 & \boldsymbol{R}_{g1} & \boldsymbol{R}_{g1} & \boldsymbol{A}_{og} & \boldsymbol{R}_{g2} \\
0 & 0 & 0 & \boldsymbol{R}_o & \boldsymbol{R}_{g1} & \boldsymbol{R}_{g1} & \boldsymbol{R}_{g2} & \boldsymbol{A}_{og}
\end{bmatrix}
$$

$$
\boldsymbol{T}^{n+1}_{\text{pipe}_{(\text{K*DOF})}} = \begin{Bmatrix}
\boldsymbol{T}_{i1} \\ \boldsymbol{T}_{i2} \\ \boldsymbol{T}_{o1} \\ \boldsymbol{T}_{o2} \\ \boldsymbol{T}_{g1} \\ \boldsymbol{T}_{g2} \\ \boldsymbol{T}_{g3} \\ \boldsymbol{T}_{g4}
\end{Bmatrix}^{n+1}
$$

$$
\boldsymbol{R}_{ps_{(\text{K*DOF}\times 1)}} = \begin{bmatrix}
0 \\ 0 \\ 0 \\ 0 \\ \boldsymbol{R}_s \\ \boldsymbol{R}_s \\ \boldsymbol{R}_s \\ \boldsymbol{R}_s
\end{bmatrix}
$$

$$
\boldsymbol{R}^T_{ps_{(1\times\text{K*DOF})}} = \begin{bmatrix} 0 & 0 & 0 & 0 & \boldsymbol{R}_s & \boldsymbol{R}_s & \boldsymbol{R}_s & \boldsymbol{R}_s \end{bmatrix}
$$

$$
\boldsymbol{A}_{s_{(N\times N)}} \in \Re^{N\times N} \tag{1-146}
$$

For the solution of the complete equation system (1-145) a *static condensation* strategy (also known as sub-structuring technique[22] frequently used in finite-element structural engineering) is preferred, where the internal pipe variables $\boldsymbol{T}^{n+1}_{\text{pipe}}$ can be eliminated from (1-145). The first row of the matrix system (1-145) reads

$$
\boldsymbol{A}_{\text{pipe}} \cdot \boldsymbol{T}^{n+1}_{\text{pipe}} + \boldsymbol{R}_{ps} \cdot \boldsymbol{T}^{n+1}_{s} = \boldsymbol{B}^{n+1}_{\text{pipe}} \tag{1-147}
$$

It yields

$$
\boldsymbol{T}^{n+1}_{\text{pipe}} = \boldsymbol{A}^{-1}_{\text{pipe}} \cdot (\boldsymbol{B}^{n+1}_{\text{pipe}} - \boldsymbol{R}_{ps} \cdot \boldsymbol{T}^{n+1}_{s}) \tag{1-148}
$$

Taking the second row of (1-145) the temperature vector of the pipe $\boldsymbol{T}_{\text{pipe}}^{n+1}$ can be eliminated by using (1-148). It finally gives a reduced equation system of the following form

$$[\boldsymbol{A}_s - \boldsymbol{R}_{ps}^T \cdot (\boldsymbol{A}_{\text{pipe}}^{-1} \cdot \boldsymbol{R}_{ps})] \cdot \boldsymbol{T}_s^{n+1} = \boldsymbol{B}_s^{n+1} - \boldsymbol{R}_{ps}^T \cdot (\boldsymbol{A}_{\text{pipe}}^{-1} \cdot \boldsymbol{B}_{\text{pipe}}^{n+1}) \tag{1-149}$$

or

$$\left.\begin{aligned} (\boldsymbol{A}_s - \boldsymbol{A}_{ps}) \cdot \boldsymbol{T}_s^{n+1} &= \boldsymbol{B}_s^{n+1} - \boldsymbol{B}_{ps}^{n+1} \\ \boldsymbol{A}_{ps} &= \boldsymbol{R}_{ps}^T \cdot (\boldsymbol{A}_{\text{pipe}}^{-1} \cdot \boldsymbol{R}_{ps}) \\ \boldsymbol{B}_{ps}^{n+1} &= \boldsymbol{R}_{ps}^T \cdot (\boldsymbol{A}_{\text{pipe}}^{-1} \cdot \boldsymbol{B}_{\text{pipe}}^{n+1}) \end{aligned}\right\} \tag{1-150}$$

for solving only the soil temperature $\boldsymbol{T}_s^{n+1}$ at the new time stage $n+1$, where the modified matrix $(\boldsymbol{A}_s - \boldsymbol{A}_{ps}) = (\boldsymbol{A}_s{}^* - G\boldsymbol{R}_s - \boldsymbol{A}_{ps})$ represents the *Schur complement*[3]. Note that $\boldsymbol{A}_{\text{pipe}}$ is a local $K^*\text{DOF} \times K^*\text{DOF}$ matrix, which is commonly not large $K \ll N$ ($K < 1000$, DOF = 8 for 2U, DOF = 4 for 1U and DOF = 3 for CXA and CXC). Accordingly, the inverse $\boldsymbol{A}_{\text{pipe}}^{-1}$ can be easily computed by a direct Gaussian matrix solution for each pipe. If $\boldsymbol{T}_s^{n+1}$ is solved from (1-149) the internal temperatures $\boldsymbol{T}_{\text{pipe}}^{n+1}$ for each exchanger can be simply recomputed from (1-148).

Using (1-150) and (1-148) a direct and non-sequential solution of complete temperature field for the soil and the pipe, $\boldsymbol{T}_s^{n+1}$, $\boldsymbol{T}_{\text{pipe}}^{n+1}$, appears possible. Basically, there is no need for an iterative solution of the coupled system (1-144), which is superior to the strictly iterative sequential strategy as used by Al-Khoury *et al.*[1,2]. However, the condensed matrix system (1-150) in form of the Schur complement $(\boldsymbol{A}_s - \boldsymbol{A}_{ps})$ has been shown frequently very stiff, particularly when the heat transfer coefficients dominate above thermal conduction and advection of the global system. In such cases numerical roundoff errors can distort the solution and balance errors occur in long-term or steady-state simulations. To prevent these harmful effects the solution of the severely ill-conditioned matrix system (1-150) is combined with an iterative correction strategy as follows:

$$\text{starting solution } \tau = 0: \quad \begin{cases} (\boldsymbol{A}_s - \boldsymbol{A}_{ps}) \cdot \boldsymbol{T}_s^{(n+1),\tau} = \boldsymbol{B}_s^{n+1} - \boldsymbol{B}_{ps}^{n+1} \\ \boldsymbol{T}_{\text{pipe}}^{(n+1),\tau} = \boldsymbol{A}_{\text{pipe}}^{-1} \cdot (\boldsymbol{B}_{\text{pipe}}^{n+1} - \boldsymbol{R}_{ps} \cdot \boldsymbol{T}_s^{(n+1),\tau}) \end{cases}$$

$$\text{iterative correction } \tau + 1: \quad \begin{cases} (\boldsymbol{A}_s{}^* - G\boldsymbol{R}_s) \cdot \boldsymbol{T}_s^{(n+1),(\tau+1)} = \boldsymbol{B}_s^{n+1} - \boldsymbol{R}_{ps}^T \cdot \boldsymbol{T}_{\text{pipe}}^{(n+1),\tau} \\ \boldsymbol{T}_{\text{pipe}}^{(n+1),(\tau+1)} = \boldsymbol{A}_{\text{pipe}}^{-1} \cdot (\boldsymbol{B}_{\text{pipe}}^{n+1} - \boldsymbol{R}_{ps} \cdot \boldsymbol{T}_s^{(n+1),(\tau+1)}) \end{cases} \tag{1-151}$$

were τ corresponds to an iteration counter. At each time level we start with the Schur complement solution. It results the soil temperature $\boldsymbol{T}_s^{(n+1),\tau}$ and the pipe temperature $\boldsymbol{T}_{\text{pipe}}^{(n+1),\tau}$ at initial state $\tau = 0$. With known $\boldsymbol{T}_{\text{pipe}}^{(n+1),\tau}$ the global soil matrix system (second row of matrix system (1-145)) is solved to find the new iterate for temperatures of soil $\boldsymbol{T}_s^{(n+1),(\tau+1)}$ and accordingly of pipe $\boldsymbol{T}_{\text{pipe}}^{(n+1),(\tau+1)}$. The iteration τ in (1-

151) is repeated until a satisfactory convergence is achieved, such as

$$\left\| \boldsymbol{T}_{\text{pipe}}^{(n+1),(\tau+1)} - \boldsymbol{T}_{\text{pipe}}^{(n+1),\tau} \right\|_{L_p} < \delta \tag{1-152}$$

where $\|\ldots\|_{L_p}$ can be used as a RMS ($p = 2$) or maximum ($p = \infty$) error norm[9] and δ is a user-specified dimensionless error tolerance. Usually, only one iteration is required in transient simulations if the time step length Δt_n is chosen appropriately small. This is effectively controlled by using the adaptive time stepping strategy combined with predictor-corrector schemes as described above.

1.10.2 Analytical BHE solution

For the soil temperatures $\boldsymbol{T}_s^{n+1} = \boldsymbol{T}_s(t^{n+1})$ the spatio-temporal finite element discretization is taken in the following form:

$$([\boldsymbol{A}_s^*] + [\boldsymbol{R}_{\text{BHE}}]) \cdot \{\boldsymbol{T}_s\}^{n+1} = \{\boldsymbol{B}_s\}^{n+1} + \{\boldsymbol{B}_{\text{BHE}}(\boldsymbol{T}_s^{n+1})\} \tag{1-153}$$

where with (1-109) a BHE-related diagonal resistance matrix

$$\boldsymbol{R}_{\text{BHE}} = \int_z \left(\frac{1}{R_1^{\Delta}} + \frac{1}{R_2^{\Delta}} \right) dz \boldsymbol{I} \tag{1-154}$$

and a source/sink term on the RHS

$$\boldsymbol{B}_{\text{BHE}}(\boldsymbol{T}_s^{n+1}) = \int_z \left(\frac{\boldsymbol{T}_{i1}^{n+1}}{R_1^{\Delta}} + \frac{\boldsymbol{T}_{o1}^{n+1}}{R_2^{\Delta}} \right) dz \tag{1-155}$$

appear. The temperature distributions for pipe(s)-in $\boldsymbol{T}_{i1}^{n+1}$ and pipe(s)-out $\boldsymbol{T}_{o1}^{n+1}$ represent complex analytical expressions as given in Chapter 1.9 (see equations (1-119), (1-131), (1-138)). Since they are again dependent on the soil temperature

$$\begin{aligned} \boldsymbol{T}_{i1}^{n+1} &= \boldsymbol{T}_{i1}^{n+1}(\boldsymbol{T}_s^{n+1}) \\ \boldsymbol{T}_{o1}^{n+1} &= \boldsymbol{T}_{o1}^{n+1}(\boldsymbol{T}_s^{n+1}) \end{aligned} \tag{1-156}$$

the matrix system (1-153) is solved via an iterative procedure according to

$$\begin{aligned} \text{starting solution } \tau = 0: &\quad ([\boldsymbol{A}_s^*] + \boldsymbol{R}_{\text{BHE}}) \cdot \{\boldsymbol{T}_s\}^{(n+1),\tau} = \{\boldsymbol{B}_s\}^{n+1} + \{\boldsymbol{B}_{\text{BHE}}(\boldsymbol{T}_s^{n})\} \\ \text{iteration } \tau + 1: &\quad ([\boldsymbol{A}_s^*] + \boldsymbol{R}_{\text{BHE}}) \cdot \{\boldsymbol{T}_s\}^{(n+1),(\tau+1)} = \{\boldsymbol{B}_s\}^{n+1} + \{\boldsymbol{B}_{\text{BHE}}(\boldsymbol{T}_s^{(n+1),\tau})\} \end{aligned} \tag{1-157}$$

The iterations with the current time level $(n+1)$ are stopped if

$$\left\| \boldsymbol{T}_s^{(n+1),(\tau+1)} - \boldsymbol{T}_s^{(n+1),\tau} \right\|_{L_p} < \delta \tag{1-158}$$

1.11 Important Note on Meshing BHE Nodes

In using the numerical (Al-Khoury *et al.*'s[1,2]) or the analytical (Eskilson and Claesson's[12]) solution strategies a BHE is reduced to an internal boundary condition occupied at a single node in a horizontal view on the 3D finite element mesh of the global problem. It appears similar to a well node, where a pumping well with a rate Q_b in the borehole is modeled at a singular node via a well function applied to the sink/source term Q of (1-1):

$$Q = Q_b(\boldsymbol{x}_i)\delta(\boldsymbol{x}-\boldsymbol{x}_i) \tag{1-159}$$

where $\delta(\ )$ is the Dirac delta function and $\boldsymbol{x}_i$ are the well coordinates of the well node i.

Such types of nodal singularities in a mesh require specific considerations due to the following reasons. If inserting Q_b at a singular node i the resulting head value h_i in a flow simulation don't usually represent the head exactly at the physical borehole radius r_b; instead, the actually computed head h_i at the node i is to be deemed on a different radius, which is called *virtual radius* r_{virtual}; in regional models often larger than the real physical radius r_b. It can be shown that the virtual radius r_{virtual} is primarily dependent on the mesh discretization around the node i, represented by a nodal distance Δ (*cf.* Fig. 1.7). Accordingly, it has to be the goal in present modeling to design the mesh around those singular well nodes i in such a way that the virtual radius r_{virtual} meets at best the physical radius r_b of the well. In doing this, we introduce the following two methods for tuning the mesh at BHE nodes.

1.11.1 Direct estimation of nodal distance Δ (method 1)

It follows the ideas by Nillert[15] developed for 2D horizontal regular meshes applied to wells in groundwater flow. Extending to conductive heat transport we find the following relationships, which are similar to potential flow. In a spatial discretization the conductive heat flux H_i at the singular node i can be expressed by

$$H_i = \vartheta\Phi(T_\Delta - T_{\text{virtual}}) \tag{1-160}$$

where T_Δ is the temperature at the distance Δ, T_{virtual} is the temperature at the virtual radius r_{virtual}, which must not be the physical BHE radius r_b, Φ is the heat transfer coefficient and ϑ is a shape factor determined by the BHE-node surrounding mesh. For regular 2D meshes Nillert[15] derived:

$$\vartheta = n\tan\left(\frac{\pi}{n}\right) \tag{1-161}$$

where $n = (4, 5, 6, \ldots)$ denotes the number of surrounding nodes, where $n = 6$ is typical for triangular horizontal meshes (see Fig. 1.7).

In contrast to the approximate solution (1-160), for a radially symmetric BHE we find the analytical (heat) well formula[6]

$$H_i^{\text{ana}} = 2\pi\Phi\frac{T_\Delta - T_{\text{virtual}}}{\ln\left(\frac{\Delta}{r_{\text{virtual}}}\right)} \tag{1-162}$$

Equating (1-162) and (1-160) it yields

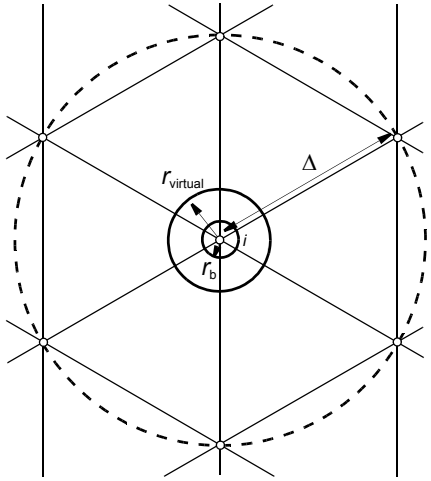

Figure 1.7 Spatial discretization ($n = 6$) around a BHE 'well' node.

$$\Delta = \exp(\alpha)\, r_{virtual} \qquad \alpha = \frac{2\pi}{n \tan\left(\frac{\pi}{n}\right)} \tag{1-163}$$

Equation (1-163) can be used to determine the required nodal distance Δ spacing from the BHE node if forcing the virtual radius to the borehole radius $r_{virtual} = r_b$. It obtains for typical horizontal meshes

$$\Delta = a\, r_b \qquad a = \begin{cases} 4.81 & \text{for } n = 4 \\ 6.13 & \text{for } n = 6 \\ 6.66 & \text{for } n = 8 \end{cases} \tag{1-164}$$

Relation (1-164) represents an direct and effective estimation for an *optimal mesh* refinement around a BHE node. It will be shown further below that those meshes which are designed by using criterion (1-164) can give optimal accuracy, even better than spatial discretizations over-refined $\Delta \le r_b$ or coarse $\Delta > a\, r_b$ around BHE nodes.

1.11.2 Iterative determination of nodal distance Δ (method 2)

While method 1 is derived for ideal regular meshes, this method 2 is applicable on the actual discretization. It has been proposed by Bauer[4] in using the following iterative procedure for finding optimal nodal distances Δ around BHE nodes. Using Kelvin's line source theory[14] the temperature change ΔT in a distance from the line source is given by

$$\Delta T = \frac{Q_h}{2\pi\lambda^s} \int_{\beta}^{\infty} \frac{e^{-\beta^2}}{\beta} d\beta \qquad \beta = \frac{r}{2\sqrt{\alpha t}} \qquad \alpha = \frac{\lambda^s}{\rho^s c^s} \tag{1-165}$$

where Q_h is the thermal power of the line source and r represents the radial distance from the line source. For the case $\alpha t / r^2 > 1$ an approximate solution of (1-165) is given[20] (applied to SI units of parameters)

$$\Delta T = \frac{0.1833 Q_h}{\lambda^s} \left[\log_{10}\left(\frac{\alpha t}{r^2}\right) + 0.106 \frac{r^2}{\alpha t} + 0.351 \right] \tag{1-166}$$

The relation (1-166) can be used to determine an optimal nodal (horizontal) distance Δ via the following iterative procedure. The computations should be simply realized on a 2D horizontal mesh, where the full 3D problem is reduced to only one layer:

(1) Apply a standard thermal 4th kind boundary condition (no BHE) at the node i with an injection rate of 50 W/m.
(2) Simulate the problem for t = 50 days at given mesh having an initial 'averaged' nodal distance Δ. For a first guess of Δ the relation (1-164) can be used. It is to be required that the outer boundaries of the global problem are not affected by the injecting heat over the considered time (outer boundaries are suitably distant the 'well' node i).
(3) Determine ΔT from the (forward) numerical solution of the reduced 2D problem at the 'well' node i.
(4) Determine r from the implicit expression (1-166) with given ΔT, Q_h, λ^s, α and t.
(5) If $r < r_b$ then the adjacent nodes around the BHE have to shifted outwards, so Δ increases. Otherwise, if $r > r_b$ then the adjacent nodes have to be moved inwards, so Δ decreases.
(6) Repeat the simulation over 50 days (re-initialize the solution meantime) and compare with (1-166) again. Terminate the iterative loop if it meets $r \approx r_b$.

Both methods are beneficial to determine optimal mesh geometry for BHE in the regional discretization. Optimal conditions commonly exist when the nodal distance Δ around the BHE node is larger than the actual BHE radius r_b because we know from (1-164) that Δ should be chosen five to six times larger than the physical borehole radius r_b, which is in general a reasonable guess. We note that if refining the mesh too much around the BHE node, so $\Delta < r_b$, the solution can become even poorer, unless the contrast for the thermal conductivity of elements within the physical borehole radius r_b is significantly increased.

The advantage of method 2 against method 1 is that the forward solution (step 3) is based on the actual horizontal spatial discretization and accordingly ΔT in (1-166) implies the accuracy from the overall horizontal discretization, not only related to the local spacing conditions around the BHE. On the other hand, the effort in the iterative procedure of method 2 can be high, particularly if applied to arrays of BHE, and method 1 could be sufficient under practical conditions. We note finally, both methods assume that the heat transfer process is dominated by a radial conduction having no (or negligible) variation in the vertical direction.

1.12 Related FEFLOW Dialogs

1.12.1 BHE well specification

1.12.1.1 BHE 'well' option

A BHE represents a specific 'well' boundary condition of 4th kind in heat transport similar to a multi-well boundary condition (BC) of 4th kind in flow problems. However, the BHE 'well' boundary condition is more complex and requires various additional data. Particularly, 4th kind well boundary condition has to be changed from the standard single well node input to the BHE node input by using the *Heat 4th Kind BC Option Options Menu* as exhibited in Fig. 1.8.

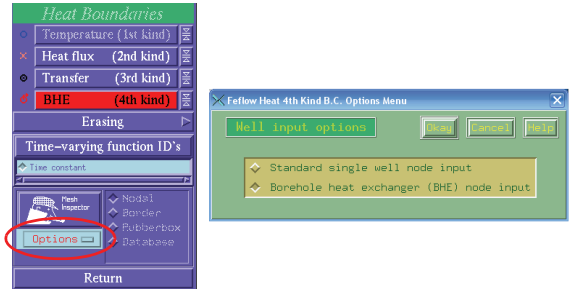

Figure 1.8 Setting borehole heat exchanger node input via FEFLOW's heat 4th kind BC option menu.

1.12.1.2 BHE setting

A single BHE or a series of BHE can be set at nodes on top slice of a 3D heat (or thermohaline) transport model. If such a node is assigned the *Borehole Heat Exchanger Setting Menu* immediately appears (see Fig. 1.9), where a number of data can be specified:

- Total heat input rate Q_h [J d^{-1}] of BHE. Note that Q_h implies an inlet temperature T_i [^{o}C] (see further below).
- Exact coordinates (x_p, y_p, z_p) [m] of BHE on top slice.
- Pipe bottom and pipe top locations ('screen lengths') of BHE.
- Computational method applied to BHE: *analytical* (Eskilson and Claesson's[12]) method or *numerical* (Al-Khoury *et al.*'s[1,2]) method.
- Type of BHE: double U-shape (2U), single U-shape (1U) and coaxial shapes (CXA and CXC).
- Dataset identifier, where an arbitrary number of dataset can be introduced, i.e., series of BHE can be assigned in a 3D model, where different BHE types and parameters mutually occur.
- Dataset parameters related to an identifier for <u>*Borehole*</u> consisting of (1) borehole diameter D [m], (2) pipe distance w [m], for <u>*Pipe-in*</u> consisting of (3) pipe-in outer diameter $d_i^o = 2r_{i1}^o = 2r_{i2}^o$ [m], (4) pipe-in wall thickness $b_i = r_{i1}^o - r_{i1}^i = r_{i2}^o - r_{i2}^i$ [m], (5) pipe-in thermal conductivity $\lambda_{i1}^p = \lambda_{i2}^p$ [Jm^{-1}s^{-1}K^{-1}], for <u>*Pipe-out*</u> consisting of (6) pipe-out outer diameter $d_o^o = 2r_{o1}^o = 2r_{o2}^o$ [m], (7) pipe-out wall thickness $b_o = r_{o1}^o - r_{o1}^i = r_{o2}^o - r_{o2}^i$ [m], (8) pipe-out thermal conductivity $\lambda_{o1}^p = \lambda_{o2}^p$ [Jm^{-1}s^{-1}K^{-1}], for <u>*Refrigerant*</u> consisting of (9) flow discharge (total) Q_r [m^{3}d^{-1}], which can also be a time-dependent function $Q_r = Q_r(t)$ if assigning a power function via the ID's menu as shown in Fig. 1.9, (10) volumetric heat capacity $\rho^r c^r$ [10^6 Jm^{-3}K^{-1}], (11) thermal conductivity λ^r [Jm^{-1}s^{-1}K^{-1}], (12) dynamic viscosity μ^r [10^{-3} kg m^{-1}s^{-1}], (13) mass density ρ^r [10^3 kg m^{-3}], for <u>*Grout*</u> consisting of (14) volumetric heat capacity $\rho^g c^g$ [10^6 Jm^{-3}K^{-1}], and (15) thermal conductivity λ^g [Jm^{-1}s^{-1}K^{-1}].
- <u>*Heat transfer*</u> coefficients or <u>*thermal resistances*</u> in dependence on the selected computational method (either numerical or analytical), which can be alternatively *computed* from the dataset parameters (1) to (15) according to the analytical formulae as given in Chapter 1.6 or *prescribed* in an independent manner. In the prescribed mode it is to be directly input (16) heat transfer and thermal resistance of pipe-in to grout Φ_{fig} [Jm^{-2}s^{-1}K^{-1}], R_{fig} [msKJ^{-1}], respectively, for 2U and 1U or heat transfer and thermal resistance of pipe-in to pipe-out Φ_{ff}^{CXC} [Jm^{-2}s^{-1}K^{-1}], R_{ff}^{CXC} [msKJ^{-1}], respectively, for CXC, (17) heat transfer and thermal resistance of pipe-out to grout Φ_{fog} [Jm^{-2}s^{-1}K^{-1}], R_{fog} [msKJ^{-1}], respectively, for 2U and 1U or heat transfer and thermal resistance of pipe-out to pipe-in Φ_{ff}^{CXA} [Jm^{-2}s^{-1}K^{-1}], R_{ff}^{CXA} [msKJ^{-1}], respectively, for CXA, (18) heat transfer and thermal resistance of grout to grout Φ_{gg1}^{2U} [Jm^{-2}s^{-1}K^{-1}], R_{gg1}^{2U} [msKJ^{-1}], respectively, for 2U or Φ_{gg}^{1U} [J m^{-2}s^{-1}K^{-1}], R_{gg}^{1U} [msKJ^{-1}], respectively, for 1U, (19) heat transfer and thermal resistance of grout to grout Φ_{gg2}^{2U} [Jm^{-2}s^{-1}K^{-1}], R_{gg2}^{2U} [msKJ^{-1}], respectively, only for 2U, and (20) heat transfer and thermal resistance of grout to soil Φ_{gs} [Jm^{-2}s^{-1}K^{-1}], R_{gs} [m KJ^{-1}], respectively.

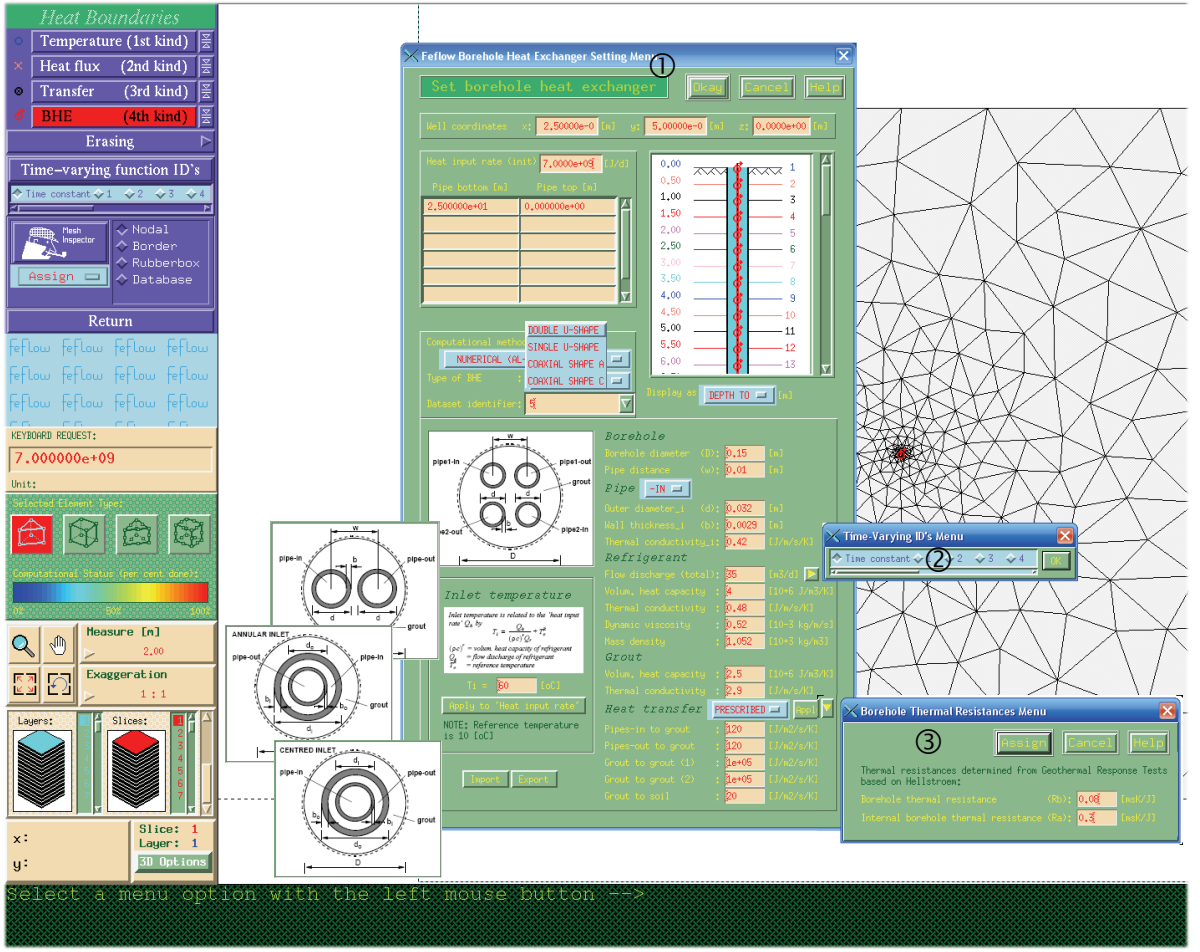

Figure 1.9 FEFLOW's borehole heat exchanger setting menu: ① major BHE menu, ② optional input for time-dependent discharge $Q_r(t)$ of refrigerant, and ③ optional input of thermal resistances R_b and R_a from thermal response tests.

The prescribed input mode for heat transfer coefficients and thermal resistances can be advantageous in cases, where the user prefers to specify these coefficients by applying own rules or experimental findings. This can be input for each coefficient. Alternatively, if the *borehole thermal resistances* R_b and R_a are known from thermal response tests (see Chapter 1.7) a specific dialog supports the assignment of the heat transfer coefficients and thermal resistances in the prescribed input mode as depicted in Fig. 1.9. Furthermore, in the BHE setting menu there are *import* and *export* buttons (see Fig. 1.9) to exchange BHE data in a XML file format.

1.12.1.3 BHE inlet temperature

Giving the total heat input rate Q_h, the total flow discharge Q_r and the volumetric heat capacity $\rho^r c^r$ of refrigerant for a BHE the difference between inlet temperature T_i [°C] and reference temperature T_o^R [°C] is determined as

$$T_i - T_o^R = \frac{Q_h}{\rho^r c^r Q_r} \tag{1-167}$$

which provides the Dirichlet-type (1st kind) boundary condition for the temperature at pipe(s)-in on top slice z_p, i.e.,

$$T_{i1}(x_p, y_p, z_p, t) = T_{i2}(x_p, y_p, z_p, t) = T_i \qquad t > 0 \tag{1-168}$$

if the reference temperature T_o^R is given. In the BHE setting menu (Fig. 1.9) the inlet temperature T_i can be explicitly specified provided that steady-state rate conditions (Q_h and Q_r) occur, which updates the heat input rate Q_h according to relationship (1-167) at given Q_r, $\rho^r c^r$ and T_o^R. Furthermore, changing Q_h, Q_r or $\rho^r c^r$ the inlet temperature T_i is modified.

1.12.2 BHE computational results

If simulation for a 3D heat (or thermohaline) transport problem with incorporated BHE systems is started a number of additional diagram windows appears in which the computational results for each BHE are displayed. There are the following windows (Fig. 1.10):

- Vertical temperature profiles ① for each BHE are plotted. It covers the pipe-in, pipe-out and grout temperature profiles at simulation time t^n, i.e., $T_{i1}(x_p, y_p, z, t^n)$, $T_{o1}(x_p, y_p, z, t^n)$, $T_g(x_p, y_p, z, t^n)$ for $\forall z$.
- The 'average heat' diagram window ② is used to display the time history of pipe-out temperature on top, i.e., $T_{o1}(x_p, y_p, z_p, t)$ for $\forall t$.
- The different BHE representations in a model are identified automatically by an alpha-numeric or numeric ID starting with 'a','b', ..., '_27','_28', ... In this context a selection dialog ③ is available (Fig. 1.10) to switch between the IDs of BHE.
- The iteration progress according to (1-151) or (1-157) is watched in a specific window ④. It displays the iteration history τ and outlines when the iterative procedure converges or eventually fails. In combination with adaptive time stepping the iterations τ are performed within each time step Δt_n. It can happen that the iteration diverges, however, the time step error control rejects the current solution $\boldsymbol{T}^{n+1}$ and restarts with a reduced time step.

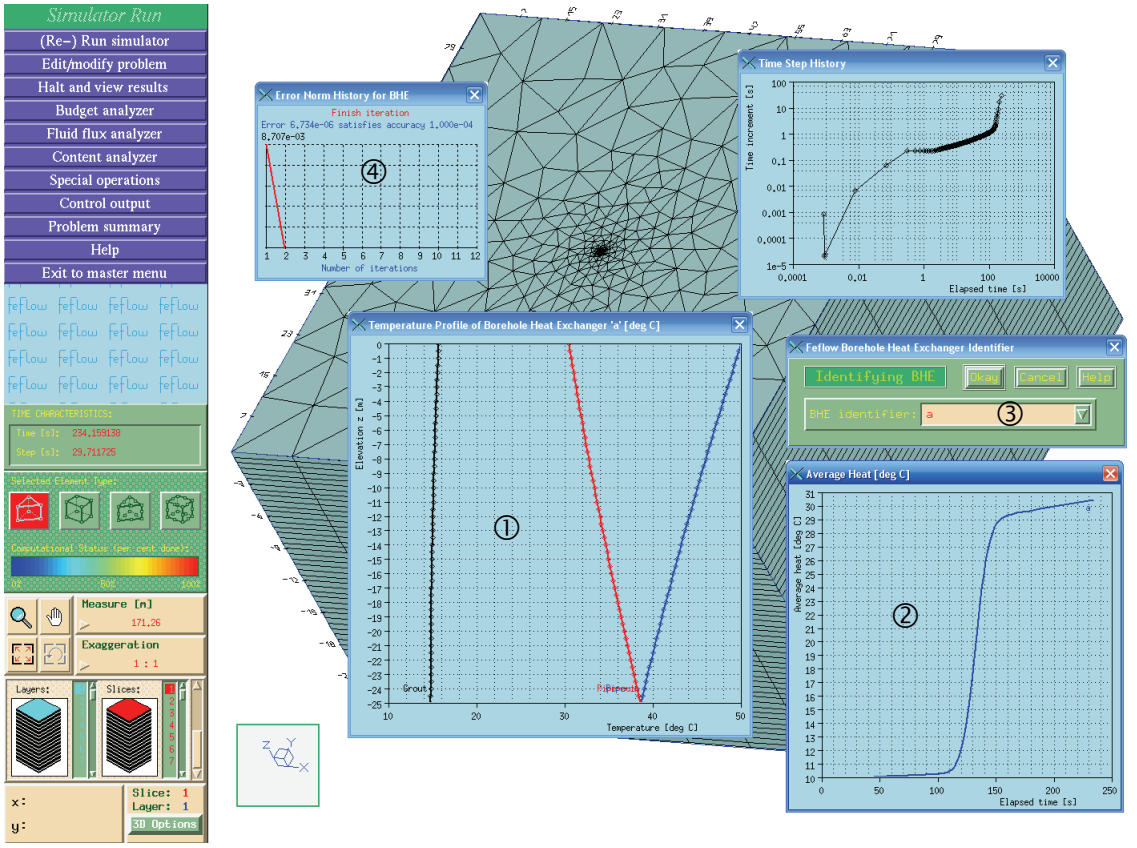

Figure 1.10 BHE diagrams appearing in simulation: ① vertical temperature profiles, ② time history of pipe-out temperature on top $T_{o1}(x_p, y_p, z_p, t)$, ③ BHE's ID selector and ④ iteration history.

1.13 Model Validation

1.13.1 Numerical versus analytical solutions of BHE for steady-state conditions and given temperature at borehole wall

We directly compare the numerical and analytical solution strategies by Al-Khoury *et al.*[1,2] and Eskilson

and Claesson[12] for local BHE problems under steady-state conditions. The analytical BHE solutions are compared to the numerical BHE results for CXA, CXC, 1U and 2U-type BHE configurations with the parameters as listed in Tab. 1.1 to 1.4, respectively. Since T_s is here specified as a boundary condition the solid properties become irrelevant for the present comparison analysis. The heat transfer coefficients and thermal resistances as summarized in Tab. 1.1 to 1.4 are computed from the formula given in Chapter 1.6 and 1.5, respectively.

Table 1.1 Parameters of CXA-type BHE used for analytical comparisons

Parameter	Symbol	Value	Unit
Depth of borehole	$\bar{L}$	100	m
Borehole diameter	D	10	cm
Outer diameter of pipe-in	d_{i1}^{o}	5	cm
Outer diameter of pipe-out	d_{o1}^{o}	2.4	cm
Pipe-in wall thickness	b_{i1}	4	mm
Pipe-out wall thickness	b_{o1}	3	mm
Thermal conductivities of pipe walls	$\lambda_{i1}^{p}, \lambda_{o1}^{p}$	0.38	$\mathrm{J\,m^{-1}s^{-1}K^{-1}}$
Boundary solid temperature	T_s	10	$^{o}\mathrm{C}$
Reference temperature	T_o^R	10	$^{o}\mathrm{C}$
Inlet temperature	T_i	80	$^{o}\mathrm{C}$
Total flow discharge of refrigerant	Q_r	21.86	$\mathrm{m^3 d^{-1}}$
Total heat input rate	Q_h	$6.3216 \cdot 10^{9}$	$\mathrm{J\,d^{-1}}$
Volumetric heat capacity of refrigerant	$\rho^r c^r$	$4.1312 \cdot 10^{6}$	$\mathrm{J\,m^{-3}K^{-1}}$
Thermal conductivity of refrigerant	λ^r	0.6405	$\mathrm{J\,m^{-1}s^{-1}K^{-1}}$
Dynamic viscosity of refrigerant	μ^r	$0.54741 \cdot 10^{-3}$	$\mathrm{kg\,m^{-1}s^{-1}}$
Mass density of refrigerant	ρ^r	$0.9881 \cdot 10^{3}$	$\mathrm{kg\,m^{-3}}$
Volumetric heat capacity of grout	$\rho^g c^g$	$2.19 \cdot 10^{6}$	$\mathrm{J\,m^{-3}K^{-1}}$

Table 1.1 Parameters of CXA-type BHE used for analytical comparisons (cont.)

Parameter	Symbol	Value	Unit
Thermal conductivity of grout	λ^g	2.3	$J\ m^{-1}\ s^{-1}\ K^{-1}$
Computed heat transfer coefficients:			
pipe-in to grout	Φ_{fig}	69.698	$[J\ m^{-2}\ s^{-1}\ K^{-1}]$
pipe-in to pipe-out	Φ_{ff}	135.64	$[J\ m^{-2}\ s^{-1}\ K^{-1}]$
grout to soil	Φ_{gs}	195.74	$[J\ m^{-2}\ s^{-1}\ K^{-1}]$
Computed thermal resistances:			
pipe-in to grout	R_{fig}	0.10874	$[m\ s\ K\ J^{-1}]$
pipe-in to pipe-out	R_{ff}	0.13037	$[m\ s\ K\ J^{-1}]$
grout to soil	R_{gs}	0.01626	$[m\ s\ K\ J^{-1}]$

Table 1.2 Parameters of CXC-type BHE used for analytical comparisons

Parameter	Symbol	Value	Unit
Depth of borehole	$\bar{L}$	100	m
Borehole diameter	D	10	cm
Outer diameter of pipe-in	d^o_{i1}	2.4	cm
Outer diameter of pipe-out	d^o_{o1}	5	cm
Pipe-in wall thickness	b_{i1}	3	mm
Pipe-out wall thickness	b_{o1}	4	mm
Thermal conductivities of pipe walls	$\lambda^p_{i1}, \lambda^p_{o1}$	0.38	$J\ m^{-1}\ s^{-1}\ K^{-1}$
Boundary solid temperature	T_s	10	^oC
Reference temperature	T^R_o	10	^oC
Inlet temperature	T_i	80	^oC
Total flow discharge of refrigerant	Q_r	21.86	$m^3\ d^{-1}$

Table 1.2 Parameters of CXC-type BHE used for analytical comparisons (cont.)

Parameter	Symbol	Value	Unit
Total heat input rate	Q_h	$6.3216 \cdot 10^9$	$J\ d^{-1}$
Volumetric heat capacity of refrigerant	$\rho^r c^r$	$4.1312 \cdot 10^6$	$J\ m^{-3}K^{-1}$
Thermal conductivity of refrigerant	λ^r	0.6405	$J\ m^{-1}s^{-1}K^{-1}$
Dynamic viscosity of refrigerant	μ^r	$0.54741 \cdot 10^{-3}$	$kg\ m^{-1}s^{-1}$
Mass density of refrigerant	ρ^r	$0.9881 \cdot 10^3$	$kg\ m^{-3}$
Volumetric heat capacity of grout	$\rho^g c^g$	$2.19 \cdot 10^6$	$J\ m^{-3}K^{-1}$
Thermal conductivity of grout	λ^g	2.3	$J\ m^{-1}s^{-1}K^{-1}$
Computed heat transfer coefficients: pipe-out to grout pipe-out to pipe-in grout to soil	 Φ_{fog} Φ_{ff} Φ_{gs}	 69.698 135.64 195.74	 $[J\ m^{-2}s^{-1}K^{-1}]$ $[J\ m^{-2}s^{-1}K^{-1}]$ $[J\ m^{-2}s^{-1}K^{-1}]$
Computed thermal resistances: pipe-out to grout pipe-out to pipe-in grout to soil	 R_{fog} R_{ff} R_{gs}	 0.10874 0.13037 0.01626	 $[m\ s\ K\ J^{-1}]$ $[m\ s\ K\ J^{-1}]$ $[m\ s\ K\ J^{-1}]$

Table 1.3 Parameters of 1U-type BHE used for analytical comparisons

Parameter	Symbol	Value	Unit
Depth of borehole	$\bar{L}$	100	m
Borehole diameter	D	13	cm
Pipe distance	w	6	cm
Outer diameter of pipe-in	d^o_{i1}	3.2	cm
Outer diameter of pipe-out	d^o_{o1}	3.2	cm

Table 1.3 Parameters of 1U-type BHE used for analytical comparisons (cont.)

Parameter	Symbol	Value	Unit
Pipe-in wall thickness	b_{i1}	2.9	mm
Pipe-out wall thickness	b_{o1}	2.9	mm
Thermal conductivities of pipe walls	$\lambda^p_{i1}, \lambda^p_{o1}$	0.38	$J\,m^{-1}s^{-1}K^{-1}$
Boundary solid temperature	T_s	10	°C
Reference temperature	T^R_o	10	°C
Inlet temperature	T_i	80	°C
Total flow discharge of refrigerant	Q_r	21.86	$m^3 d^{-1}$
Total heat input rate	Q_h	$6.3216 \cdot 10^9$	$J\,d^{-1}$
Volumetric heat capacity of refrigerant	$\rho^r c^r$	$4.1312 \cdot 10^6$	$J\,m^{-3}K^{-1}$
Thermal conductivity of refrigerant	λ^r	0.6405	$J\,m^{-1}s^{-1}K^{-1}$
Dynamic viscosity of refrigerant	μ^r	$0.54741 \cdot 10^{-3}$	$kg\,m^{-1}s^{-1}$
Mass density of refrigerant	ρ^r	$0.9881 \cdot 10^3$	$kg\,m^{-3}$
Volumetric heat capacity of grout	$\rho^g c^g$	$2.19 \cdot 10^6$	$J\,m^{-3}K^{-1}$
Thermal conductivity of grout	λ^g	2.3	$J\,m^{-1}s^{-1}K^{-1}$
Computed heat transfer coefficients:			
pipe-in to grout	Φ_{fig}	77.993	$[J\,m^{-2}s^{-1}K^{-1}]$
pipe-out to grout	Φ_{fog}	77.993	$[J\,m^{-2}s^{-1}K^{-1}]$
grout to grout	Φ_{gg}	66.796	$[J\,m^{-2}s^{-1}K^{-1}]$
grout to soil	Φ_{gs}	190.24	$[J\,m^{-2}s^{-1}K^{-1}]$
Computed thermal resistances:			
pipe-in to grout	R_{fig}	0.15577	$[m\,s\,K\,J^{-1}]$
pipe-out to grout	R_{fog}	0.15577	$[m\,s\,K\,J^{-1}]$
grout to grout	R_{gg}	0.11516	$[m\,s\,K\,J^{-1}]$
grout to soil	R_{gs}	0.02574	$[m\,s\,K\,J^{-1}]$

Table 1.4 Parameters of 2U-type BHE used for analytical comparisons

Parameter	Symbol	Value	Unit
Depth of borehole	$\bar{L}$	100	m
Borehole diameter	D	13	cm
Pipe distance	w	4.242	cm
Outer diameter of pipe-in	d_{i1}^{o}	3.2	cm
Outer diameter of pipe-out	d_{o1}^{o}	3.2	cm
Pipe-in wall thickness	b_{i1}	2.9	mm
Pipe-out wall thickness	b_{o1}	2.9	mm
Thermal conductivities of pipe walls	$\lambda_{i1}^{p}, \lambda_{o1}^{p}$	0.38	$\mathrm{J\,m^{-1}s^{-1}K^{-1}}$
Boundary solid temperature	T_s	10	$^{o}\mathrm{C}$
Reference temperature	T_o^R	10	$^{o}\mathrm{C}$
Inlet temperature	T_i	80	$^{o}\mathrm{C}$
Total flow discharge of refrigerant	Q_r	21.86	$\mathrm{m^3 d^{-1}}$
Total heat input rate	Q_h	$6.3216 \cdot 10^{9}$	$\mathrm{J\,d^{-1}}$
Volumetric heat capacity of refrigerant	$\rho^r c^r$	$4.1312 \cdot 10^{6}$	$\mathrm{J\,m^{-3}K^{-1}}$
Thermal conductivity of refrigerant	λ^r	0.6405	$\mathrm{J\,m^{-1}s^{-1}K^{-1}}$
Dynamic viscosity of refrigerant	μ^r	$0.54741 \cdot 10^{-3}$	$\mathrm{kg\,m^{-1}s^{-1}}$
Mass density of refrigerant	ρ^r	$0.9881 \cdot 10^{3}$	$\mathrm{kg\,m^{-3}}$
Volumetric heat capacity of grout	$\rho^g c^g$	$2.19 \cdot 10^{6}$	$\mathrm{J\,m^{-3}K^{-1}}$
Thermal conductivity of grout	λ^g	2.3	$\mathrm{J\,m^{-1}s^{-1}K^{-1}}$

Table 1.4 Parameters of 2U-type BHE used for analytical comparisons (cont.)

Parameter	Symbol	Value	Unit
Computed heat transfer coefficients:			
pipe-in to grout	Φ_{fig}	83.877	$[J\ m^{-2}s^{-1}K^{-1}]$
pipe-out to grout	Φ_{fog}	83.877	$[J\ m^{-2}s^{-1}K^{-1}]$
grout to grout 1	Φ_{gg1}	48489	$[J\ m^{-2}s^{-1}K^{-1}]$
grout to grout 2	Φ_{gg2}	65.323	$[J\ m^{-2}s^{-1}K^{-1}]$
grout to soil	Φ_{gs}	143.32	$[J\ m^{-2}s^{-1}K^{-1}]$
Computed thermal resistances:			
pipe-in to grout	R_{fig}	0.14485	$[m\ s\ K\ J^{-1}]$
pipe-out to grout	R_{fog}	0.14485	$[m\ s\ K\ J^{-1}]$
grout to grout 1	R_{gg1}	0.00031	$[m\ s\ K\ J^{-1}]$
grout to grout 2	R_{gg2}	0.11776	$[m\ s\ K\ J^{-1}]$
grout to soil	R_{gs}	0.06833	$[m\ s\ K\ J^{-1}]$

In the simulation models only the inner borehole is discretized, where boundary conditions for the solid temperature T_s are prescribed at the BHE node patch as exhibited in Fig. 1.11. For the vertical discretization 100 layers are used, i.e., $\Delta z = 1$ m.

The numerical results versus the analytical solutions in form of steady-state vertical temperature profiles of pipe(s)-in, pipe(s)-out and grout zone(s) are shown in Figs. 1.12 to 1.15 for each of the CXA, CXC, 1U and 2U-type BHE configuration, respectively. As evidenced in all cases the agreement is nearly perfect.

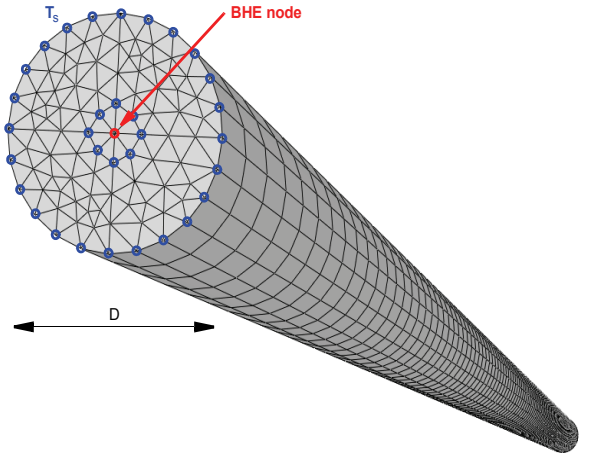

Figure 1.11 Discretized inner borehole with temperature boundary conditions of solid T_s (indicated on top slice).

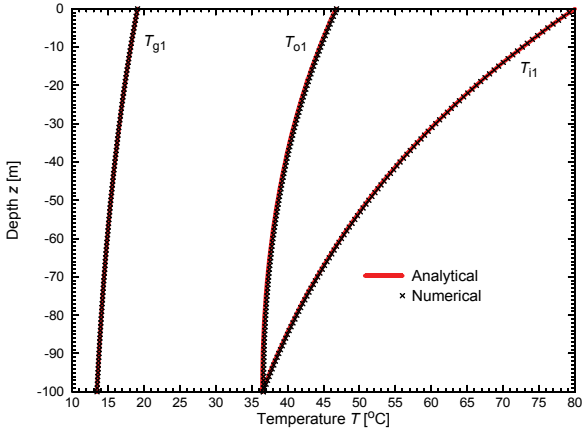

Figure 1.12 Analytical vs. numerical temperature distribution for CXA-type BHE.

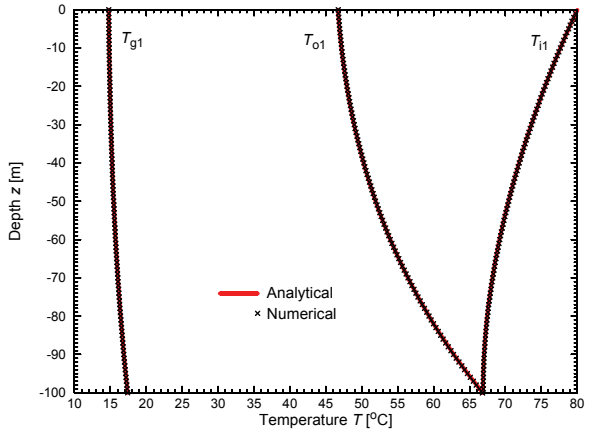

Figure 1.13 Analytical vs. numerical temperature distribution for CXC-type BHE.

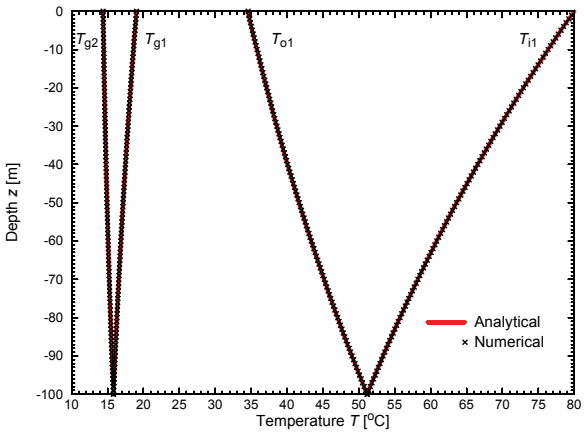

Figure 1.14 Analytical vs. numerical temperature distribution for 1U-type BHE.

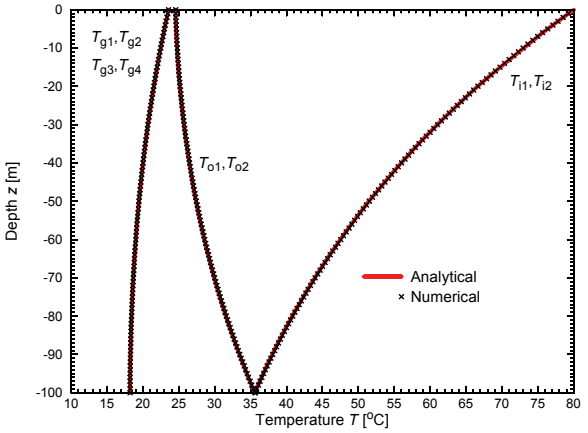

Figure 1.15 Analytical vs. numerical temperature distribution for 2U-type BHE.

1.13.2 Analytical solution of heat transport in a single pipe with soil interaction

There are analytical solutions suited for the partial problem of the 1D transient heat transport in a single pipe with a lateral heat exchange to the surrounding grout or soil. It can be used to compare the numerical results for a BHE solution at a starting period when the heat flow develops in the 1D pipe-in of a heat exchanger interacting with the soil. It is assumed that the heat transfer to the grout and to the soil are equal. In such a case the governing heat transport equation reads

$$\frac{\partial T}{\partial t} + u\frac{\partial T}{\partial z} - D\frac{\partial^2 T}{\partial z^2} + \phi(T - T_s) = 0 \qquad (1\text{-}169)$$

where $T\ (= T_{i1})$ is the fluid temperature in the pipe-in, u is the refrigerant fluid velocity, D is the thermal diffusivity, ϕ is a specific heat transfer coefficient, T_s is the surrounding soil temperature taken as a reference temperature and z is the vertical coordinate. Thermodispersivity, refrigerant fluid velocity and specific heat transfer coefficient are related to the parameters used in the numerical modeling as follows:

$$\begin{aligned} D &= \frac{|\Lambda^r|}{\rho^r c^r} \\ u &= \frac{Q_r}{A^i_{i1}} \qquad A^i_{i1} = \pi(r^i_{i1})^2 \\ \phi &= \frac{2\pi r^o_{i1}\Phi_{fig}}{A^i_{i1}\rho^r c^r} \end{aligned} \qquad (1\text{-}170)$$

Choosing the following initial and boundary conditions according to

$$\begin{aligned} T(z, 0) &= T_s \\ T(0, t) &= T_i \\ \frac{\partial T}{\partial z}(\infty, t) &= 0 \end{aligned} \qquad (1\text{-}171)$$

the analytical solution[19] for (1-169) is given by

$$\begin{aligned} T(z,t) &= T_s + \frac{(T_i - T_s)}{2}\left\{\exp\left[\frac{(u-v)z}{2D}\right]\operatorname{erfc}\left(\frac{z - vt}{2\sqrt{Dt}}\right) + \exp\left[\frac{(u+v)z}{2D}\right]\operatorname{erfc}\left(\frac{z + vt}{2\sqrt{Dt}}\right)\right\} \\ v &= u\sqrt{1 + \frac{4\phi D}{u^2}} \end{aligned} \qquad (1\text{-}172)$$

The comparison between the numerical and analytical solution is performed with the following data

$$
\left.
\begin{aligned}
Q_h &= 2.89086 \cdot 10^6 \ [\mathrm{J\,d^{-1}}] \\
Q_r &= 0.0175 \ [\mathrm{m^3 d^{-1}}] \\
r_{i1}^{i} &= 0.0131 \ [\mathrm{m}] \\
r_{i1}^{o} &= 0.016 \ [\mathrm{m}] \qquad (b = 0.0029 \ [\mathrm{m}]\,) \\
\rho^r c^r &= 4.1298 \cdot 10^6 [\mathrm{J\,m^{-3} K^{-1}}] \\
|\Lambda^r| &= \lambda^r = 0.65 \ [\mathrm{J\,m^{-1} s^{-1} K^{-1}}] \qquad (\alpha_L = 0) \\
\Phi_{fig} &= 12.0 \ [\mathrm{J\,m^{-2} s^{-1} K^{-1}}] \qquad \Phi_{gs} = \Phi_{fig} \qquad \Phi_{fog} = 0 \\
T_s &= T_o^R = 10 \ [^\circ\mathrm{C}] \\
T_i &= \frac{Q_h}{\rho^r c^r Q_r} + T_o^R = 50 \ [^\circ\mathrm{C}]
\end{aligned}
\right\} \quad (1\text{-}173)
$$

For this example the refrigerant discharge and the heat input rate are chosen relatively low in relation to the heat transfer. This has been done to emphasize the heat transfer effect at early times for a pipe with a short length. The numerical model is shown in Fig. 1.16 forming a 3D box with a horizontal extent of 20 m x 20 m and a depth of 1 m. In the central position a single BHE is located, where the heat transfer coefficients of pipe-in to grout and grout to soil are identical $\Phi_{fig} = \Phi_{gs}$, while the heat transfer of the pipe-out is set to zero $\Phi_{fog} = 0$ to eliminate thermal interaction of the pipe-out to the grout heated by pipe-in.

The computed temperature BHE profiles in comparison to the analytical solution at $t = 0.02$ days are shown in Fig. 1.17 revealing a good agreement. The simulations have been performed for two different vertical discretizations of 100 and 200 layers. Adaptive time stepping with the AB/TR scheme and an error tolerance of $\delta = 10^{-4}$ have been used. It is combined with a streamline upwind scheme to stabilize the sharp temperature front moving through the pipe in time. As seen in Fig. 1.17 at early times when the heat flow through the pipe is significantly influenced by advection a sufficient vertical spatial discretization is needed to obtain accurate solutions. At later times, however when the heat front in the pipe disappears and the process is dominated by heat transfer this effect declines.

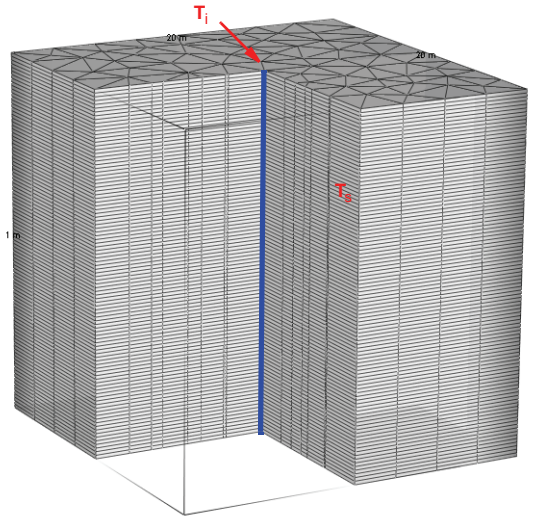

Figure 1.16 Single BHE in a 3D mesh (exaggerated cut view).

We have also interest in comparing the present BHE solution and the analytical results to a fully discretized solution, where the pipe-soil interaction is modeled in a rigorous 3D manner without resorting to heat transfer relationships. Fully discretized 3D models (FD3DM) can be useful as reference solutions in applications, where there are no analytical results. Accordingly, we have to test how such type of 3D models can be developed and how is their accuracy compared to the pre-

ferred BHE solution. Obviously, there is a difficulty in FD3DM to find an appropriate geometric representation of the inner pipe and outer pipe geometries. For the inner pipe processes 1D discrete feature elements[10] are well suited. On the other hand, the pipe walls have to be fully discretized. Figure 1.18 shows the used 3D mesh of a FD3DM for the single pipe-soil interaction, where only the symmetric quarter of the domain has been discretized. The 3D mesh consists of 628,826 pentahedral prismatic elements with 100 layers.

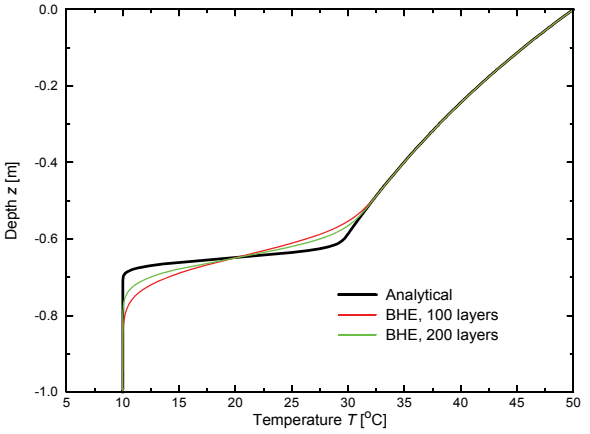

Figure 1.17 Computed temperature profiles in comparison to the analytical solution for the single pipe-soil interaction at $t = 0.02$ d.

As revealed in Fig. 1.18(b) while the vertical discrete feature element of the inner pipe is represented at a single node and the pipe wall is locally discretized, it remains a surplus of the inner pipe domain, which is required to exchange heat between the discrete feature elements and the pipe wall. The domain of the inner pipe surplus has to be assigned to special physical data to hold the physical system correct. A sufficiently small thermal capacity of $\rho^r c^r = 1$ [J m^{-3}K^{-1}] has to be used. Furthermore, the thermal conductivity $\boldsymbol{\Lambda}$ (1-5) should be significantly large in horizontal direction, however, very small in vertical direction. This can be enforced by using the following numerical trick. A very small, but non-zero vertical velocity is assigned to the surplus domain. Then, a longitudinal thermo-dispersivity α_L of zero and a transverse thermo-dispersivity α_T of a very large amount are used in the surplus, which mimics a high thermal anisotropic behavior of the surplus according to (1-5). In the present computation we set $\alpha_T = 10^{12}$ m and $\alpha_L = 0$, where the artificial vertical velocity in the surplus is set to 10^{-6} md^{-1}. In amendment to the parameters (1-173) we need thermal conductivity and capacity of the pipe wall material. The former can be recomputed from the heat transfer coefficient Φ_{fig_o} according to (1-21). We find $\lambda^p_{i1} = \Phi_{fig_o} r^o_{i1} \ln(r^o_{i1}/r^i_{i1}) = 0.031436$ [J m^{-1}s^{-1}K^{-1}]. For the thermal capacity of the pipe wall $\rho^p c^p = 2.1574 \cdot 10^6$[J m^{-3}K^{-1}] is set.

The FD3DM computational results are shown in Fig. 1.19 in comparison to the analytical solution (1-172). The agreement is reasonable, however, difficulties are revealed due to the extremely anisotropic behavior of the inner pipe surplus, which makes the FD3DM simulations expensive and sensitive. It indicates the superior of the efficient BHE solutions to the complex FD3DM simulations, where even a higher accuracy could be attained on a much coarser mesh as shown in Fig. 1.17. It is important to note that there is a certain lag in the FD3DM solution, which does not exist in the BHE computation (*cf.* Figs. 1.17 vs. 1.19).

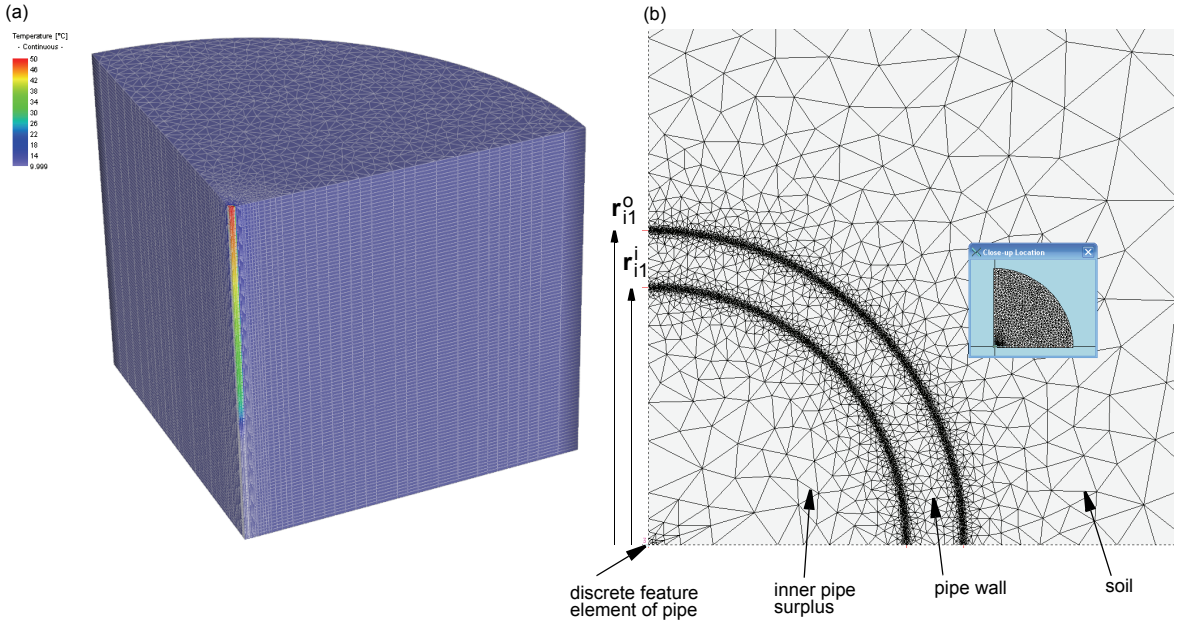

Figure 1.18 FD3DM for studying the single pipe-soil interaction: (a) 3D mesh with temperature distribution at t = 0.02 d, (b) mesh magnified at the single pipe with location of vertical discrete feature elements, the pipe wall and inner pipe surplus of the domain, (c) temperature distribution on top (z = 0) at t = 0.02 d.

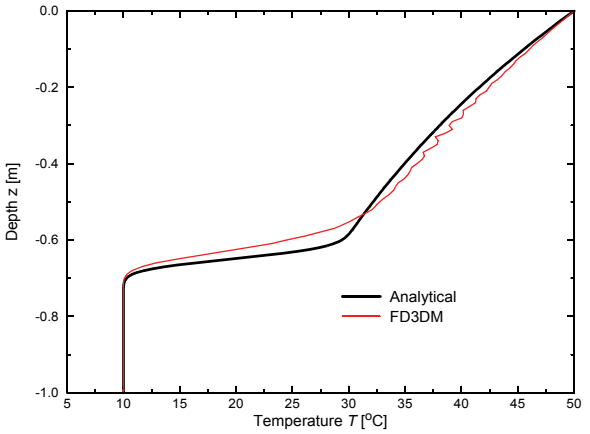

Figure 1.19 Computed temperature profile of the FD3DM solution in comparison to the analytical solution for the single pipe-soil interaction at $t = 0.02$ d.

1.13.3 Transient BHE solution of coaxial pipe system

We consider a BHE coaxial pipe system of annular inlet (CXA type) with parameters as listed in Tab. 1.5. The aquifer domain measures 100 m x 100 m in horizontal directions and 100 m in depth. The used mesh for the BHE solution is shown in Fig. 1.20. The pipe system is located in the centre of the domain, where the mesh is locally refined. For the vertical discretization 100 layers are applied. Two variants of heat injections are considered. The first one refers to a small-rate injection with laminar flow in the coaxial pipes, which is highly driven by thermal conduction. On the other hand, a turbulent flow regime is studied, where advective heat transport in the pipe system is more apparent. In both variants in the time range $(0 < t \leq 90\text{d})$ water with a temperature of 80 °C is injected at the annular pipe-in. At later times $(90\text{d} < t \leq 180\text{d})$ the injection temperature amounts to 10 °C.

Both the Al-Khoury *et al.*'s numerical BHE method and the Eskilson and Claesson's analytical BHE method are applied. The 3D FEFLOW results are compared to a fully discretized finite-difference solution for an axisymmetric 2D formulation of the problem as given by Heidemann. Heidemann has discretized the meridional cross-section by a 72 x 113 grid. The radial extension is taken with 50 m. His grid has been gradually spaced along the radial direction ranging from 1.5 mm up to 1 m. Heidemann used variable time steps between 30 min and 4 hours.

The outlet temperature histories computed by the numerical and analytical BHE methods in comparison to Heidemann's solution are displayed in Fig. 1.21 for the laminar flow and in Fig. 1.23 for the turbulent flow. The results are in a reasonable agreement. For the turbulent case we find an excellent agreement between Heidemann's and the analytical BHE solution as evidenced in Fig. 1.23. We have to note that the present analytical BHE solutions are invalid for variations in a time scale shorter than about 3.5 hours according to the limit (1-107). Using limit (1-108) input variations cannot be simulated even below about 10 hours for laminar flow and about 4 hours for turbulent flow. In Figs. 1.22 and 1.24 the short-term temperature behavior of the analytical and numerical BHE methods are shown for the laminar and turbulent flow cases, respectively. They reveal how the analytical method overestimates the outlet temperature at transient input situations. However, these errors vanishes in long-term predictions if no longer input variations occur as depicted in Figs. 1.21 and 1.23. It has been shown necessary to

assign a high thermal conductivity with an anisotropic behavior for the inner pipe surplus. For the surplus $\lambda^s = 10^3\ \mathrm{J\,m^{-1}s^{-1}K^{-1}}$ and $\lambda^s_{zz}/\lambda^s_{xx,\,yy} = 0$ were chosen, where the porosity ε is set to zero.

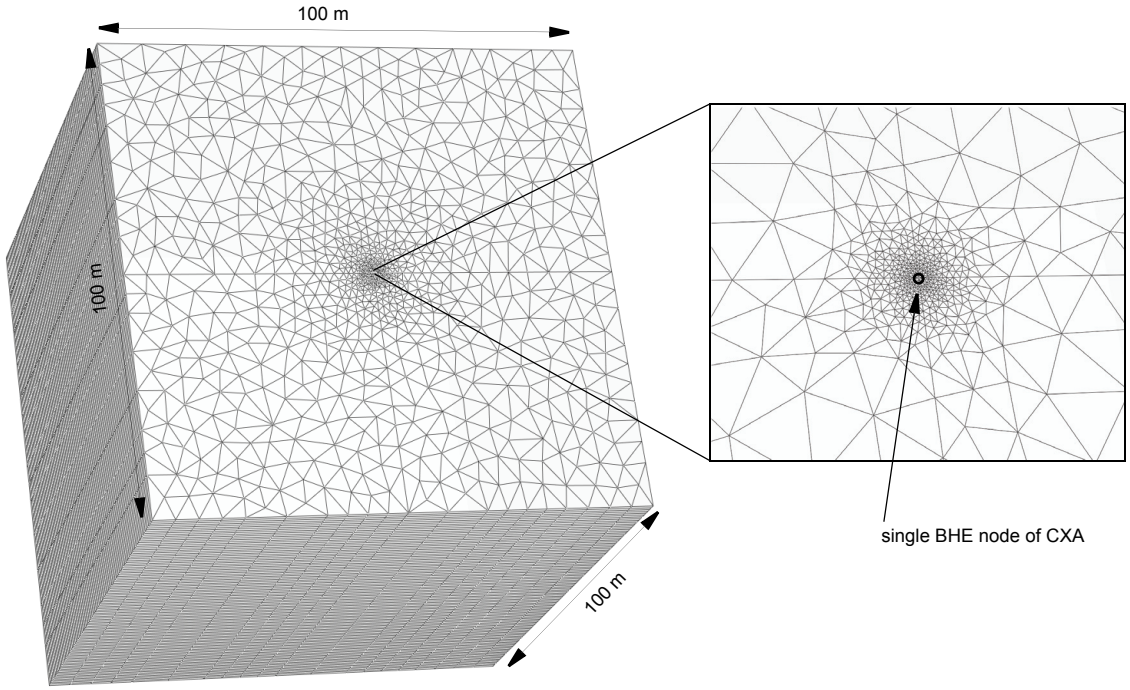

Figure 1.20 Finite-element mesh used for CXA-type BHE model consisting of 239,100 pentahedral elements. Vertical discretization concerns 100 layers.

Table 1.5 Parameters of the CXA exchanger problem

Parameter	Symbol	Value	Unit
Depth of borehole	$\bar{L}$	100	m
Borehole diameter	D	10	cm
Outer diameters of pipe-in	d^o_{i1}	5	cm

Table 1.5 Parameters of the CXA exchanger problem (cont.)

Parameter	Symbol	Value	Unit
Outer diameters of pipe-out	d_{o1}^{o}	2.4	cm
Pipe-in wall thickness	b_{i1}	4	mm
Pipe-out wall thickness	b_{o1}	3	mm
Volumetric heat capacity of pipe walls	$\rho^p c^p$	$2.1574 \cdot 10^6$	$\mathrm{J\,m^{-3}K^{-1}}$
Thermal conductivities of pipe walls	$\lambda_{i1}^{p}, \lambda_{o1}^{p}$	0.38	$\mathrm{J\,m^{-1}s^{-1}K^{-1}}$
Initial temperature	$T_s(0)$	10	°C
Reference temperature	T_o^R	10	°C
Total flow discharge of refrigerant: *laminar flow* *turbulent flow*	 Q_r^{laminar} $Q_r^{\text{turbulent}}$	 1.0931 21.8624	 $\mathrm{m^3 d^{-1}}$ $\mathrm{m^3 d^{-1}}$
Total heat input rate: *laminar flow*	$Q_h^{\text{laminar}}(t)$	$3.1602 \cdot 10^8$ $(0 < t \le 90\mathrm{d})$ 0.0 $(90\mathrm{d} < t \le 180\mathrm{d})$	$\mathrm{J\,d^{-1}}$
turbulent flow	$Q_h^{\text{turbulent}}(t)$	$6.3203 \cdot 10^9$ $(0 < t \le 90\mathrm{d})$ 0.0 $(90\mathrm{d} < t \le 180\mathrm{d})$	$\mathrm{J\,d^{-1}}$
Volumetric heat capacity of refrigerant	$\rho^r c^r$	$4.12984 \cdot 10^6$	$\mathrm{J\,m^{-3}K^{-1}}$
Thermal conductivity of refrigerant	λ^r	0.65	$\mathrm{J\,m^{-1}s^{-1}K^{-1}}$
Volumetric heat capacity of grout	$\rho^g c^g$	$2.19 \cdot 10^6$	$\mathrm{J\,m^{-3}K^{-1}}$
Thermal conductivity of grout	λ^g	2.3	$\mathrm{J\,m^{-1}s^{-1}K^{-1}}$
Porosity of soil	ε	0	1

Table 1.5 Parameters of the CXA exchanger problem (cont.)

Parameter	Symbol	Value	Unit
Volumetric heat capacity of soil	$\rho^s c^s$	$2.21 \cdot 10^6$	$J\,m^{-3}K^{-1}$
Thermal conductivity of soil	λ^s	2.2	$J\,m^{-1}s^{-1}K^{-1}$
Anisotropy factor	$\lambda^s_{zz}/\lambda^s_{xx,yy}$	1	1
Thermal conductivity of pipe surplus	λ^s	10^3	$J\,m^{-1}s^{-1}K^{-1}$
Anisotropy factor of pipe surplus	$\lambda^s_{zz}/\lambda^s_{xx,yy}$	0	1
Computed heat transfer coefficients:			
laminar flow			
pipe-in to grout	Φ_{fig}	52.955	$[J\,m^{-2}s^{-1}K^{-1}]$
pipe-in to pipe-out	Φ_{ff}	52.068	$[J\,m^{-2}s^{-1}K^{-1}]$
grout to soil	Φ_{gs}	195.74	$[J\,m^{-2}s^{-1}K^{-1}]$
turbulent flow			
pipe-in to grout	Φ_{fig}	69.326	$[J\,m^{-2}s^{-1}K^{-1}]$
pipe-in to pipe-out	Φ_{ff}	134.14	$[J\,m^{-2}s^{-1}K^{-1}]$
grout to soil	Φ_{gs}	195.74	$[J\,m^{-2}s^{-1}K^{-1}]$
Computed thermal resistances:			
laminar flow			
pipe-in to grout	R_{fig}	0.14312	$[m\,s\,K\,J^{-1}]$
pipe-in to pipe-out	R_{ff}	0.33963	$[m\,s\,K\,J^{-1}]$
grout to soil	R_{gs}	0.016262	$[m\,s\,K\,J^{-1}]$
turbulent flow			
pipe-in to grout	R_{fig}	0.10932	$[m\,s\,K\,J^{-1}]$
pipe-in to pipe-out	R_{ff}	0.13183	$[m\,s\,K\,J^{-1}]$
grout to soil	R_{gs}	0.016262	$[m\,s\,K\,J^{-1}]$

The present turbulent flow case of a single CXA-type BHE gives opportunity for a mesh convergence study, where the level of mesh refinement around the singular BHE node is systematically increased. This will reflect the statements of Chapter 1.11 regarding an optimal mesh design for BHE solutions. We test the accuracy of the solution for a stepwise local refinement of mesh Υ around the BHE node according to (*cf.* Fig. 1.25)

$$\Upsilon_l \qquad l = 0, 1, 2, \ldots, 8 \tag{1-174}$$

where l is the refinement level of mesh Υ_l. Starting with Υ_0 consisting of a regular triangular tesselation

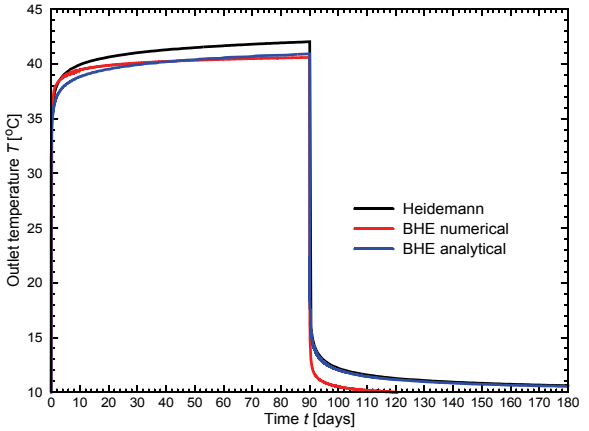

Figure 1.21 Temperature history at pipe outlet of the CXA-type BHE for laminar flow compared to Heidemann's solution.

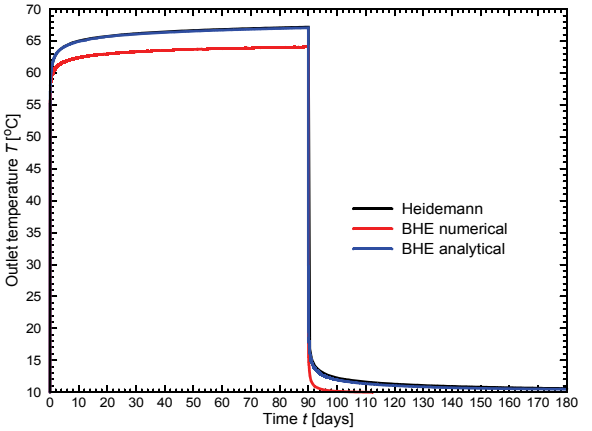

Figure 1.23 Temperature history at pipe outlet of the CXA-type BHE for turbulent flow compared to Heidemann's solution.

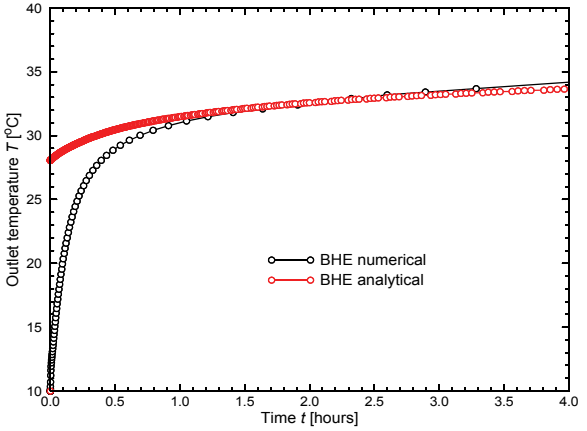

Figure 1.22 Short-term temperature history at pipe outlet of the CXA-type BHE for laminar flow.

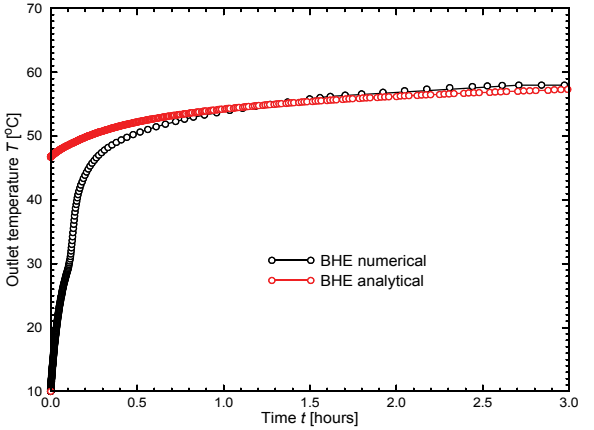

Figure 1.24 Short-term temperature history at pipe outlet of the CXA-type BHE for turbulent flow.

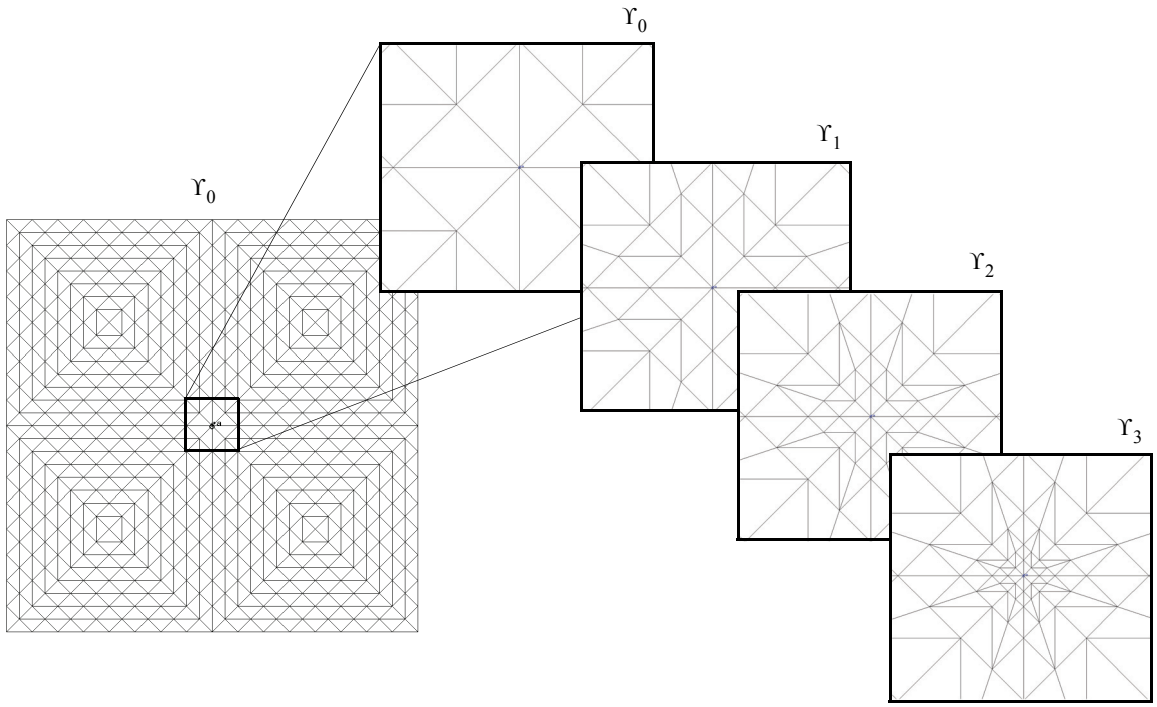

Figure 1.25 Different mesh refinement levels for CXA-type BHE located in the centre of the domain ($100x100m^2$). Vertical discretization concerns 20 layers.

characterized by a BHE nodal distance Δ of about 4.42 m, the number of triangular prisms *NE* and total number of nodes *NP* then increase according to the refinement level l, while the BHE nodal distance Δ is halved in value for each refinement level l:

$$\begin{aligned} NE &= 32(32+l)\cdot(NS-1) \\ NP &= [16(34+l)+1]\cdot NS \\ \Delta_l &= 2^{-l}\Delta \qquad \Delta \approx \frac{\bar{L}}{32}\sqrt{2} = 4.42\ \text{m} \qquad NS = 21 \end{aligned} \tag{1-175}$$

where the BHE node (in the central position of the domain) is locally refined from level to level l (see Fig. 1.25). For the mesh convergence test only a vertical discretization consisting of 20 layers (number of slices $NS = 21$) with a vertical spacing of $\Delta z = \bar{L}/(NS-1) = 5$ m is considered.

The simulations by using the analytical BHE method are performed up to a maximum refinement level of $l = 8$. At that level the BHE nodal distance

with about 1.7 cm is clearly smaller than the physical borehole radius of $r_b = D/2 = 5$ cm. Using estimation method 1 (1-164) from Chapter 1.11 we can expect an optimal BHE nodal distance Δ of about 0.333 m (with $n = 8$), which would require a refinement level of about 4 ($\Delta_4 \approx 0.276$ m) to attain suited accuracy. Indeed, the simulations reveal that the best agreement to Heidemann's reference solution is for Υ_4 as evidenced in Fig. 1.26 for the turbulent flow case. As revealed both coarse meshes ($\Upsilon_l, l < 4$) and higher dense meshes ($\Upsilon_l, l > 4$) under- and over-estimates, respectively, the reference solution for the outlet temperature. If the nodal distance falls below the physical borehole radius r_b the elements within $\Delta \le r_b$ have to assigned to a high thermal conductivity to break the further increase of the temperature at the borehole. The method 2 as described in Chapter 1.11 is also tested for an optimal BHE nodal distance Δ. Method 2 results a value of $\Delta = 0.277$ m, which is somewhat smaller than the method 1's estimation of 0.333 m, but also confirms refinement level Υ_4 as the best, say optimal, mesh.

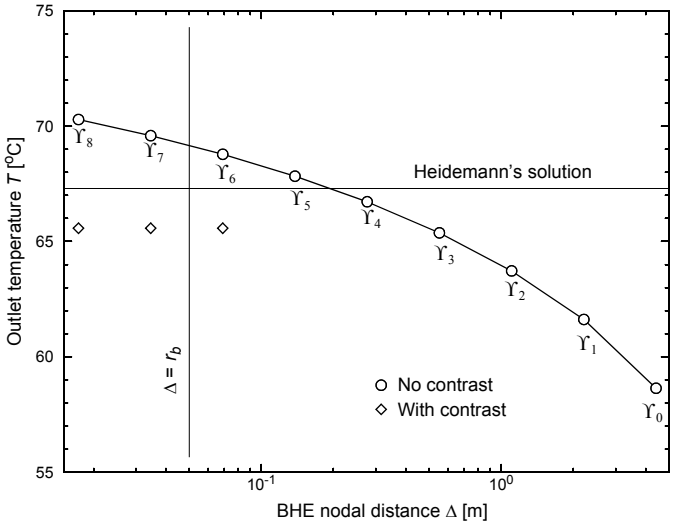

Figure 1.26 Outlet temperature at $t = 90$ d of the CXA-type BHE for turbulent flow versus the BHE nodal distance Δ. Refinement levels Υ_l ($l = 0,...,8$) in comparison to Heidemann's reference solution. For levels l = 6-8 solutions with high contrast of the thermal conductivity $\lambda^s = 10^3$ J m^{-1}s^{-1}K^{-1} for elements smaller than physical borehole radius $r_b = 0.05$ m are also incorporated. Analytical BHE method is used.

The results for the optimal Υ_4 mesh give very good agreement with Heidemann's reference solution as shown in Fig. 1.27 for the full history of outlet temperature. Although the mesh of level Υ_4 is about 10 times

coarser (consisting only of 23,040 pentahedral elements) than the mesh studied above (Fig. 1.20) consisting of 239,100 pentahedral elements, the quality of the results is comparable (*cf.* Fig. 1.27 vs. Fig. 1.23).

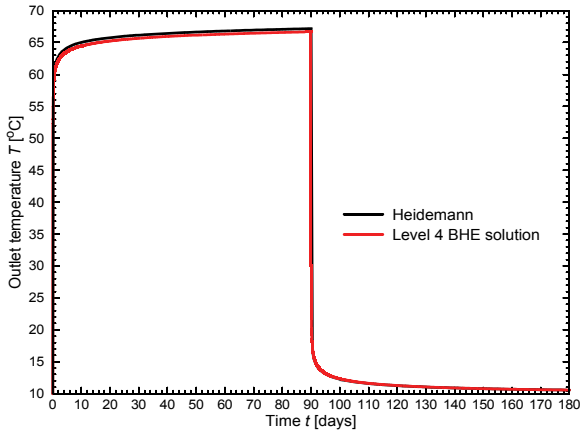

Figure 1.27 Outlet temperature history of the CXA-type BHE for turbulent flow simulated with optimal mesh of refinement level 4, Υ_4 (analytical BHE solution) compared to Heidemann's solution.

1.13.4 BHE solution versus fully discretized 3D model (FD3DM) solution applied to a double U-shape pipe system

Comparisons between the proposed BHE solution and a fully discretized 3D model solution (FD3DM) are performed for heating operation of a 2U configuration located in central position of an aquifer domain measuring 20 m x 20 m in horizontal directions and 55 m in depth. The used meshes for both solutions are shown in Fig. 1.28 revealing a much more refined tessellation for FD3DM to discretize appropriately the interior geometric structure of the 2U exchanger. In both meshes, however, the vertical discretization is the same by using 55 layers. For the 2U exchanger problem the used parameters are summarized in Tab. 1.6. In FD3DM 1D discrete feature (fracture) elements have been used to model the internal pipes. It was necessary to assign the inner pipe surplus to a high thermal conductivity of solid with anisotropy. For the surplus we took a value of $\lambda^s = 10^3\ \mathrm{J\,m^{-1}s^{-1}K^{-1}}$ with an anisotropy factor of $\lambda^s_{zz}/\lambda^s_{xx,yy} = 0$. In the surplus we use a porosity ε of zero.

Table 1.6 Parameters of the 2U exchanger problem

Parameter	Symbol	Value	Unit
Depth of borehole	$\bar{L}$	55	m
Borehole diameter	D	12	cm
Outer diameters of pipes-in	d^o_{i1}, d^o_{i2}	3.2	cm
Outer diameters of pipes-out	d^o_{o1}, d^o_{o2}	3.2	cm
Pipes-in wall thicknesses	b_{i1}, b_{i2}	2.9	mm

Table 1.6 Parameters of the 2U exchanger problem (cont.)

Parameter	Symbol	Value	Unit
Pipes-out wall thicknesses	b_{o1}, b_{o2}	2.9	mm
Pipe distance	w	4.2	cm
Volumetric heat capacity of pipe walls	$\rho^p c^p$	$2.1574 \cdot 10^6$	$J\,m^{-3}K^{-1}$
Thermal conductivities of pipe walls	$\lambda^p_{i1}, \lambda^p_{i2}, \lambda^p_{o1}, \lambda^p_{o2}$	0.38	$J\,m^{-1}s^{-1}K^{-1}$
Total flow discharge of refrigerant	Q_r	38.284	$m^3 d^{-1}$
Total heat input rate	Q_h	$6.3242 \cdot 10^9$	$J\,d^{-1}$
Reference temperature	T^R_o	10	^oC
Inlet temperature	T_i	50	^oC
Volumetric heat capacity of refrigerant	$\rho^r c^r$	$4.12984 \cdot 10^6$	$J\,m^{-3}K^{-1}$
Thermal conductivity of refrigerant	λ^r	0.65	$J\,m^{-1}s^{-1}K^{-1}$
Volumetric heat capacity of grout	$\rho^g c^g$	$2.19 \cdot 10^6$	$J\,m^{-3}K^{-1}$
Thermal conductivity of grout	λ^g	2.3	$J\,m^{-1}s^{-1}K^{-1}$
Porosity of soil	ε	0.2	1
Porosity of pipe surplus	ε	0	1
Volumetric heat capacity of groundwater	$\rho^f c^f$	$4.2 \cdot 10^6$	$J\,m^{-3}K^{-1}$
Volumetric heat capacity of soil	$\rho^s c^s$	$2.405 \cdot 10^6$	$J\,m^{-3}K^{-1}$
Thermal conductivity of groundwater	λ^f	0.65	$J\,m^{-1}s^{-1}K^{-1}$
Thermal conductivity of soil	λ^s	2.46	$J\,m^{-1}s^{-1}K^{-1}$
Anisotropy factor	$\lambda^s_{zz}/\lambda^s_{xx,yy}$	1	1
Thermal conductivity of pipe surplus	λ^s	10^3	$J\,m^{-1}s^{-1}K^{-1}$
Anisotropy factor of pipe surplus	$\lambda^s_{zz}/\lambda^s_{xx,yy}$	0	1
Longitudinal thermo-dispersivity of aquifer	α_L	0.5	m

Table 1.6 Parameters of the 2U exchanger problem (cont.)

Parameter	Symbol	Value	Unit
Transverse thermo-dispersivity of aquifer	α_T	0.05	m
Initial temperature	$T_s(0)$	10	^oC
Computed heat transfer coefficients:			
pipe-in to grout	Φ_{fig}	91.624	$[J\ m^{-2}s^{-1}K^{-1}]$
pipe-out to grout	Φ_{fog}	91.624	$[J\ m^{-2}s^{-1}K^{-1}]$
grout to grout 1	Φ_{gg1}	802.43	$[J\ m^{-2}s^{-1}K^{-1}]$
grout to grout 2	Φ_{gg2}	31.702	$[J\ m^{-2}s^{-1}K^{-1}]$
grout to soil	Φ_{gs}	181.02	$[J\ m^{-2}s^{-1}K^{-1}]$
Computed thermal resistances:			
pipe-in to grout	R_{fig}	0.1326	$[m\ s\ K\ J^{-1}]$
pipe-out to grout	R_{fog}	0.1326	$[m\ s\ K\ J^{-1}]$
grout to grout 1	R_{gg1}	0.02077	$[m\ s\ K\ J^{-1}]$
grout to grout 2	R_{gg2}	0.26287	$[m\ s\ K\ J^{-1}]$
grout to soil	R_{gs}	0.05861	$[m\ s\ K\ J^{-1}]$

A comparison between the BHE solutions to fully discretized 3D model (FD3DM) is shown in Fig. 1.29 for the short-term outlet temperature history, in Fig. 1.30 for the long-time outlet temperature history and in Fig. 1.31 for the vertical temperature profile after 12 hours. As revealed the agreement between the different solutions is quite well. For long-term predictions the analytical BHE simulation has shown reasonably accurate and fast, while the numerical BHE computations became superior to the analytical BHE solution at short-term predictions and in a well agreement with the FD3DM results from beginning. In Fig. 1.31 the vertical temperature profile of grout is not evaluated for FD3DM because the grout temperature considerably varies within the mesh nodes in the borehole at that early time.

For the FD3DM a forward Adams-Bashforth/backward trapezoid time integration scheme with a RMS error tolerance of 10^{-4} has been used. It took 276 time steps for the simulation period of 365 days. For the BHE solutions always a forward Euler/backward Euler time marching predictor-corrector scheme with a RMS error tolerance of 10^{-3} was preferred due to better robustness for this class of problems. The analytical BHE required only 227 time steps. In contrast, the numerical BHE computations failed for the long-term run because the adaptive time step control could not increase the time steps anymore and a very large number of time steps would follow. Obviously, this is caused by random effects triggered from the stiff matrix system by poor numerical precision of the only 8 byte floating point mantissa.

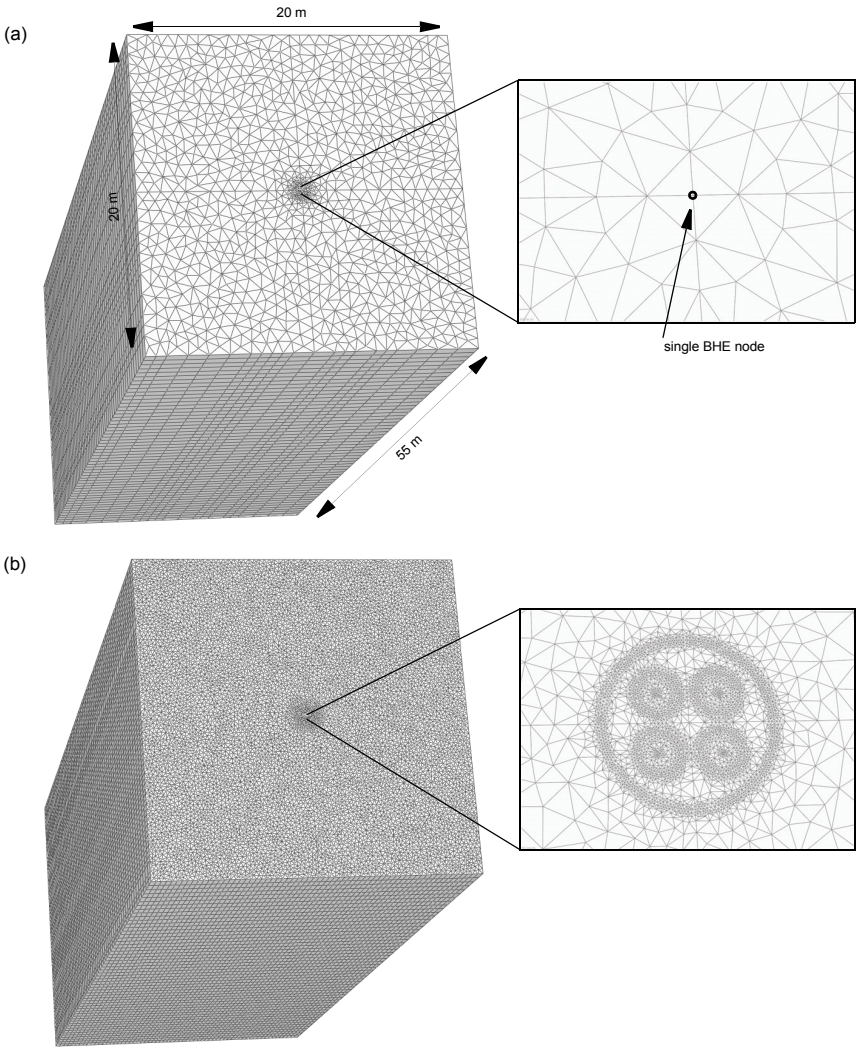

Figure 1.28 Finite-element meshes for (a) BHE consisting of 130,185 pentahedral elements and (b) FD3DM consisting of 1,204,665 pentahedral elements. Both meshes are vertically discretized by 55 layers.

The good agreement of the BHE solutions with the FD3DM results demonstrates the accuracy and practical applicability of the new BHE modeling strategy. Its numerical efficiency and capability will be more apparent for arrays of BHE.

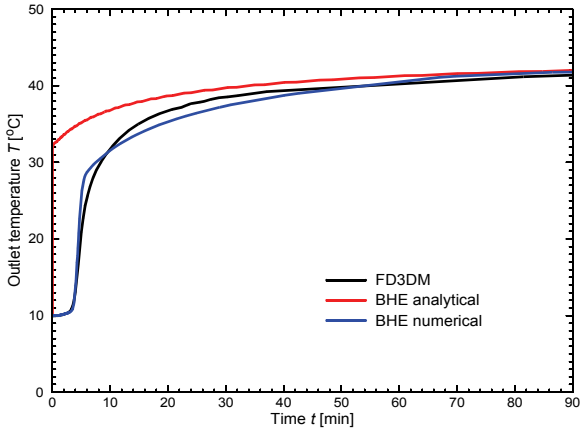

Figure 1.29 Short-term outlet temperature history of the BHE solution in comparison to the fully discretized 3D model (FD3DM) solution measured at the pipe's outlet.

1.14 Application to Borehole Thermal Energy Stores

Borehole Thermal Energy Stores (BTES) consist of a large number of borehole heat exchangers typically installed with spacing in the range of two to five meters as the thermal interaction of the individual borehole heat exchangers is essential for an efficient storage process. BTES can be a reasonable technical and economical alternative - depending on the local geological and hydrogeological situation - to other techniques of heat

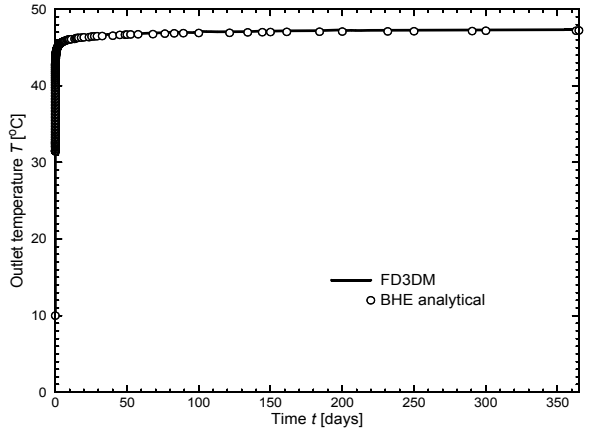

Figure 1.30 Long-term outlet temperature history of the BHE solution in comparison to the fully discretized 3D model (FD3DM) solution measured at the pipe's outlet.

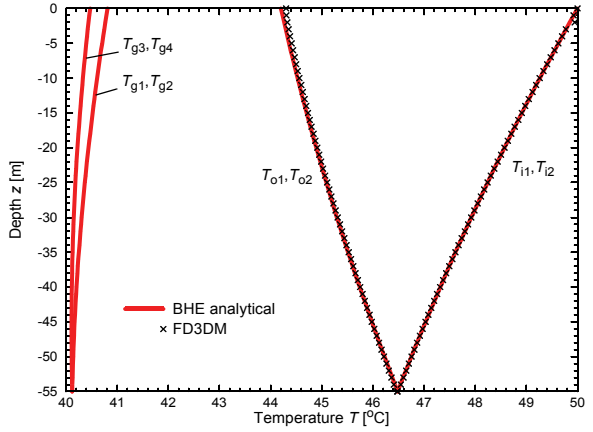

Figure 1.31 Analytical BHE solution of temperature profile at t = 12 hours in comparison to the fully discretized 3D model (FD3DM).

storage for the use in solar assisted district heating systems with seasonal heat storage. However, BTES are very sensitive to groundwater flow. Both for permit procedures required by the authorities and for plant-engineering issues, simulations are needed which are capable of predicting the three-dimensional temperature profile in the underground and the thermal efficiency of the store. Together with the new BHE option of FEFLOW the simulation of such installations is a feasible task.

1.14.1 Dynamic coupling with the energy simulation program TRNSYS

In order to simulate the interaction of an array of BHE with the supply of energy to housing areas advanced capabilities are necessary. Using FEFLOW's open programming interface IFM a *Qt*-based module has been developed which allows to couple FEFLOW with the transient systems simulation code TRNSYS[17,8]. This way it is possible to model the complete energy transfer cycle for instance between an array of solar panels, the connected buildings and a subsurface heat storage system together with the thermal interaction with the surrounding rocks. The FEFLOW-TRNSYS-coupling module processes a variable number of BHE which can be connected using arbitrarily complex circuits. An example of the modul's user interface is shown in Fig. 1.32.

The interface enables the exchange of a pipe inlet flow rate and inlet temperature from TRNSYS to FEFLOW and of the resulting outlet temperature back to TRNSYS. In addition, the flow direction can be switched and the temperature of selected observation points can be reported to TRNSYS. This coupling is performed using the remote procedure protocol RPC[7]. The counterpart to FEFLOW's IFM module is a new developed TRNSYS type called Type331.

For users who want to interlink BHE without using TRNSYS there is also a standalone option available. In this case the operation is controlled by three power functions (for flow rate, temperature and flow direction).

1.14.2 Numerical simulation of real-site BTES Crailsheim, Germany

To investigate the influence of moving groundwater on BTES of real dimension, the recently built BTES in Crailsheim, south-west Germany was simulated. For more information about Crailsheim BTES see Bauer *et al*.[5] and Rieger[16]. The Crailsheim BTES consists of 80 double U-tube BHE with 55 m in length installed on a circular area with 30 m in diameter. The BTES is situated in a geology comprising two aquifers. It is covered with soil and heat insulation (Tab. 1.7). The properties of the used BHE are given in Tabs. 1.8 and 1.9. Within FEFLOW's new BHE configuration dialog the Eskilson and Claesson's analytical BHE method was chosen. Only one iteration is performed per each time, but a stronger RMS error tolerance of 10^{-6} concerning the AB/TR automatic time-stepping control was selected. With these selections a fast but also accurate computation could be achieved. The linkage of the single BHE within the BHE array is shown in Fig. 1.32. It reveals that always two BHE are interlinked, where one BHE located on an outer circular range is connected to a

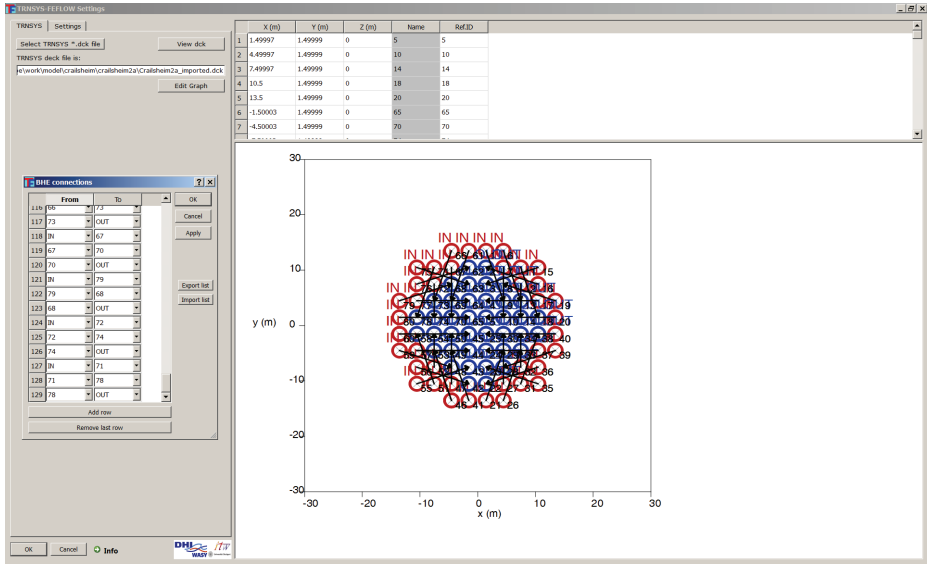

Figure 1.32 The user interface of the new IFM module for connecting BHE arrays.

BHE located on an inner circular range within the BHE array.

For the finite element meshing of the BHE array additional point add-ins were introduced. This was particularly done to attain an optimal nodal distance Δ around each single BHE of the array. According to Chapter 1.11 an optimal BHE nodal distance Δ of about 0.4 m (by using n = 6) was chosen for the unstructured mesh. Finally, the total study area of 2000 m x 2000 m was discretized by 21,337 triangular prismatic elements per layer. In the vertical direction the used finite element mesh consists of 24 layers with a thickness between 0.5 m and 40 m; within the BTES the slice distance is 5 m in maximum.

The simulation was conducted for a time range of five years featuring an alternation between one heat inserting period and one heat extracting period of approximately six months per year. In addition to this cycle there is also a daily change of the inflow temperature during the heat-storing period. Due to the day/night variation a cycle of 8 hours with a temperature of 80°C and 16 hours with 40°C can be presumed. The latter temperature represents the output temperature of a buffer storage tank. Since a computation over 5 years with these daily fluctuations is time consuming, an approximated time-weighted mixture temperature of

53.33°C is used for the first cycle (heat-storage). After a time range of 185 days the flow direction of the refrigerant is reversed and the inlet temperature is reduced to 10°C (period of heat extraction). These two cycles are repeated for the following years, five in total. The settings of the TRNSYS deck file are performed in the so called Simulation Studio of TRNSYS (Fig. 1.33). The total inflow rate for all 80 BHE is 8064 l/h.

Table 1.7 Simulation parameters of Crailsheim BTES site

Formation	Extent below top ground surface [m]	Hydraulic gradient [-]	Hydraulic conductivity K [ms^{-1}]	Porosity ε [-]	Volumetric heat capacity $\rho^s c^s$ [$Jm^{-3}K^{-1}$]	Thermal conductivity λ^s [$Jm^{-1}s^{-1}K^{-1}$]
Soil cover	0 - 1.5	/	$1 \cdot 10^{-12}$	$1 \cdot 10^{-6}$	$2.20 \cdot 10^{6}$	2.10
Heat insulation	1.5 - 2	/	$1 \cdot 10^{-12}$	$1 \cdot 10^{-6}$	$1.28 \cdot 10^{2}$	0.08
Sandstone (Keuper)	2 - 24	0.01	$5.7 \cdot 10^{-6}$	0.01	$2.60 \cdot 10^{6}$	1.95
Limestone (Muschelkalk)	24 - 61	/	$1 \cdot 10^{-9}$	0.01	$2.40 \cdot 10^{6}$	2.46
	61 - 103	0.0045	$1.31 \cdot 10^{-4}$	0.01	$2.40 \cdot 10^{6}$	2.46
Basement	103 - 200	/	$1.31 \cdot 10^{-4}$	0.01	$2.40 \cdot 10^{6}$	2.46

Table 1.8 Physical properties of 2U BHE used for Crailsheim BTES site

Property	fluid	pipe	grout
ρc [$Jm^{-3}K^{-1}$]	$4.13 \cdot 10^{6}$	$2.16 \cdot 10^{6}$	$2.19 \cdot 10^{6}$
λ [$Jm^{-1}s^{-1}K^{-1}$]	0.6405	0.38	2.3
μ [$kg\ m^{-1}s^{-1}$]	$5.47 \cdot 10^{-4}$	-	-

Table 1.9 Geometric relations of 2U BHE used for Crailsheim BTES site

Geometry	[m]
d_i^i, d_o^i	0.0262
d_i^o, d_o^o	0.032
s	0.09
D	0.13
$\bar{L}$	55

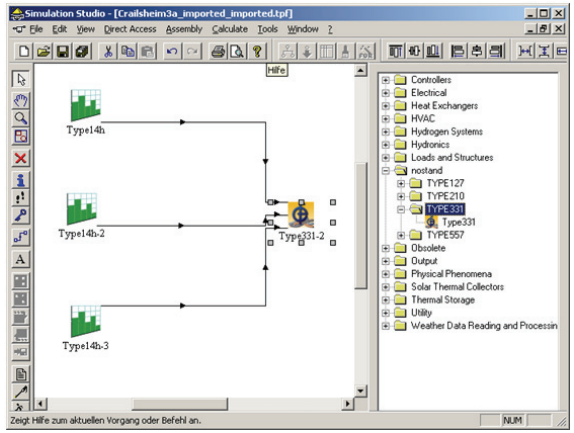

Figure 1.33 Linking the new TRNSYS type 331 for connecting FEFLOW in the TRNSYS Simulation Studio.

Figure 1.34 shows two temperature profiles of the subsurface at different times for the fifth year of heat injection/extraction. In Fig. 1.35 the history of outlet temperatures of all 80 BHE is plotted. These figures illustrate the impact of alternation of the seasonal heat loading and extraction of the storage and reveal how those BHE which are located in the inner circular range of the BHE array get water which has been already cooled down because it circulated before through the outer range of the BHE array - or vice versa.

Figure 1.36 depicts a cross-sectional profile of temperature along the main direction of groundwater flow after a fifth year BTES operation of alternating heat loading and extraction and indicates the movement of heat slowly drifting outside the BTES due to thermal conduction and advection. It is obvious that the real hydrogeological conditions of the BTES site are important for efficiency and reliability of the subsurface heat storage system. Related environmental impact studies for a long-term operation of BTES become necessary. The present simulation results represent a scenario with use of schematic hydrogeological parameters, which was confirmed by the regular authorities for Geology, Resources and Mining of Baden-Württemberg (LGRB). Further more detailed investigations and modeling studies for the BTES Crailsheim site are ongoing.

1.15 Summary and Conclusions

In this paper, the details in numerical modeling of single BHE and arrays of BHE in FEFLOW are reported. Four types of *vertical* BHE are supported: double U-shape (2U) pipe, single U-shape (1U) pipe,

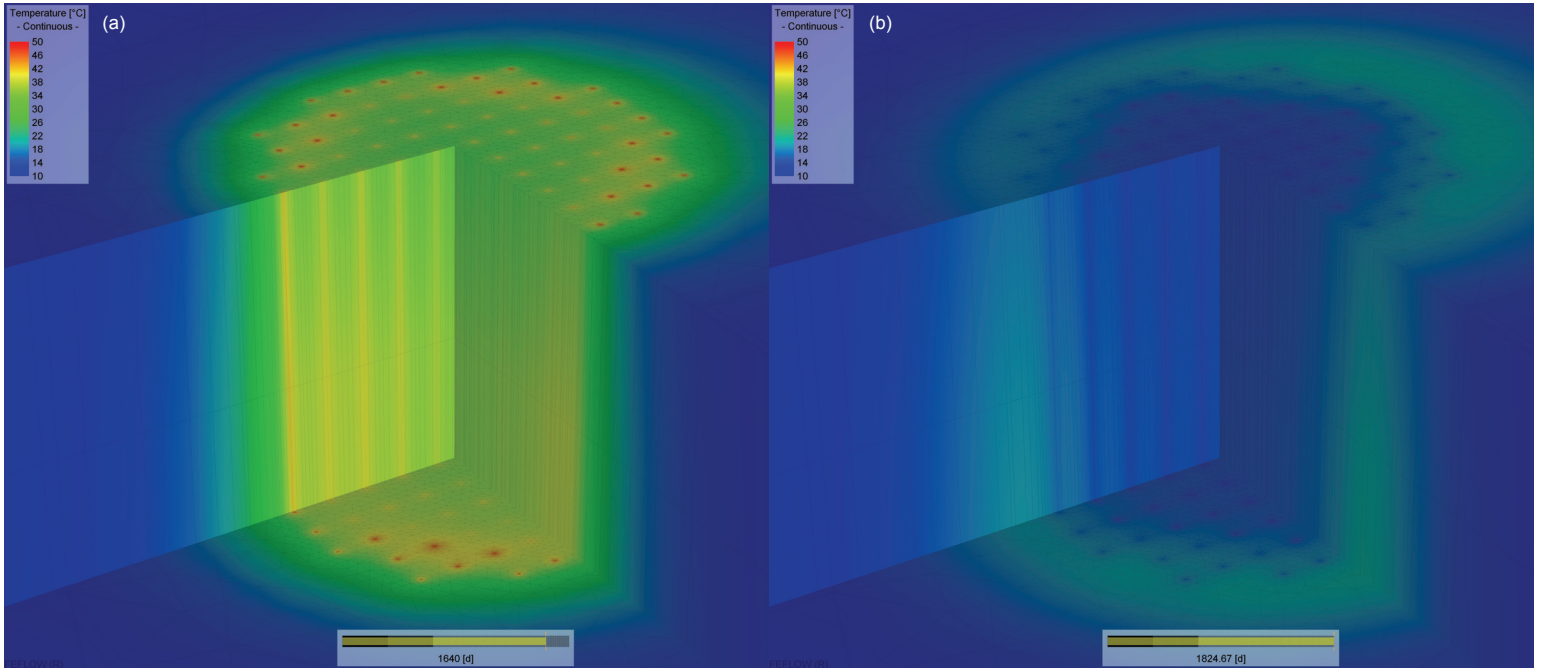

Figure 1.34 Temperature distribution around the array of 80 BHE computed with FEFLOW and coupled with TRNSYS: (a) at the end of the heat injection period after 4 years and 180 days. (b) after 5 years.

coaxial pipe with annular (CXA) and centred (CXC) inlet. BHE system modeling is applicable for 3D heat or thermohaline problems. The thermal processes can be dependent on the groundwater flow regime, thermal capacity and conductivity of the subsurface as well as fluid viscosity and buoyancy effects if density variable flow conditions occur. For handling BHE arrays an IFM interface module has been developed, which is capable of linking with the energy simulation program TRNSYS.

The paper describes the basic theory of BHE modeling. Starting with the general formulation of the balance equations for flow and heat transport in BHE pipe system and surrounding soil, efficient finite element solution strategies are derived and thoroughly described. There two principal approaches: (1) The analytical BHE method based on Eskilson and Claesson's solution, (2) numerical BHE method based on Al-Khoury et al.'s solution. While the latter is more general and accurate both for short-term and long-term analyses, the analytical solutions strategy has shown

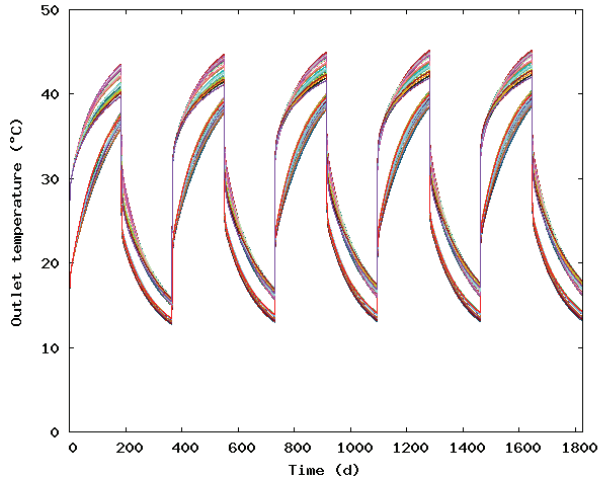

Figure 1.35 History of outlet temperatures of all 80 BHE.

highly efficient, precise and robust, however, not applicable for short-term processes (a temporal scale in order of seconds, minutes or few hours). But, this limitation of the analytical method is usually not relevant for real BHE applications, where the thermal processes is measured in days and years.

The BHE systems are modeled by 1D finite-element representations, where the thermal exchange both within the BHE configurations consisting of pipes and grout material zones and with the surrounding soil is subjected to thermal transfer relationships. For this purpose improved relationships for thermal resistances of BHE are introduced. Pipe-to-grout thermal transfer possesses multiple grout points for 2U and 1U BHE to attain a more accurate modeling. The numerical solution of the final 3D problems is performed via a widely non-sequential (essentially non-iterative) coupling strategy for the BHE and porous medium discretization.

Using BHE in regional discretizations optimal conditions of mesh spacing around singular BHE nodes are recommended. The direct estimation of the nodal distance can be sufficient under practical conditions. Such optimal meshes have shown superior to those discretizations which are either too fine or too coarse. Commonly, over-refined meshes around BHE nodes require the assignment of high contrast of thermal conductivity of elements within the BHE radius. But, an optimal mesh spacing around BHE avoids such kind of manipulations and the solutions become faster and more (or similarly) accurate, even realized on coarser meshes.

To input all relevant BHE data specific dialogs are available in FEFLOW. The computational results for BHE are displayed in diagrams showing vertical temperature profile and outlet temperature in time for each BHE. The number of BHE can be arbitrary. To support BHE arrays an IFM module has been developed which provides tools for interlink BHE. Furthermore, this module also allows the coupling of FEFLOW with the energy simulation program TRNSYS to control and dispatch the complete energy transfer cycle for real-site applications.

To illustrate and benchmark FEFLOW's BHE functionality, a number of test and example problems are posed and solved. The proposed BHE solution strategies result very good agreements with analytical solutions. Detailed comparisons to reference finite-difference solutions are given for a single coaxial-type BHE under laminar and turbulent flow of refrigerant. It shows the advantage of the analytical Eskilson and Claessson's solution method for long-term analysis. If

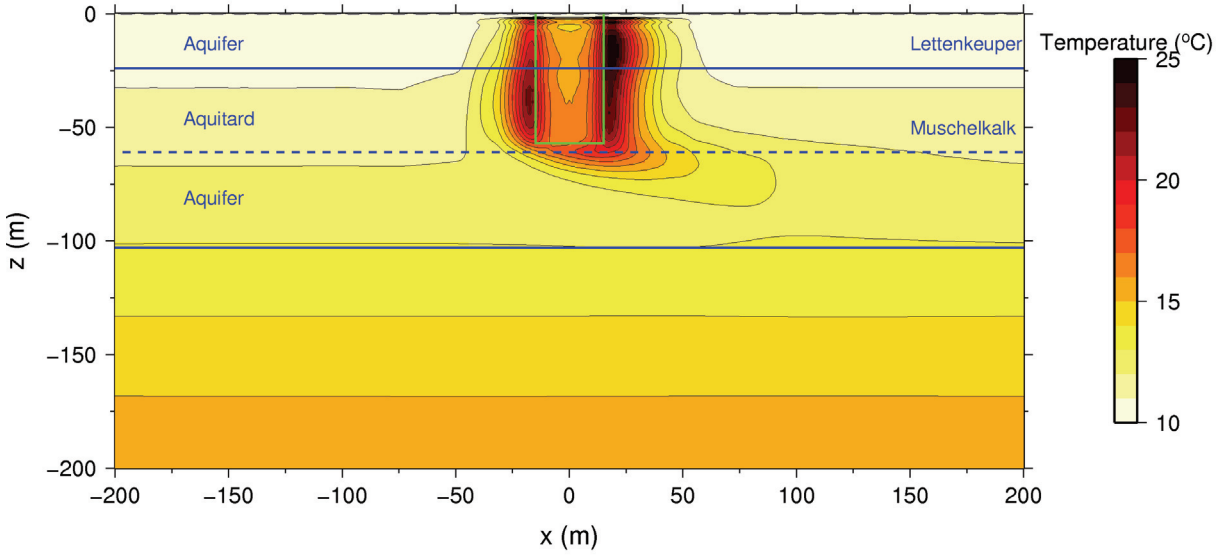

Figure 1.36 Cross-sectional temperature profile through the center of the BTES (green line) oriented to the main groundwater flow direction after the fifth year of BTES operation.

applied to optimal mesh configurations the solutions have shown very efficient and accurate. Additionally, comparisons are provided to finite-element solutions resulting from a fully discretized 3D model (FD3M). The good agreement of the BHE solutions with the FD3DM results demonstrates the accuracy and practical applicability of the new BHE modeling strategy. Finally, a practical application to BTES consisting of 80 BHE is given for the real-site BTES Crailsheim, Germany. The simulations are supported by the specifically developed FEFLOW-TRNSYS coupling module. Scenarios indicate the effect of the groundwater flow regime on efficiency and reliability of the subsurface heat storage system.

Acknowledgements

The authors acknowledge Rafid Al-Khoury (Delft University of Technology, The Netherlands) for his interest, suggestions and useful discussions of the work. This work was supported by the German Federal Ministry for the Environment, Nature Conservation and Nuclear Safety under Grant No. AZ 02E2-41V5034. The authors are grateful for this support.

References

1. Al-Khoury, R., Bonnier, P.G., Brinkgreve, R.B., Efficient finite element formulation for geothermal heating systems. Part I: Steady state. *Int. J. Numer. Meth. Engng.* **63** (2005) 7, 988-1013.
2. Al-Khoury, R., Bonnier, P.G., Efficient finite element formulation for geothermal heating systems. Part II: Transient. *Int. J. Numer. Meth. Engng.* **67** (2006) 5, 725-745.
3. Axelsson, O., *Iterative solution methods*. Cambridge University Press, 1994.
4. Bauer, D. Kompensation unterschiedlicher örtlicher Diskretisierungen des 3D-FE-Netzes um 1D-Erdwärmesonden (compensation of spatially varying 3D finite element meshes around 1D borehole heat exchangers). Internal status report ITW Stuttgart, 2009.
5. Bauer, D., Heidemann, W., Müller-Steinhagen, H., Diersch, H.-J.G., Modelling and simulation of groundwater influence on borehole thermal energy stores. Proceedings *Effstock - 11th International Conference on Energy Storage*, Stockholm, Sweden, 2009.
6. Bear, J., *Dynamics of fluids in porous media.* Amer. Elsevier, N.Y., 1972.
7. Birrell, A.D., Nelson, B.J., Implementing remote procedure calls. ACM *Transactions on Computer Systems* **2** (1984) 1, 39-49.
8. Bradley, D. E., Kummert, M., New evolutions in TRNSYS - a selection of version 16 features. Proceedings IBPSA (International Building Performance Simulation Association), World Conference, 2005.
9. Diersch, H.-J.G., Error norms used in FEFLOW. *FEFLOW's White Papers Vol. I*, Chapter 5, WASY GmbH, Berlin, 2002.
10. Diersch, H.-J.G., Discrete feature modeling of flow, mass and heat transport processes by using FEFLOW. *FEFLOW's White Papers Vol. I*, Chapter 9, WASY GmbH, Berlin, 2002.
11. Diersch, H.-J.G., Kolditz, O., Variable-density flow and transport in porous media: approaches and challenges. *Adv. Water Resour.* **25** (2002), 899-944.
12. Eskilson, P., Claesson, J., Simulation model for thermally interacting heat extraction boreholes. *Numerical Heat Transfer* **13** (1988), 149-165.
13. Hellström, G., *Ground heat storage. Thermal analyses of duct storage systems. I. Theory.* Dept. of Mathematical Physics. University of Lund, Sweden, 1991.
14. Ingersoll, L.R., Zobel, O.J. Ingersoll, A.C., *Heat conduction with engineering, geological, and other applications.* McGraw Hill, New York, 1948.
15. Nillert, P., Beitrag zur Simulation von Brunnen als innere Randbedingungen in horizontalebenen diskreten Grundwasserströmungsmodellen (simulation of wells as inner boundary conditions for horizontal 2D discrete groundwater flow models). Dissertation, Technical University Dresden, Germany, 1976.
16. Rieger, M., Saisonaler Erdsonden-Wärmespeicher in Crailsheim (seasonal BTES in Crailsheim, Germany). *bbr - Fachmagazin für Brunnen- und Leitungsbau* **9** (2008), 24-32.
17. TRNSYS, *A transient system simulation program*, Solar Energy Laboratory, University of Wisconsin, Madison and Transsolar, Stuttgart, 2000.
18. van Gelder, A.J. Geothermal response tests: the design and engineering of geothermal energy systems *Workshop Geothermal Response Tests* (École Polytechnique Fédérale Lausanne, Schweizerische Vereinigung für Geothermie SVG, Lausanne), ed. W. Eugster and L. Laloui, 2001, pp 64–75.
19. van Genuchten, M.Th., Alves, W.J., Analytical solutions of the one-dimensional convective-dispersive solute transport equation. Technical Bulletin Number 1661, US Dept. Agriculture, 1982, 149p.
20. VDI-Gesellschaft Energietechnik (Hrsg.), VDI-Richtlinien: Thermische Nutzung des Untergrundes - Erdgekoppelte Wärmepumpenanlagen (thermal use of the underground - ground source heat pump systems). VDI 4640 Part 2, Beuth Verlag GmbH, Berlin, 2001.
21. VDI-Gesellschaft Verfahrenstechnik und Chemieingenieurwesen (Hrsg.), VDI-Wärmeatlas: Wärmeübertragung bei der Strömung durch Rohre (heat transfer in flow through pipes). Springer, 10. Auflage, 2006.
22. Zienkiewicz, O.C., Taylor, R.L. *The finite element method. Volume 1*: The basis. 5th edition, Butterworth-Heinemann, Oxford, 2000.

Appendix A

Analytic evaluation of matrix elements for the 1D pipe element

We consider the following linear 2-node element *e* (see Fig. 1.37)

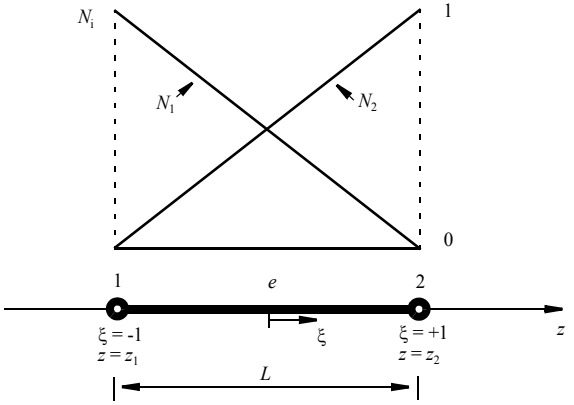

Figure 1.37 Shape functions of 1D element.

with the basis functions at the nodes 1 and 2

$$N_1 = \frac{1}{2}(1-\xi)$$
$$N_2 = \frac{1}{2}(1+\xi) \qquad \text{(A1)}$$

and their derivatives

$$\frac{\partial N_1}{\partial \xi} = -\frac{1}{2}$$
$$\frac{\partial N_2}{\partial \xi} = \frac{1}{2} \qquad \text{(A2)}$$

Furthermore, we have for the element

$$z = N_1 z_1 + N_2 z_2 \qquad \text{(A3)}$$

The Jacobian is given

$$\|J\| = \frac{\partial z}{\partial \xi} = \frac{\partial N_1}{\partial \xi} z_1 + \frac{\partial N_2}{\partial \xi} z_2 = \frac{L}{2} \qquad \text{(A4)}$$

and accordingly its inverse reads

$$J^{-1} = \frac{1}{\|J\|} = \frac{2}{L} \qquad \text{(A5)}$$

Then, the divergence terms appearing in (1-101a) to (1-101f) become with (A2)

$$\begin{bmatrix} \nabla N_1 \\ \nabla N_2 \end{bmatrix} = J^{-1} \begin{bmatrix} \frac{\partial N_1}{\partial \xi} \\ \frac{\partial N_2}{\partial \xi} \end{bmatrix} = \begin{bmatrix} -\frac{1}{L} \\ \frac{1}{L} \end{bmatrix} \qquad \text{(A6)}$$

For a 1D pipe element we have for the volume and surface element, respectively,

$$\left.\begin{aligned} d\Omega &= A\,dz = A\|J\|d\xi = \frac{AL}{2}d\xi \\ d\Gamma &= S\,dz = S\|J\|d\xi = \frac{SL}{2}d\xi \end{aligned}\right\} \qquad \text{(A7)}$$

where A is a cross-sectional area and S is the specific exchange surface given in (1-71). In case of 2U exchangers we will assume that the radii for the two pipes-in and two pipes-out are equal, i.e., we define $r_i^i = r_{i1}^i = r_{i2}^i$, $r_i^o = r_{i1}^o = r_{i2}^o$, $r_o^i = r_{o1}^i = r_{o2}^i$ and $r_o^o = r_{o1}^o = r_{o2}^o$. Accordingly, we find for cross-sectional areas A of the inner pipes and for the grout zones

(A8)

	2U	1U	CXA	CXC
A_i^i	$\pi(r_i^i)^2$	$\pi(r_i^i)^2$	$\pi[(r_i^i)^2-(r_o^o)^2]$	$\pi(r_i^i)^2$
A_o^i	$\pi(r_o^i)^2$	$\pi(r_o^i)^2$	$\pi(r_o^i)^2$	$\pi[(r_o^i)^2-(r_i^o)^2]$
A_g^i	$\pi\left[\frac{1}{4}\frac{D^2}{4}-(r_i^o)^2\right]$	$\pi\left[\frac{1}{2}\frac{D^2}{4}-(r_i^o)^2\right]$	$\pi\left[\frac{D^2}{4}-(r_i^o)^2\right]$	-
A_g^o	$\pi\left[\frac{1}{4}\frac{D^2}{4}-(r_o^o)^2\right]$	$\pi\left[\frac{1}{2}\frac{D^2}{4}-(r_o^o)^2\right]$	-	$\pi\left[\frac{D^2}{4}-(r_o^o)^2\right]$

In using these relationships the matrices (1-101a) to (1-101f) become for element e

$$\boldsymbol{o}_i^e = \int_{\Omega^e_{i1,i2}} \rho^r c^r \begin{bmatrix} N_1N_1 & N_1N_2 \\ N_2N_1 & N_2N_2 \end{bmatrix} d\Omega = \frac{\rho^r c^r}{4} \int_{-1}^{1} \begin{bmatrix} (1-\xi)^2 & (1-\xi^2) \\ (1-\xi^2) & (1+\xi)^2 \end{bmatrix} \frac{A_i^i L}{2} d\xi = \frac{A_i^i \rho^r c^r L}{6} \begin{bmatrix} 2 & 1 \\ 1 & 2 \end{bmatrix}$$

$$\boldsymbol{o}_o^e = \frac{A_o^i \rho^r c^r L}{6} \begin{bmatrix} 2 & 1 \\ 1 & 2 \end{bmatrix}$$

$$\boldsymbol{o}_{g1}^e = \int_{\Omega^e_{g1}} \varepsilon_g \rho^g c^g \begin{bmatrix} N_1N_1 & N_1N_2 \\ N_2N_1 & N_2N_2 \end{bmatrix} d\Omega = \frac{\varepsilon_g \rho^g c^g}{4} \int_{-1}^{1} \begin{bmatrix} (1-\xi)^2 & (1-\xi^2) \\ (1-\xi^2) & (1+\xi)^2 \end{bmatrix} \frac{A_g^i L}{2} d\xi = \frac{A_g^i \varepsilon_g \rho^g c^g L}{6} \begin{bmatrix} 2 & 1 \\ 1 & 2 \end{bmatrix}$$

$$\boldsymbol{o}_{g2}^e = \frac{A_g^i \varepsilon_g \rho^g c^g L}{6} \begin{bmatrix} 2 & 1 \\ 1 & 2 \end{bmatrix}$$

$$\boldsymbol{o}_{g3}^e = \int_{\Omega^e_{g3}} \varepsilon_g \rho^g c^g \begin{bmatrix} N_1N_1 & N_1N_2 \\ N_2N_1 & N_2N_2 \end{bmatrix} d\Omega = \frac{\varepsilon_g \rho^g c^g}{4} \int_{-1}^{1} \begin{bmatrix} (1-\xi)^2 & (1-\xi^2) \\ (1-\xi^2) & (1+\xi)^2 \end{bmatrix} \frac{A_g^o L}{2} d\xi = \frac{A_g^o \varepsilon_g \rho^g c^g L}{6} \begin{bmatrix} 2 & 1 \\ 1 & 2 \end{bmatrix}$$

$$\boldsymbol{o}_{g4}^e = \frac{A_g^o \varepsilon_g \rho^g c^g L}{6} \begin{bmatrix} 2 & 1 \\ 1 & 2 \end{bmatrix} \tag{A9}$$

$$\boldsymbol{c}_i^e = \boldsymbol{c}_{i,a}^e + \boldsymbol{c}_{i,d}^e$$

$$\boldsymbol{c}_{i,a}^e = \int_{\Omega^e_{i1,i2}} \rho^r c^r u \begin{bmatrix} N_1\nabla N_1 & N_1\nabla N_2 \\ N_2\nabla N_1 & N_2\nabla N_2 \end{bmatrix} d\Omega = \frac{\rho^r c^r u}{2L} \int_{-1}^{1} \begin{bmatrix} -(1-\xi) & (1-\xi) \\ -(1+\xi) & (1+\xi) \end{bmatrix} \frac{A_i^i L}{2} d\xi = \frac{A_i^i \rho^r c^r u}{2} \begin{bmatrix} -1 & 1 \\ -1 & 1 \end{bmatrix}$$

$$\boldsymbol{c}_{i,d}^e = \int_{\Omega^e_{i1,i2}} \Lambda^r \begin{bmatrix} \nabla N_1\nabla N_1 & \nabla N_1\nabla N_2 \\ \nabla N_2\nabla N_1 & \nabla N_2\nabla N_2 \end{bmatrix} d\Omega = \frac{\Lambda^r}{L^2} \int_{-1}^{1} \begin{bmatrix} 1 & -1 \\ -1 & 1 \end{bmatrix} \frac{A_i^i L}{2} d\xi = \frac{A_i^i \Lambda^r}{L} \begin{bmatrix} 1 & -1 \\ -1 & 1 \end{bmatrix} \tag{A10}$$

$$\boldsymbol{c}_o^e = \boldsymbol{c}_{o,a}^e + \boldsymbol{c}_{o,d}^e = \frac{A_o^i \rho^r c^r (-u)}{2} \begin{bmatrix} -1 & 1 \\ -1 & 1 \end{bmatrix} + \frac{A_o^i \Lambda^r}{L} \begin{bmatrix} 1 & -1 \\ -1 & 1 \end{bmatrix}$$

where $\Lambda^r = \left|\boldsymbol{\Lambda}^r\right|$.

$$
\begin{aligned}
\boldsymbol{R}_i^e &= -\Phi_{fig}\int_{\Gamma^e_{i1,i2}}\begin{bmatrix}N_1N_1 & N_1N_2\\ N_2N_1 & N_2N_2\end{bmatrix}d\Gamma = -\frac{\Phi_{fig}}{4}\int_{-1}^{1}\begin{bmatrix}(1-\xi)^2 & (1-\xi^2)\\ (1-\xi^2) & (1+\xi)^2\end{bmatrix}\frac{S_iL}{2}d\xi = -\frac{\Phi_{fig}S_iL}{6}\begin{bmatrix}2 & 1\\ 1 & 2\end{bmatrix}\\
\boldsymbol{R}_o^e &= -\Phi_{fog}\int_{\Gamma^e_{o1,o2}}\begin{bmatrix}N_1N_1 & N_1N_2\\ N_2N_1 & N_2N_2\end{bmatrix}d\Gamma = -\frac{\Phi_{fog}}{4}\int_{-1}^{1}\begin{bmatrix}(1-\xi)^2 & (1-\xi^2)\\ (1-\xi^2) & (1+\xi)^2\end{bmatrix}\frac{S_oL}{2}d\xi = -\frac{\Phi_{fog}S_oL}{6}\begin{bmatrix}2 & 1\\ 1 & 2\end{bmatrix}\\
\boldsymbol{R}_{io}^e &= -\Phi_{ff}\int_{\Gamma^e_{o1\cap i1}}\begin{bmatrix}N_1N_1 & N_1N_2\\ N_2N_1 & N_2N_2\end{bmatrix}d\Gamma = -\frac{\Phi_{ff}}{4}\int_{-1}^{1}\begin{bmatrix}(1-\xi)^2 & (1-\xi^2)\\ (1-\xi^2) & (1+\xi)^2\end{bmatrix}\frac{S_{io}L}{2}d\xi = -\frac{\Phi_{ff}S_{io}L}{6}\begin{bmatrix}2 & 1\\ 1 & 2\end{bmatrix}\\
\boldsymbol{R}_{g1}^e &= -\Phi_{gg1}\int_{\Gamma^e_{g1,g2,g3,g4}}\begin{bmatrix}N_1N_1 & N_1N_2\\ N_2N_1 & N_2N_2\end{bmatrix}d\Gamma = -\frac{\Phi_{gg1}}{4}\int_{-1}^{1}\begin{bmatrix}(1-\xi)^2 & (1-\xi^2)\\ (1-\xi^2) & (1+\xi)^2\end{bmatrix}\frac{S_{g1}L}{2}d\xi = -\frac{\Phi_{gg1}S_{g1}L}{6}\begin{bmatrix}2 & 1\\ 1 & 2\end{bmatrix}\\
\boldsymbol{R}_{g2}^e &= -\Phi_{gg2}\int_{\Gamma^e_{g1,g2,g3,g4}}\begin{bmatrix}N_1N_1 & N_1N_2\\ N_2N_1 & N_2N_2\end{bmatrix}d\Gamma = -\frac{\Phi_{gg2}}{4}\int_{-1}^{1}\begin{bmatrix}(1-\xi)^2 & (1-\xi^2)\\ (1-\xi^2) & (1+\xi)^2\end{bmatrix}\frac{S_{g2}L}{2}d\xi = -\frac{\Phi_{gg2}S_{g2}L}{6}\begin{bmatrix}2 & 1\\ 1 & 2\end{bmatrix}\\
\boldsymbol{R}_s^e &= -\Phi_{gs}\int_{\Gamma^e_{g1,g2,g3,g4}}\begin{bmatrix}N_1N_1 & N_1N_2\\ N_2N_1 & N_2N_2\end{bmatrix}d\Gamma = -\frac{\Phi_{gs}}{4}\int_{-1}^{1}\begin{bmatrix}(1-\xi)^2 & (1-\xi^2)\\ (1-\xi^2) & (1+\xi)^2\end{bmatrix}\frac{S_{gs}L}{2}d\xi = -\frac{\Phi_{gs}S_{gs}L}{6}\begin{bmatrix}2 & 1\\ 1 & 2\end{bmatrix}
\end{aligned}
\tag{A11}
$$

$$
\begin{aligned}
\boldsymbol{K}_{i1}^e &= \boldsymbol{C}_i^e - \boldsymbol{R}_i^e - \boldsymbol{R}_{io}^e = \frac{A_i^i\rho^r c^r u}{2}\begin{bmatrix}-1 & 1\\ -1 & 1\end{bmatrix} + \frac{A_i^i\Lambda^r}{L}\begin{bmatrix}1 & -1\\ -1 & 1\end{bmatrix} + \frac{(\Phi_{fig}S_i + \Phi_{ff}S_{io})L}{6}\begin{bmatrix}2 & 1\\ 1 & 2\end{bmatrix}\\
\boldsymbol{K}_{i2}^e &= \boldsymbol{C}_i^e - \boldsymbol{R}_i^e = \frac{A_i^i\rho^r c^r u}{2}\begin{bmatrix}-1 & 1\\ -1 & 1\end{bmatrix} + \frac{A_i^i\Lambda^r}{L}\begin{bmatrix}1 & -1\\ -1 & 1\end{bmatrix} + \frac{\Phi_{fig}S_iL}{6}\begin{bmatrix}2 & 1\\ 1 & 2\end{bmatrix}\\
\boldsymbol{K}_{o1}^e &= \boldsymbol{C}_o^e - \boldsymbol{R}_o^e - \boldsymbol{R}_{io}^e = \frac{A_o^i\rho^r c^r(-u)}{2}\begin{bmatrix}-1 & 1\\ -1 & 1\end{bmatrix} + \frac{A_o^i\Lambda^r}{L}\begin{bmatrix}1 & -1\\ -1 & 1\end{bmatrix} + \frac{(\Phi_{fog}S_o + \Phi_{ff}S_{io})L}{6}\begin{bmatrix}2 & 1\\ 1 & 2\end{bmatrix}\\
\boldsymbol{K}_{o2}^e &= \boldsymbol{C}_o^e - \boldsymbol{R}_o^e = \frac{A_o^i\rho^r c^r(-u)}{2}\begin{bmatrix}-1 & 1\\ -1 & 1\end{bmatrix} + \frac{A_o^i\Lambda^r}{L}\begin{bmatrix}1 & -1\\ -1 & 1\end{bmatrix} + \frac{\Phi_{fog}S_oL}{6}\begin{bmatrix}2 & 1\\ 1 & 2\end{bmatrix}\\
\boldsymbol{K}_{ig}^e &= \frac{A_g^i\varepsilon_g\lambda^g}{L}\begin{bmatrix}1 & -1\\ -1 & 1\end{bmatrix} + (\Phi_{fig}S_i + 2\Phi_{gg1}S_{g1} + \Phi_{gg2}S_{g2} + \Phi_{gs}S_{gs})\frac{L}{6}\begin{bmatrix}2 & 1\\ 1 & 2\end{bmatrix}\\
\boldsymbol{K}_{og}^e &= \frac{A_g^o\varepsilon_g\lambda^g}{L}\begin{bmatrix}1 & -1\\ -1 & 1\end{bmatrix} + (\Phi_{fog}S_o + 2\Phi_{gg1}S_{g1} + \Phi_{gg2}S_{g2} + \Phi_{gs}S_{gs})\frac{L}{6}\begin{bmatrix}2 & 1\\ 1 & 2\end{bmatrix}
\end{aligned}
\tag{A12}
$$

$$
\begin{aligned}
\boldsymbol{F}^e_{i1} &= \int_{\Omega^e_{i1}} H_{i1}\begin{bmatrix}N_1\\N_2\end{bmatrix}d\Omega = \frac{H_{i1}}{2}\int_{-1}^{1}\begin{bmatrix}(1-\xi)\\(1+\xi)\end{bmatrix}\frac{A^i_i L}{2}d\xi = \frac{A^i_i H_{i1} L}{2}\begin{bmatrix}1\\1\end{bmatrix}\\
\boldsymbol{F}^e_{i2} &= \int_{\Omega^e_{i2}} H_{i2}\begin{bmatrix}N_1\\N_2\end{bmatrix}d\Omega = \frac{H_{i2}}{2}\int_{-1}^{1}\begin{bmatrix}(1-\xi)\\(1+\xi)\end{bmatrix}\frac{A^i_i L}{2}d\xi = \frac{A^i_i H_{i2} L}{2}\begin{bmatrix}1\\1\end{bmatrix}\\
\boldsymbol{F}^e_{o1} &= \int_{\Omega^e_{o1}} H_{i1}\begin{bmatrix}N_1\\N_2\end{bmatrix}d\Omega = \frac{H_{o1}}{2}\int_{-1}^{1}\begin{bmatrix}(1-\xi)\\(1+\xi)\end{bmatrix}\frac{A^i_o L}{2}d\xi = \frac{A^i_o H_{o1} L}{2}\begin{bmatrix}1\\1\end{bmatrix}\\
\boldsymbol{F}^e_{o2} &= \int_{\Omega^e_{o2}} H_{o2}\begin{bmatrix}N_1\\N_2\end{bmatrix}d\Omega = \frac{H_{o2}}{2}\int_{-1}^{1}\begin{bmatrix}(1-\xi)\\(1+\xi)\end{bmatrix}\frac{A^i_o L}{2}d\xi = \frac{A^i_o H_{o2} L}{2}\begin{bmatrix}1\\1\end{bmatrix}\\
\boldsymbol{F}^e_{g1} &= \int_{\Omega^e_{g1}} H_{g1}\begin{bmatrix}N_1\\N_2\end{bmatrix}d\Omega = \frac{H_{g1}}{2}\int_{-1}^{1}\begin{bmatrix}(1-\xi)\\(1+\xi)\end{bmatrix}\frac{A^i_g L}{2}d\xi = \frac{A^i_g H_{g1} L}{2}\begin{bmatrix}1\\1\end{bmatrix}\\
\boldsymbol{F}^e_{g2} &= \int_{\Omega^e_{g2}} H_{g2}\begin{bmatrix}N_1\\N_2\end{bmatrix}d\Omega = \frac{H_{g2}}{2}\int_{-1}^{1}\begin{bmatrix}(1-\xi)\\(1+\xi)\end{bmatrix}\frac{A^i_g L}{2}d\xi = \frac{A^i_g H_{g2} L}{2}\begin{bmatrix}1\\1\end{bmatrix}\\
\boldsymbol{F}^e_{g3} &= \int_{\Omega^e_{g3}} H_{g3}\begin{bmatrix}N_1\\N_2\end{bmatrix}d\Omega = \frac{H_{g3}}{2}\int_{-1}^{1}\begin{bmatrix}(1-\xi)\\(1+\xi)\end{bmatrix}\frac{A^o_g L}{2}d\xi = \frac{A^o_g H_{g3} L}{2}\begin{bmatrix}1\\1\end{bmatrix}\\
\boldsymbol{F}^e_{g4} &= \int_{\Omega^e_{g4}} H_{g3}\begin{bmatrix}N_1\\N_2\end{bmatrix}d\Omega = \frac{H_{g4}}{2}\int_{-1}^{1}\begin{bmatrix}(1-\xi)\\(1+\xi)\end{bmatrix}\frac{A^o_g L}{2}d\xi = \frac{A^o_g H_{g4} L}{2}\begin{bmatrix}1\\1\end{bmatrix}
\end{aligned}
\tag{A13}
$$

Appendix B

Element matrices of the 1D-2U pipe element

The 1D 2U pipe element *e* consists of two nodes with each eight degrees of freedom (8-DOF) as shown in Fig. 1.38. Accordingly, the local element matrices yield following forms:

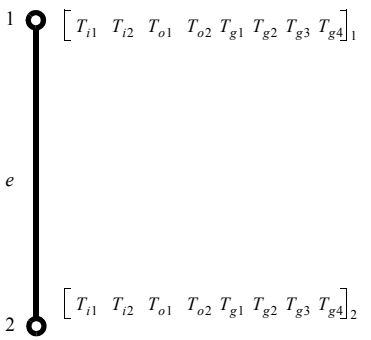

Figure 1.38 1D 2U 8-DOF element.

$$\boldsymbol{O}^e = \begin{bmatrix} \boldsymbol{O}_i^e & 0 & 0 & 0 & 0 & 0 & 0 & 0 \\ 0 & \boldsymbol{O}_i^e & 0 & 0 & 0 & 0 & 0 & 0 \\ 0 & 0 & \boldsymbol{O}_o^e & 0 & 0 & 0 & 0 & 0 \\ 0 & 0 & 0 & \boldsymbol{O}_o^e & 0 & 0 & 0 & 0 \\ 0 & 0 & 0 & 0 & \boldsymbol{O}_{g1}^e & 0 & 0 & 0 \\ 0 & 0 & 0 & 0 & 0 & \boldsymbol{O}_{g2}^e & 0 & 0 \\ 0 & 0 & 0 & 0 & 0 & 0 & \boldsymbol{O}_{g3}^e & 0 \\ 0 & 0 & 0 & 0 & 0 & 0 & 0 & \boldsymbol{O}_{g4}^e \end{bmatrix}$$

$$= \begin{array}{c} \\ \\ (1) \\ \\ \\ \\ \\ \\ \\ (2) \\ \\ \\ \\ \\ \\ \\ \end{array} \begin{array}{c} \begin{array}{cccccccc} \multicolumn{8}{c}{(1)} & \multicolumn{8}{c}{(2)} \end{array} \\ \begin{array}{cccccccc} i1 & i2 & o1 & o2 & g1 & g2 & g3 & g4 \end{array} \\ \begin{bmatrix} O_i^{11} & 0 & 0 & 0 & 0 & 0 & 0 & 0 \\ 0 & O_i^{11} & 0 & 0 & 0 & 0 & 0 & 0 \\ 0 & 0 & O_o^{11} & 0 & 0 & 0 & 0 & 0 \\ 0 & 0 & 0 & O_o^{11} & 0 & 0 & 0 & 0 \\ 0 & 0 & 0 & 0 & O_{g1}^{11} & 0 & 0 & 0 \\ 0 & 0 & 0 & 0 & 0 & O_{g2}^{11} & 0 & 0 \\ 0 & 0 & 0 & 0 & 0 & 0 & O_{g3}^{11} & 0 \\ 0 & 0 & 0 & 0 & 0 & 0 & 0 & O_{g4}^{11} \end{bmatrix} \begin{bmatrix} O_i^{12} & 0 & 0 & 0 & 0 & 0 & 0 & 0 \\ 0 & O_i^{12} & 0 & 0 & 0 & 0 & 0 & 0 \\ 0 & 0 & O_o^{12} & 0 & 0 & 0 & 0 & 0 \\ 0 & 0 & 0 & O_o^{12} & 0 & 0 & 0 & 0 \\ 0 & 0 & 0 & 0 & O_{g1}^{12} & 0 & 0 & 0 \\ 0 & 0 & 0 & 0 & 0 & O_{g2}^{12} & 0 & 0 \\ 0 & 0 & 0 & 0 & 0 & 0 & O_{g3}^{12} & 0 \\ 0 & 0 & 0 & 0 & 0 & 0 & 0 & O_{g4}^{12} \end{bmatrix} \\ \begin{bmatrix} O_i^{21} & 0 & 0 & 0 & 0 & 0 & 0 & 0 \\ 0 & O_i^{21} & 0 & 0 & 0 & 0 & 0 & 0 \\ 0 & 0 & O_o^{21} & 0 & 0 & 0 & 0 & 0 \\ 0 & 0 & 0 & O_o^{21} & 0 & 0 & 0 & 0 \\ 0 & 0 & 0 & 0 & O_{g1}^{21} & 0 & 0 & 0 \\ 0 & 0 & 0 & 0 & 0 & O_{g2}^{21} & 0 & 0 \\ 0 & 0 & 0 & 0 & 0 & 0 & O_{g3}^{21} & 0 \\ 0 & 0 & 0 & 0 & 0 & 0 & 0 & O_{g4}^{21} \end{bmatrix} \begin{bmatrix} O_i^{22} & 0 & 0 & 0 & 0 & 0 & 0 & 0 \\ 0 & O_i^{22} & 0 & 0 & 0 & 0 & 0 & 0 \\ 0 & 0 & O_o^{22} & 0 & 0 & 0 & 0 & 0 \\ 0 & 0 & 0 & O_o^{22} & 0 & 0 & 0 & 0 \\ 0 & 0 & 0 & 0 & O_{g1}^{22} & 0 & 0 & 0 \\ 0 & 0 & 0 & 0 & 0 & O_{g2}^{22} & 0 & 0 \\ 0 & 0 & 0 & 0 & 0 & 0 & O_{g3}^{22} & 0 \\ 0 & 0 & 0 & 0 & 0 & 0 & 0 & O_{g4}^{22} \end{bmatrix} \end{array} \quad \text{(B1)}$$

$$\boldsymbol{D}^e = \begin{bmatrix} \boldsymbol{K}^e_{i1} & 0 & \boldsymbol{R}^e_{io} & 0 & \boldsymbol{R}^e_{i} & 0 & 0 & 0 \\ 0 & \boldsymbol{K}^e_{i2} & 0 & 0 & 0 & \boldsymbol{R}^e_{i} & 0 & 0 \\ \boldsymbol{R}^e_{io} & 0 & \boldsymbol{K}^e_{o1} & 0 & 0 & 0 & \boldsymbol{R}^e_{o} & 0 \\ 0 & 0 & 0 & \boldsymbol{K}^e_{o2} & 0 & 0 & 0 & \boldsymbol{R}^e_{o} \\ \boldsymbol{R}^e_{i} & 0 & 0 & 0 & \boldsymbol{K}^e_{ig} & \boldsymbol{R}^e_{g2} & \boldsymbol{R}^e_{g1} & \boldsymbol{R}^e_{g1} \\ 0 & \boldsymbol{R}^e_{i} & 0 & 0 & \boldsymbol{R}^e_{g2} & \boldsymbol{K}^e_{ig} & \boldsymbol{R}^e_{g1} & \boldsymbol{R}^e_{g1} \\ 0 & 0 & \boldsymbol{R}^e_{o} & 0 & \boldsymbol{R}^e_{g1} & \boldsymbol{R}^e_{g1} & \boldsymbol{K}^e_{og} & \boldsymbol{R}^e_{g2} \\ 0 & 0 & 0 & \boldsymbol{R}^e_{o} & \boldsymbol{R}^e_{g1} & \boldsymbol{R}^e_{g1} & \boldsymbol{R}^e_{g2} & \boldsymbol{K}^e_{og} \end{bmatrix}$$

(1) (2)

$$= \begin{array}{c} \\ \\ (1) \\ \\ \\ \\ \\ \\ \\ (2) \\ \\ \\ \\ \\ \\ \\ \end{array} \begin{array}{c} \begin{array}{cccccccc} i1 & i2 & o1 & o2 & g1 & g2 & g3 & g4 \end{array} \\ \begin{bmatrix} K^{11}_{i1} & 0 & R^{11}_{io} & 0 & R^{11}_{i} & 0 & 0 & 0 \\ 0 & K^{11}_{i2} & 0 & 0 & 0 & R^{11}_{i} & 0 & 0 \\ R^{11}_{io} & 0 & K^{11}_{o1} & 0 & 0 & 0 & R^{11}_{o} & 0 \\ 0 & 0 & 0 & K^{11}_{o2} & 0 & 0 & 0 & R^{11}_{o} \\ R^{11}_{i} & 0 & 0 & 0 & K^{11}_{ig} & R^{11}_{g2} & R^{11}_{g1} & R^{11}_{g1} \\ 0 & R^{11}_{i} & 0 & 0 & R^{11}_{g2} & K^{11}_{ig} & R^{11}_{g1} & R^{11}_{g1} \\ 0 & 0 & R^{11}_{o} & 0 & R^{11}_{g1} & R^{11}_{g1} & K^{11}_{og} & R^{11}_{g2} \\ 0 & 0 & 0 & R^{11}_{o} & R^{11}_{g1} & R^{11}_{g1} & R^{11}_{g2} & K^{11}_{og} \end{bmatrix} \\ \begin{bmatrix} K^{21}_{i1} & 0 & R^{21}_{io} & 0 & R^{21}_{i} & 0 & 0 & 0 \\ 0 & K^{21}_{i2} & 0 & 0 & 0 & R^{21}_{i} & 0 & 0 \\ R^{21}_{io} & 0 & K^{21}_{o1} & 0 & 0 & 0 & R^{21}_{o} & 0 \\ 0 & 0 & 0 & K^{21}_{o2} & 0 & 0 & 0 & R^{21}_{o} \\ R^{21}_{i} & 0 & 0 & 0 & K^{21}_{ig} & R^{21}_{g2} & R^{21}_{g1} & R^{21}_{g1} \\ 0 & R^{21}_{i} & 0 & 0 & R^{21}_{g2} & K^{21}_{ig} & R^{21}_{g1} & R^{21}_{g1} \\ 0 & 0 & R^{21}_{o} & 0 & R^{21}_{g1} & R^{21}_{g1} & K^{21}_{og} & R^{21}_{g2} \\ 0 & 0 & 0 & R^{21}_{o} & R^{21}_{g1} & R^{21}_{g1} & R^{21}_{g2} & K^{21}_{og} \end{bmatrix} \end{array} \begin{array}{c} \begin{array}{cccccccc} i1 & i2 & o1 & o2 & g1 & g2 & g3 & g4 \end{array} \\ \begin{bmatrix} K^{12}_{i1} & 0 & R^{12}_{io} & 0 & R^{12}_{i} & 0 & 0 & 0 \\ 0 & K^{12}_{i2} & 0 & 0 & 0 & R^{12}_{i} & 0 & 0 \\ R^{12}_{io} & 0 & K^{12}_{o1} & 0 & 0 & 0 & R^{12}_{o} & 0 \\ 0 & 0 & 0 & K^{12}_{o2} & 0 & 0 & 0 & R^{12}_{o} \\ R^{12}_{i} & 0 & 0 & 0 & K^{12}_{ig} & R^{12}_{g2} & R^{12}_{g1} & R^{12}_{g1} \\ 0 & R^{12}_{i} & 0 & 0 & R^{12}_{g2} & K^{12}_{ig} & R^{12}_{g1} & R^{12}_{g1} \\ 0 & 0 & R^{12}_{o} & 0 & R^{12}_{g1} & R^{12}_{g1} & K^{12}_{og} & R^{12}_{g2} \\ 0 & 0 & 0 & R^{12}_{o} & R^{12}_{g1} & R^{12}_{g1} & R^{12}_{g2} & K^{12}_{og} \end{bmatrix} \\ \begin{bmatrix} K^{22}_{i1} & 0 & R^{22}_{io} & 0 & R^{22}_{i} & 0 & 0 & 0 \\ 0 & K^{22}_{i2} & 0 & 0 & 0 & R^{22}_{i} & 0 & 0 \\ R^{22}_{io} & 0 & K^{22}_{o1} & 0 & 0 & 0 & R^{22}_{o} & 0 \\ 0 & 0 & 0 & K^{22}_{o2} & 0 & 0 & 0 & R^{22}_{o} \\ R^{22}_{i} & 0 & 0 & 0 & K^{22}_{ig} & R^{22}_{g2} & R^{22}_{g1} & R^{22}_{g1} \\ 0 & R^{22}_{i} & 0 & 0 & R^{22}_{g2} & K^{22}_{ig} & R^{22}_{g1} & R^{22}_{g1} \\ 0 & 0 & R^{22}_{o} & 0 & R^{22}_{g1} & R^{22}_{g1} & K^{22}_{og} & R^{22}_{g2} \\ 0 & 0 & 0 & R^{22}_{o} & R^{22}_{g1} & R^{22}_{g1} & R^{22}_{g2} & K^{22}_{og} \end{bmatrix} \end{array} \tag{B2}$$

where the coefficients of the element submatrices $\boldsymbol{O}_i^e = \begin{bmatrix} O_i^{11} & O_i^{12} \\ O_i^{21} & O_i^{22} \end{bmatrix}$, $\boldsymbol{K}_{i1}^e = \begin{bmatrix} K_{i1}^{11} & K_{i1}^{12} \\ K_{i1}^{21} & K_{i1}^{22} \end{bmatrix}$, $\boldsymbol{R}_i^e = \begin{bmatrix} R_i^{11} & R_i^{12} \\ R_i^{21} & R_i^{22} \end{bmatrix}$ *etc.* are given from the expressions (A9) to (A13).

The remaining part of the $\boldsymbol{R}_s$ matrix has to be assembled for each element *e* linked to the corresponding soil nodes *s*. Such type of element also consists of two nodes but with only one degree of freedom (1-DOF) as shown in Fig. 1.39.

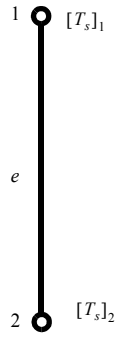

Figure 1.39 1D $\boldsymbol{R}_s^e$ 1-DOF element.

The local element matrix $\boldsymbol{R}_s^e$ reads simply

$$\boldsymbol{R}_s^e = \begin{bmatrix} R_s^{11} & R_s^{12} \\ R_s^{21} & R_s^{22} \end{bmatrix} \tag{B3}$$

determined from (A11).

Appendix C

Nomenclature

Roman letters

A	L^2	cross-sectional area;
b	L	pipe wall thickness;
c	$L^2T^{-2}\Theta^{-1}$	specific heat capacity;
D	L	borehole diameter;
D	L^2T^{-1}	thermal diffusivity;
D^i	L	inner diameter of pipe;
d	L	pipe diameter;
$\boldsymbol{e}$	1	$= -\boldsymbol{g}/\lvert\boldsymbol{g}\rvert$, gravitational unit vector;
f_μ	1	viscosity relation function;
G	1	number of grout zones;
$\boldsymbol{g}$	LT^{-2}	gravity vector;
g	LT^{-2}	$= \lvert\boldsymbol{g}\rvert$, gravitational acceleration;
H	$ML^{-1}T^{-3}$	thermal sink/source term;
h	L	hydraulic head;
$\boldsymbol{I}$	1	unit (identity) matrix;
$\boldsymbol{J}$	L	Jacobian matrix;
$\boldsymbol{K}$	LT^{-1}	hydraulic conductivity tensor;
K		number of soil-pipe nodes;
L	L	length of 1D pipe element;
$\bar{L}$	L	length of pipe, depth of borehole;
L_p		error norm specifier, $p \geq 1$;
$\boldsymbol{N}$	1	shape function vector;
N		number of soil *s* nodes;
Nu	1	Nusselt number;
$\boldsymbol{n}$	1	normal unit vector (positive outward);
Pr	1	Prandtl number;
Q	T^{-1}	flow supply;

Q_b	L^3T^{-1}	pumping rate of well;
Q_h	ML^2T^{-3}	total heat input rate of BHE;
Q_r	L^3T^{-1}	total refrigerant flow discharge of BHE;
$\boldsymbol{q}$	LT^{-1}	vector of volumetric Darcy flux of fluid;
$\boldsymbol{q}_{nT_s}$	MT^{-3}	normal heat flux of soil (positive outward);
R	$M^{-1}L^{-1}T^3\Theta$	thermal resistance;
R_a, R_b	$M^{-1}L^{-1}T^3\Theta$	borehole thermal resistances;
$\Re$		space of matrix;
Re	1	Reynolds number;
r	L	radius;
S	L	specific exchange surface;
S_s	L^{-1}	storage coefficient;
s	L	diagonal pipe distance;
T	Θ	temperature;
T_i	Θ	pipe inlet temperature of refrigerant;
T_o	Θ	pipe outlet temperature of refrigerant;
t	T	time;
$\boldsymbol{u}$	LT^{-1}	vector of refrigerant fluid velocity;
u	LT^{-1}	$= \lvert\boldsymbol{u}\rvert$ refrigerant fluid velocity;
v	LT^{-1}	auxiliary velocity variable;
w	1	spatial weighting function;
w	L	pipe distance;
$\boldsymbol{x}$	L	Eulerian spatial coordinates;
x, y, z	L	Cartesian coordinates;
x^k	1	scaler for thermal resistance of pipe k;
z	L	vertical coordinate;

Greek letters

α_L, α_T	L	longitudinal and transverse thermo-dispersivity, respectively;
α_L^{num}	L	numerical thermo-dispersivity in longitudinal flow direction;
β	Θ^{-1}	thermal expansion coefficient;
Γ		boundary;
γ_k	1	weighting coefficient of pipe k;
Δ	L	BHE nodal distance;
δ	1	error tolerance;
$\delta(\ )$	L^{-3}	Dirac delta function;
ε	1	volume fraction, porosity;
θ	1	weighting coefficient;
κ	1	upwind parameter;
$\boldsymbol{\Lambda}$	$MLT^{-3}\Theta^{-1}$	tensor of thermal hydrodynamic dispersion;
$\boldsymbol{\Lambda}^r$	$MLT^{-3}\Theta^{-1}$	tensor of thermal hydrodynamic dispersion for refrigerant;
λ	$MLT^{-3}\Theta^{-1}$	thermal conductivity;
μ	$ML^{-1}T^{-1}$	dynamic viscosity of fluid;
ξ_k	1	auxiliary variable for pipe k;
ρ	ML^{-3}	fluid density;
τ		iteration number;
Υ_l		mesh refinement at level l;
Φ	$MT^{-3}\Theta^{-1}$	heat transfer coefficient;
ϕ	T^{-1}	specific heat transfer coefficient;
φ	MLT^{-3}	specific thermal flux;
Ω		domain;
∇	L^{-1}	Nabla (vector) operator;

Subscripts

b	borehole, well;
EOB	extended Oberbeck-Boussinesq approximation;
g	grout;
i	pipe-in or internal;

k	pipe index;
n	time plane;
o	pipe-out or outer;
p	pipe;
s	soil;

Superscripts

CXA	coaxial pipe with annular inlet;
CXC	coaxial pipe with centred inlet;
i	internal;
e	element;
f	fluid;
g	grout;
k	pipe index;
l	refinement level;
n	time plane;
o	outer;
p	pipe;
R	boundary;
r	refrigerant;
s	solid or soil;
T	transpose;
1U	single U-shape pipe;
2U	double U-shape pipe;

Abbreviations

BC	boundary condition;
BE	backward Euler scheme;
BHE	borehole heat exchanger;
BTES	borehole thermal energy store(s);
CXA	coaxial pipe with annular inlet;
CXC	coaxial pipe with centred inlet;
DOF	degrees of freedom;
FD3DM	fully discretized 3D model;
FEFLOW	finite element flow simulator;
FEM	finite element method;
IFM	interface manager;
NE	number of elements;
NP	number of points (nodes);
NS	number of slices;
RHS	right-hand side;
RMS	root mean square;
RPC	remote procedure protocol;
TR	trapezoid rule scheme;
TRNSYS	energy simulation program;
1U	single U-shape pipe;
1D	one-dimensional;
2U	double U-shape pipe;
3D	three-dimensional;

2 Derivation of the coefficients of compressibility, thermal expansion and fluid density difference ratio for reproducing aqueous NaCl density

F. Magri

Free University of Berlin, Department of Hydrogeology, Berlin, Germany

2.1 Equations and Variable Definitions

Fluid density ρ^f varies as a function of pressure p, temperature T and concentration C of dissolved components. In FEFLOW ρ^f is usually approximated by a linear form according to the following Equation of State (EOS)[2]:

$$\rho^f = \rho_o^f\left(1+\bar{\gamma}(p-p_o)-\bar{\beta}(T-T_o)+\frac{\bar{\alpha}}{(C_s-C_o)}(C-C_o)\right) \quad (2\text{-}1)$$

where

$$\bar{\gamma} = \frac{1}{\rho_o^f}\frac{\partial\rho^f}{\partial p}\bigg|_{T,C} \quad (2\text{-}2)$$

is the coefficient of compressibility of the fluid at constant temperature and concentration,

$$\bar{\beta} = \frac{1}{\rho_o^f}\frac{\partial\rho^f}{\partial T}\bigg|_{p,C} \quad (2\text{-}3)$$

is the coefficient of thermal expansion at constant pressure and concentration, and

$$\bar{\alpha}/(C_s-C_o) = \frac{1}{\rho_o^f}\frac{\partial\rho^f}{\partial C}\bigg|_{p,T} \quad (2\text{-}4)$$

introduces the effect of a density change due to the concentration of a dissolved component at constant pressure and temperature.

The fluid density ρ^f is equal to a reference density ρ_o^f when $T = T_o$, $p = p_o$ and $C = C_o$ that is when T, p and C are respectively equal to the reference temperature T_o, reference pressure p_o and reference concentration C_o. For instance, at p_o = 100 kPa, T_o = 0 °C and C_o = 0 mg/l, (2-1) becomes:

$$\rho^f(p,T,C) = \rho_o^f\left(1+\bar{\gamma}(p-100)-\bar{\beta}T+\frac{\bar{\alpha}}{C_s}C\right) \quad (2\text{-}5)$$

with $\rho^f = 998.8396\ [\mathrm{kg\ m^{-3}}]$ for water.

When modeling geothermal systems, wide ranges of pressure, temperature and concentration require that the coefficients $\bar{\alpha}, \bar{\beta}, \bar{\gamma}$ vary as function of p, T and C in order to correctly reproduce variable fluid density.

2.2 Data and Polynomial Equations

Brines are considered in the single liquid phase within the range (2-6).

Here the coefficients $\bar{\alpha}, \bar{\beta}, \bar{\gamma}$ are derived for reproducing the fluid density of aqueous sodium chloride solution (brine) in the single liquid phase within the following ranges:

$$\begin{aligned} 0.1 \le p \le 100\ \mathrm{MPa} \\ 0 \le T \le 300\ ^\circ\mathrm{C} \\ 0 \le C \le 350\ \mathrm{g\ l^{-1}} \end{aligned} \tag{2-6}$$

These coefficients are of big use for the modeling of geothermal systems in which groundwater solutions are assumed to be brines. Furthermore, they can easily be implemented in FEFLOW via the IFM (see Chapter 2.3).

2.2.1 Data

Brine density values for different pressure, temperature and concentration have been derived by using the theoretical approach of Pitzer[4] and Archer[1]. The resolution of the data has been set to 10 °C, 100 kPa and 7 g/l. When a (p, T, C) combination did not belong to the single fluid phase, the density values were systematically excluded from the database table. In total 159,423 densities values of the aqueous NaCl solution were generated in a $p - T - C$ grid and used for the polynomial regression fit.

2.2.2 Polynomial fit

The following expression provides an approximation with an accuracy of 0.5% for ρ^f in single liquid phase in the above mentioned range. This accuracy is good enough for simulating hydrothermal processes (*cf.* Driesner[3]):

$$\begin{aligned} \rho^f(p, T, C) &= 999.843633188666 - 100^2 q_2 \\ &- 100 q_1 + (q_2 p^2 + q_1 p) + z(p, C) T^6 + \\ &w(p, C) T^5 + v(p, C) T^4 + u(p, C) T^3 + \\ &s(p, C) T^2 + r(p, C) T + (j_0 + j_1 p + j_2 p^2) C^2 + \\ &(h_0 + h_1 p + h_2 p^2) C \end{aligned} \tag{2-7}$$

where

$$\begin{aligned} z(p, T, C) &= z_0 + z_1 p + z_2 p^2 + z_3 C + z_4 C^2 \\ w(p, T, C) &= w_0 + w_1 p + w_2 p^2 + w_3 C + w_4 C^2 \\ v(p, T, C) &= v_0 + v_1 p + v_2 p^2 + v_3 C + v_4 C^2 \\ u(p, T, C) &= u_0 + u_1 p + u_2 p^2 + u_3 C + u_4 C^2 \\ s(p, T, C) &= s_0 + s_1 p + s_2 p^2 + s_3 C + s_4 C^2 \\ r(p, T, C) &= r_0 + r_1 p + r_2 p^2 + r_3 C + r_4 C^2 \end{aligned} \tag{2-8}$$

with pressure p in kPa, temperature T in $^\circ$C, and C in mg/l. The calculated coefficients are listed in Tab. 2.1. The coefficients in Tab. 2.1 have been derived account-

ing for freshwater reference condition (i.e., $C = C_o = 0$ mg/l), at $p_o = 100$ kPa and $T_o = 0$ °C. For these reference values (2-7) gives:

$$\rho^f(100, 0, 0) = \rho_o^f = 998.8396 \text{ [kg m}^{-3}\text{]} \qquad (2\text{-}9)$$

Table 2.1 Coefficients of the polynomial fits as expressed in (2-7) and (2-8)

h_0	0.00073104758291628
h_1	-9.422037142360847E-10
h_2	1.821338928754865E-15
j_0	-3.9446778202994974E-10
j_1	7.533778133432179E-16
j_2	-2.3273323084072923E-22
q_1	0.0005257539357631474
q_2	-5.459359007740163E-10
z_0	-6.625358276579406E-13
z_1	6.3111586728429706E-18
z_2	2.744492639329977E-23
z_3	7.513091563357645E-18
z_4	-1.8936376378424672E-23
w_0	5.718374379180737E-10
w_1	-4.996112674640022E-15
w_2	-2.5570358684616452E-20
w_3	-6.483691625807997E-15

Table 2.1 Coefficients of the polynomial fits as expressed in (2-7) and (2-8) (cont.)

w_4	-5.310521468059033E-18
v_0	-2.051960478431085E-7
v_1	1.58244686429457E-12
v_2	8.637135897998724E-18
v_3	2.1946081669958214E-12
v_4	-5.310521468059033E-18
u_4	8.576370648910509E-16
u_3	-3.7575488991610133E-10
u_2	-1.4036263958416905E-15
u_1	-2.4220044746230556E-10
u_0	0.00003936397979529357
s_4	-7.725866104001761E-14
s_3	3.9534845368831494E-8
s_2	1.0032350032434767E-13
s_1	2.5442857110623736E-8
s_0	-0.0063083048607919245
r_4	3.6418368120766765E-12
r_3	-2.390003668646296E-6
r_2	-3.6928765749684625E-12
r_1	-1.155475728462599E-6
r_0	-0.04949178536220616

2. Derivation of the coefficients of compressibility, thermal expansion and fluid density difference ratio for reproducing aqueous NaCl density

The goal is to find the variable fluid density ratio $\bar{\alpha}$, the fluid compressibility $\bar{\gamma}$, and the coefficient of thermal expansion $\bar{\beta}$ of the fluid density function (2-5). To do that, we consider a Taylor series expansion for the fluid density $\rho^f(p, T, C)$ expressed in (2-7) around $T_o = 0$, $p_o = 100$ and $C_o = 0$, where a 6th order approximation is used for temperature T and a 2nd order approximation is used for both pressure p and concentration C dependences, *viz.*,

$$\begin{aligned}\rho^f(p,T,C) &= 999.843633188666 + \\ &(p-100)(q_1+200q_2+T(r_1+200r_2)+T^2(s_1+200s_s)+T^3(u_1+200u_2)+T^4(v_1+200v_2)+T^5(w_1+200w_2)+T^6(z_1+200z_2))+\\ &(p-100)^2(q_2+Tr_2+T^2s_2+T^3u_2+T^4v_2+T^5w_2+T^6z_2)+\\ &T(r_0+100r_1+100^2r_2)+T^2(s_0+100s_1+100^2s_2)+T^3(u_0+100u_1+100^2u_2)+T^4(v_0+100v_1+100^2v_2)+\\ &T^5(w_0+100w_1+100^2w_2)+T^6(z_0+100z_1+100^2z_2)+\\ &C(h_0+h_2(p-100)^2+100h_1+100^2h_2+(p-100)(h_1+200h_2)+Tr_3+T^2s_3+T^3u_3+T^4v_3+T^5w_3+T^6z_3)+\\ &C^2(j_0+j_2(p-p_o)^2+100j_1+100^2j_2+(p-100)(j_1+200j_2)+Tr_4+T^2s_4+T^3u_4+T^4v_4+T^5w_4+T^6z_4)\end{aligned} \tag{2-10}$$

Comparing the above equation with the EOS for the fluid density (2-5) and reminding that $\rho_o^f = 998.8396\ [\mathrm{kg\,m^{-3}}]$, we obtain the expression for $\bar{\alpha}(p, T, C)$, $\bar{\beta}(p, T, C)$ and $\bar{\gamma}(p, T, C)$ used in (2-1):

$$\begin{aligned}\bar{\gamma} = \frac{1}{999.843633188666}&[q_1+200q_2+T(r_1+200r_2)+T^2(s_1+200s_s)+T^3(u_1+200u_2)+T^4(v_1+200v_2)+T^5(w_1+200w_2)+T^6(z_1+200z_2)+\\ &(p-100)(q_2+Tr_2+T^2s_2+T^3u_2+T^4v_2+T^5w_2+T^6z_2)]\end{aligned} \tag{2-11}$$

$$\begin{aligned}\bar{\beta} = \frac{1}{999.843633188666}&[(r_0+100r_1+100^2r_2)+T(s_0+100s_1+100^2s_2)+T^2(u_0+100u_1+100^2u_2)+T^3(v_0+100v_1+100^2v_2)+\\ &T^4(w_0+100w_1+100^2w_2)+T^5(z_0+100z_1+100^2z_2)]\end{aligned} \tag{2-12}$$

$$\begin{aligned}\bar{\alpha} = \frac{C_s}{999.843633188666}&[h_0+h_2(p-100)^2+100h_1+100^2h_2+(p-100)(h_1+200h_2)+Tr_3+T^2s_3+T^3u_3+T^4v_3+T^5w_3+T^6z_3+\\ &C(j_0+j_2(p-p_o)^2+100j_1+100^2j_2+(p-100)(j_1+200j_2)+Tr_4+T^2s_4+T^3u_4+T^4v_4+T^5w_4+T^6z_4)]\end{aligned} \tag{2-13}$$

where all coefficients are listed in Tab. 2.1. In the next section, the IFM source code allowing implementing these coefficients into FEFLOW is given.

$$\rho^f(p,T,C) = \rho_o^f\left(1+\bar{\gamma}(p-p_o)-\bar{\beta}T+\frac{\bar{\alpha}}{C_s}C\right) \tag{2-14}$$

where $\bar{\gamma}$, $\bar{\beta}$, $\bar{\alpha}$ expressed by (2-11), (2-12), (2-13), and $\rho_o^f = \rho^f(100, 0, 0) = 998.8396\ [\mathrm{kg\,m^{-3}}]$, i.e., the reference pressure, reference temperature and reference concentration are $p_o = 100$ kPa, $T_o = 0\,^\circ$C, and $C_o = 0$ mg/l, respectively. We remind that in

2.3 Implementation

Our goal is to incorporate in FEFLOW the following EOS

FEFLOW the following EOS for the fluid density is already incorporated:

$$\rho^f(p, T, C) = \rho_o^f\left(1 - \bar{\beta}(T - T_o) + \frac{\bar{\alpha}}{C_s - C_o}(C - C_o)\right) \quad (2\text{-}15)$$

where $\bar{\beta}$ and $\bar{\alpha}$ are defined by the user.

2.3.1 How to implement the extended EOS?

The implementation of $\bar{\beta}$ and $\bar{\alpha}$ can be done directly by the use of FEFLOW's IFM programming interface through the API `IfmSetMatFlowExpansionCoeff()` and `IfmSetMatFlowDensityRatio()`. On the other hand, no related API interface exists for the coefficient of compressibility $\bar{\gamma}$. To make up for this lack, we have to use a little trick. Let's consider the EOS for the fluid density that we want to incorporate into FEFLOW Eq.(2-1) and apply a simple factorization in the following way:

$$\begin{aligned}\rho^f(p, T, C) &= \rho_o^f\left(1 + \bar{\gamma}(p - p_o) - \bar{\beta}T + \frac{\bar{\alpha}}{C_s}C\right) \\ &= \rho_o^f\left[1 - \left(\bar{\beta} - \bar{\gamma}\frac{(p - p_o)}{T}\right)T + \frac{\bar{\alpha}}{C_s}C\right] \quad (2\text{-}16) \\ &= \rho_o^f\left[1 - \bar{\beta}^* T + \frac{\bar{\alpha}}{C_s}C\right]\end{aligned}$$

with

$$\underbrace{\bar{\beta}^*}_{\substack{\text{defined as BETASTAR}\\ \text{in the source code}}} = \left(\underbrace{\bar{\beta}}_{\substack{\text{defined as BETA}\\ \text{in the source code}}} + \underbrace{-\bar{\gamma}\frac{(p - p_o)}{T}}_{\substack{\text{defined as GAMMASTAR}\\ \text{in the source code}}}\right) T \neq T_o \quad (2\text{-}17)$$

and $\bar{\gamma}$, $\bar{\beta}$ expressed in (2-11) and (2-12), respectively.

In this way, the effects due to the compressibility on the brine density are implicitly expressed in the new variable $\bar{\beta}^*$, which can then be implemented into FEFLOW by use of the API `IfmSetMatFlowExpansionCoeff()`.

2.3.2 Description of the source code `brine_dens.c`

The input data required are the pressure p, the temperature T, and the concentration C for each element of the FE mesh. These values can be retrieved by the use of the API functions `IfmGetResultsFlowPressureValue()`, `IfmGetResultsTransportHeatValue()`, and `IfmGetResultsTransportMassValue()`, which respectively load the nodal values of the pressure (kPa), temperature (°C) and concentration (mg/l) calculated during the simulations. Once the mean values of these parameters are calculated, they can be used as input for calculating, $\bar{\beta}^*$ and $\bar{\alpha}$ by use of the polynomial fit (Eqs. (2-11), (2-12), (2-13)).

The returned values are then stored into the API functions `IfmSetMatFlowExpansionCoeff()` and `IfmSetMatFlowExpansionCoeff()`. The complete source code `brine_dens.c` is listed below. The code is programmed in C++ language

through the IFM tool in the `Simulation` interface under the callback function `PostTimeStep`.

The IFM code requires a specific setting of reference values for temperature and concentration according to (2-18).

IMPORTANT NOTICE:
For correctly fitting the brine density, the user must set the following reference values for temperature and concentration in the *Heat and Mass Transport Properties* of FEFLOW:

$$\left.\begin{aligned} T_o &= 0 \\ C_o &= 0 \\ C_s &= 350000 \text{ mg/l (considered as brine concentration at saturation state)} \end{aligned}\right\} \qquad (2\text{-}18)$$

```
static void PostTimeStep (IfmDocument pDoc)
{
  int    e, i;
  double T, p, C;
  double beta, gamma, alpha, BETASTAR, gammastar, ALPHASTAR;
  double alph, alph1, gam, gam1;

    /* Coefficients for the fitting and their derivatives */

  double p0  = 100.;
  double z2 =  2.744492639329977e-23;
  double z1 =  6.3111586728429706e-18;
  double z0 = -6.625358276579406e-13;
  double w2 = -2.5570358684616452e-20;
  double w1 = -4.996112674640022e-15;
  double w0 =  5.718374379180737e-10;
  double v2 =  8.637135897998724e-18;
  double v1 =  1.58244686429457e-12;
  double v0 = -2.051960478431085e-7;
  double u2 = -1.4036263958416905e-15;
  double u1 = -2.4220044746230556e-10;
  double u0 =  0.000039363979779529357;
  double s2 =  1.0032350032434767e-13;
  double s1 =  2.5442857110623736e-8;
  double s0 = -0.0063083048607919245;
  double r2 = -3.6928765749684625e-12;
  double r1 = -1.155475728462599e-6;
  double r0 = -0.04949178536220616;
  double q2 = -5.459359007740163e-10;
  double q1 =  0.0005257539357631474;
  double h0 =  0.00073104758291628;
  double h1 = -9.422037142360847e-10;
  double h2 =  1.821338928754865e-15;
  double r3 = -2.390003668646296e-6;
  double s3 =  3.9534845368831494e-8;
  double u3 = -3.7575488991610133e-10;
  double v3 =  2.1946081669958214e-12;
  double w3 = -6.4836916258079997e-15;
  double z3 =  7.513091563357645e-18;
  double j0 = -3.9446778202994974e-10;
  double j1 =  7.533778133432179e-16;
  double j2 = -2.3273323084072923e-22;
  double r4 =  3.6418368120766765e-12;
  double s4 = -7.725866104001761e-14;
  double u4 =  8.576370648910509e-16;
  double v4 = -5.310521468059033e-18;
  double w4 =  1.6153538522556503e-20;
  double z4 = -1.8936376378424672e-23;

  double bet  = r0+100*r1+10000*r2;
  double bet1 = s0+100*s1+10000*s2;
  double bet2 = u0+100*u1+10000*u2;
  double bet3 = v0+100*v1+10000*v2;
  double bet4 = w0+100*w1+10000*w2;
  double bet5 = z0+100*z1+10000*z2;

   /* Number of elements and number of nodes per element */
  int nElements = IfmGetNumberOfElements(pDoc);
  int nNodes    = IfmGetNumberOfNodesPerElement(pDoc);

   /* Loop through all elements */
  for (e = 0; e < nElements; e++) {
    T = 0.;
    p = 0.;
    C = 0.;
    /* Loop locally through all nodes of element 'e' */
    for (i = 0; i < nNodes; i++) {
      /* Get global node index */
      int indNode = IfmGetNode(pDoc, e, i);

      T += IfmGetResultsTransportHeatValue(pDoc,indNode);
      p += IfmGetResultsFlowPressureValue(pDoc,indNode);
      C += IfmGetResultsTransportMassValue(pDoc,indNode);
    }

    /* Solving the average physical properties (T and p)
      of element 'e' */
    T /= (double)nNodes;
    p /= (double)nNodes;
    C /= (double)nNodes;

    if (p < 100.) p=100.;

    alph  = h0+h2*(p-p0)*(p-p0)+100*h1+10000*h2+
            (p-100)*(h1+200*h2)+(r3+(s3+(u3+(v3+
            (w3+z3*T)*T)*T)*T)*T)*T;
    alph1 = j0+j2*(p-p0)*(p-p0)+100*j1+10000*j2+
            (p-100)*(j1+200*j2)+(r4+(s4+(u4+
            (v4+(w4+z4*T)*T)*T)*T)*T)*T;
    gam   = q1+200*q2+((r1+200*r2)+((s1+200*s2)+
            ((u1+200*u2)+((v1+200*v2)+((w1+200*w2)+
            (z1+200*z2)*T)*T)*T)*T)*T)*T;
    gam1  = q2+(r2+(s2+(u2+(v2+(w2+z2*T)*T)*T)*T)*T)*T;

    /* Set ALPHA */
    alpha=(1./999.843633188666)*(alph+alph1*C);

    /* Set BETA */
```

```
    beta  = -(1./999.843633188666)*(bet+
             (bet1+(bet2+(bet3+(bet4+bet5*T)*T)*T)*T)*T);

    /* Set GAMMA */
    gamma = (1./999.843633188666)*(gam+gam1*(p-p0));

    /* Set GAMMASTAR */
    gammastar = -gamma*(p-p0)/(T+.01);

    /* Set BETASTAR */
    BETASTAR = beta+gammastar;
    IfmSetMatFlowExpansionCoeff(pDoc, e, BETASTAR);

    /* Set ALPHASTAR by multiplying ALPHA time
       Cs = 350000 mg/L */
    ALPHASTAR = alpha*350000.;
    IfmSetMatFlowDensityRatio(pDoc, e, ALPHASTAR);
  }
}
```


Acknowledgements

Dr. Driesner from ETH, Zurich is greatly acknowledged for providing data and his expertise in thermodynamic properties of fluids. I thank Prof. Diersch, Dr. Clausnitzer and Mr. Schätzl from DHI-WASY for the support in developing the IFM code and Dr. Blöcher (GFZ Potsdam) for having further checked the source code.

References

1. Archer, D.G., Thermodynamic Properties of the NaCl+H_2O System. II. Thermodynamic Properties of NaCl(aq), NaCl 2HO(cr), and Phase Equilibria. *Journal of Physical and Chemical Reference Data* **21** (1992), 793-829.
2. Diersch, H.-J.G. Interactive, graphics-based finite-element simulation system FEFLOW for modeling groundwater flow, contaminant mass and heat transport processes. *Reference Manual*, DHI-WASY GmbH, Berlin, 2009.
3. Driesner, T., The system H2O-NaCl. Part II: Correlations for molar volume, enthalpy, and isobaric heat capacity from 0 to 1000 °C, 1 to 5000 bar, and 0 to 1 XNaCl. *Geochimica et Cosmochimica Acta* **71** (2007), 4902-4919.
4. Pitzer, K.S., Peiper, J.C., Busey, R.H., Thermodynamic Properties of Aqueous Sodium Chloride Solutions. *Journal of Physical and Chemical Reference Data* **13** (1984), 1-102.

Appendix A

Nomenclature

Latin symbols

C, C_o	ML^{-3}	concentration and reference concentration (salinity), respectively;
C_s	ML^{-3}	maximum concentration;
p, p_o	$ML^{-1}T^{-2}$	hydrodynamic fluid pressure and reference pressure, respectively;
T, T_o	Θ	temperature and reference temperature, respectively;

Greek symbols

$\bar{\alpha}$	1	density difference ratio (specific solutal expansion coefficient);
$\bar{\beta}$	Θ^{-1}	thermal expansion coefficient;
$\bar{\gamma}$	$M^{-1}LT^2$	fluid compressibility;
ρ^f, ρ_o^f	ML^{-3}	fluid density and reference fluid density, respectively;

Subscripts

o	reference value;

Superscripts

f	fluid (water) phase;

Abbreviations

API	application programming interface;
EOS	equation of state;
FE	finite element;
FEFLOW	finite element flow simulator;
IFM	interface manager;

Subject Index

Author Index

Author Index